Microelectronics meets Catalysis: An interdisciplinary approach on the structure-property relationship of single crystalline $Ce_{1-x}Pr_xO_{2-\delta}$ films on Si(111)

Von der Fakultät für Mathematik, Naturwissenschaften und Informatik
der Brandenburgischen Technischen Universität Cottbus

zur Erlangung des akademischen Grades

Doktor der Naturwissenschaften
(Dr. rer. nat.)

genehmigte Dissertation
vorgelegt von

Dipl. Chem.
Marvin Hartwig Zöllner

Geboren am 19.07.1982 in Nordenham (Deutschland)

Gutacher: Prof. Dr. Thomas Schröder

Gutachter: Prof. Dr. Marcus Bäumer

Gutachter: Prof. Dr. Joachim Wollschläger

Tag der mündlichen Prüfung: 02.04.2014

Acknowledgements

Before presenting my doctoral thesis, I would like to use the opportunity here to thank all people who supported and accompanied me during my stay at IHP for the preparation of my dissertation. In the first instance, I am grateful to Prof. Dr. Thomas Schröder for the chance to start my scientific carrier at IHP and that he imparted to me the present dissertation topic. Furthermore, I am thankful for his dedicated approach to communicate his scientific knowledge to me. I am indebted to Prof. Dr. Joachim Wollschläger for introducing me into the world of synchrotron based X-ray diffraction. Further thanks are devoted to Prof. Dr. Marcus Bäumer for scientific discussions especially in the field of catalysis. I am grateful to the “Deutsche Forschungsgemeinschaft” (DFG) for financial support Grant No. SCHR 1123/4-1.

Special thanks belong to Dr. Peter Zaumseil for didactic discussions and teaching me X-ray diffraction methods; to Dr. Alessandro Giussani for introducing me into the DFG project; to Hans Thieme for supporting me at the molecular beam epitaxy; to Dr. Gang Niu for his support and motivating scientific enthusiasm; to Dr. Jarek Dabrowski for atomistic ab-intio calculations performed at the JUROPA supercomputer in Jülich within the Neumann Institute for Computing (NIC) Grant No. hfo06; to Dr. Andreas Schubert for performing transmission electron microscopy measurements; to Jhin-Hao Jhang for performing temperature programmed desorption spectra; to Dr. Ioan Costina for supporting me at any kind of surface science characterization method; to Dr. Wolfgang Caliebe for support at beam line W1 of the Hamburger Synchrotron Strahlungslabor (Hasylab); to Prof. Dr. Federico Boscherini and Dr. Francesco d’Acapito for support at the GILDA beamline (BM08) at the European Synchrotron Radiation Facility (ESRF).

I am thankful to all my other colleagues and project partners for scientific discussions and advices: Prof. Dr. Michael Reichling, Dr. Andreas Schäfer, Dr. Canan Baristiran Kaynak, Dr. Christian Reich, Dr. Christian Walczyk, Dr. Christian Wenger, Dr. David Kot, Dr. Hans-Hermann Pieper, Dr. Grzegorz Kozlowski, Dr. Grzegorz Lupina, Dr. Gunther Lippert, Dr. Henrik Wilkens, Dr. Lidia Lupina, Dr. Mindaugas Lukosius, Dr. Olaf Seifarth, Dr. Oliver Skibitzki, Dr. Pauline Calka, Dr. Piotr Dudek, Dr. Sebastian Gevers, Dr. Thomas Bertaud, Damian Walczyk, Malgorzata Sowinska, Manja Krause, Reinhard Olbrich, Tomasz Grzela, Udo Kaletta, Yvonne Heier.

I like to express my deepest gratitude to my family and friends for keeping me grounded.

Zusammenfassung

Motivation: Ceroxid wurde viel Beachtung in der Mikroelektronik (z.B. als hoch-k Oxid, Pufferschicht in der Heteroepitaxie) und in der Katalyse (z.B. zur selektiven Oxidation und für Dehydrierungsreaktionen) geschenkt, aufgrund seiner innewohnenden strukturellen (ähnliche Kristallstruktur und kleine Gitterfehlanpassung in Bezug auf Silizium) und elektronischen (Variation des Ce^{4+}/Ce^{3+}-Valenzzustandes und Ausbildung von Sauerstoffvakanzen) Eigenschaften. Deshalb wurden einkristalline und epitaktische Ceroxiddünnfilme ausgiebig untersucht. Obwohl das benachbarte Seltenerdoxid, Praseodymoxid, ergänzende Eigenschaften aufweist, wurde es weit aus weniger studiert, wohl aufgrund seines komplexen Phasendiagramms. Da beide Oxide ein flexibles strukturelles (Polymorphismus) und elektronisches (Variation des Valenzzunstandes) Verhalten aufweisen, ist es von anhaltendem Interesse, Cer-Praseodym-Mischoxide genauer zu untersuchen, um gezielt bestimmte Eigenschaften für die jeweilige Anwendung einzustellen und zu verbessern.

Ziel: Zwecks dessen ist es das Ziel dieser Doktorarbeit in einem interdisziplinären Ansatz solche einkristallinen und epitaktischen, binären und ternären $Ce_{1-x}Pr_xO_{2-\delta}$ Dünnfilme zu wachsen und zu charakterisieren, um so hochqualitative Proben für weitere Grundlagenstudien, bezüglich der strukturellen und elektronischen Eigenschaften, zur Verfügung zu stellen, die für künftige Anwendungen in Mikroelektronik und Katalyse von Interesse sind.

Experiment: Solche einkristallinen und epitaktischen $Ce_{1-x}Pr_xO_{2-\delta}$ Dünnfilme wurden auf einem Si(111) Substrat mittels Molekularstrahlepitaxie gewachsen. Eine in-situ Kontrolle über die Kristallwachstumsqualität wurde mittels Beugung hochenergetischer Elektronen bei Reflexion erreicht. Eine detaillierte Strukturaufklärung wurde mittels labor- und synchrotronbasierter Röntgenstreuung durchgeführt. Zusätzlich diente Transmissionselektronenmikroskopie dazu eine hochauflösende Einsicht in die Struktur zu bekommen. Die strukturelle Charakterisierung wurde mit theoretischen ab-initio Berechnungen untermauert. Um die Stöchiometrie und den Valenzzustand in den ternären Mischoxiden zu bestimmen, wurde Röntgenphotoelektronenspektroskopie benutzt. Die mikroskopische Defektstruktur wurde mittels Ramanspektroskopie untersucht. Schlußendlich gab die Temperatur-programmierte Desorption einen ersten Einblick in das katalytische Verhalten.

Ergebnisse: Die strukturellen Untersuchungen implizieren ein epitaktisches, zwillingsfreies, ausschließlich typ-B orientiertes $CeO_2(111)$ Wachstum auf $Si(111)$ mittels einer ultradünnen hex-$Pr_2O_3(0001)$ Pufferschicht. Dies wurde durch die kristallographische Weiterführung des Sauerstoffuntergitters und den Erhalt des halbleitenden Verhaltens an der Ceroxid-Praseodymoxid-Grenzfläche möglich. Eine Stabilisierung von Pr^{4+} Kationen wurde mittels ab-initio Berechnungn vorausgesagt, um den Grenzflächenübergang zu begünstigen. Auf solchen hex-$Pr_2O_3(0001)/Si(111)$ Trägern wurde auch das Wachstum von ternären $Ce_{1-x}Pr_xO_{2-\delta}$ Mischoxiden ermöglicht. Eine stöchiometrieabhängige Studie implizierte ebenfalls ein Zusammenspiel von strukturellen und elektronischen Eigenschaften. In Abhängigkeit von dem Pr Gehalt stellte sich heraus, dass in der Tat Mischungen mit Pr^{3+} Eingliederung in die CeO_2 Fluoritmatrix und mit Ce^{3+} Eingliederung in die hex-Pr_2O_3 Matrix resultierten. Zwischen diesen beiden Grenzfällen wurde gezeigt, dass eine höhere Pr-Konzentration zu einer höheren Tendenz führte, Ce^{3+} Kationen in einem Bixbyit Gitter zu bilden. Jedoch konnten Fluoriteinschlüsse nicht ausgeschloßen werden. In einer ersten temperaturabhängigen Studie bezüglich des Reduktionsverhaltens wurde mittels des linear steigenden, integralen O_2 Desorptionssignals und des kristallographischen Netzebenenunterschiedes der geheizten $Ce_{1-x}Pr_xO_{2-\delta}$ Mischoxide demonstriert, dass die Sauerstoffspeicherungsfähigkeit aufgrund des Pr^{4+}/Pr^{3+} Redoxsystems über die Pr-Dotierung maßgeschneidert werden kann. Des Weiteren wurde festgestellt, dass der Kohlenwasserstoffoxidationprozess hauptsächlich über das Ce^{4+}/Ce^{3+} Redoxsystem gesteuert wird, da die Desorptionstemperatur von CO_2 sich mit steigendem Ce Gehalt verringert.

Ausblick: Solche eptaktischen und einkristallinen $Ce_{1-x}Pr_xO_{2-\delta}/Si(111)$ Heterostrukturen sind in den Forschungsbereichen der Katalyse und Mikroelektronik von Interesse für zukünftige Untersuchungen. Sie können als modelkatalytisches System verwendet werden, um einen tieferen Einblick in die Korrelation von kristallographischer und elektronischer Struktur mit den Reaktionsmechanismen zu erhalten, indem die Komplexität des Systems schrittweise unter definierten Reaktionsbedingungen erhöht wird. Des Weiteren können neue Anwendungen im Bereich der Mikroelektronik evaluiert werden. „Oxygen vacancy engineering“ in Seltenerdoxiden wird bereits intensiv untersucht, um „room temperature ferromagnetism“ Phänomene zu erklären und gegebenfalls in der Spintronik nutzbar zu machen.

Abstract

Motivation: Ceria attracted a lot of attention for microelectronics (e.g. high-k gate oxide, buffer layer for heteroepitaxy) and catalysis (e.g. selective oxidative and dehydrogenating reactions), due to its inherent structural (similar crystal structures and small lattice mismatch with respect to silicon) and electronic (Ce^{4+}/Ce^{3+} valence state variation and formation of oxygen vacancies) properties. Thus, single crystalline epitaxial ceria thin films are well investigated. Although, the neighbouring rare earth oxide, praseodymia, exhibits similar properties, this system is much less studied due to its complex phase diagram. Since both oxides exhibit a flexible structural (polymorphism) and electronic (valence state variation) behavior, it is of ongoing interest to study ceria-praseodymia mixed oxide thin films, in order to tune and improve certain characteristics for the respective applications in the field of microelectronics and catalysis.

Goal: Therefore, the goal of this doctoral thesis is to grow and characterize in an interdisziplinary approach single crystalline and epitaxial, binary and ternary $Ce_{1-x}Pr_xO_{2-\delta}$ thin films in order to allocate high quality samples for further fundamental studies, devoted to the structural and electronic properties in the field of microelectronics and catalysis.

Experimental: Such single crystalline and epitaxial $Ce_{1-x}Pr_xO_{2-\delta}$ thin films were grown on a Si(111) substrate by molecular beam epitaxy. An in-situ control of the crystal growth quality was achieved by reflection high-energery electron diffraction. A detailed structure characterization study was carried out by laboratory and synchrotron based X-ray scattering. Additionally, transmission electron microscopy gives a highly resolved structural insight. The structural characterization was supported by theoretical ab-initio calculations. To determine the stoichiometries and valence states of the ternary mixed oxide compounds, X-ray photoelectron spectroscopy was performed. The microscopic defect structure was investigated by Raman spectroscopy. Finally, a first insight into the catalytic behavior is gained by temperature programmed desorption experiments.

Results: The structural investigation implicates an epitaxial, twin-free, exclusively type-B oriented $CeO_2(111)$ growth on Si(111) by using an ultra-thin hex-$Pr_2O_3(0001)$ buffer layer. This became possible due to the crystallographic continuation of the oxygen sub-lattice and

electronic conservation of the semiconducting behavior at the ceria/praseodymia interface. A stabilization of Pr^{4+} cations is predicted by ab-initio calculations to support this interface transition. On such a hex-$Pr_2O_3(0001)$/Si(111) support the growth of epitaxial ternary $Ce_{1-x}Pr_xO_{2-\delta}$ mixed oxides became also possible. A stoichiometry dependent study also implicates an interplay of the structural and electronic properties. In dependency on the Pr content, it turned out that truly mixed alloys with Pr^{3+} incorporation into the CeO_2 fluorite crystal matrix and Ce^{3+} incorporation into the hex-Pr_2O_3 matrix were achieved. Between both extremes, it is shown that the Pr content leads to a higher tendency to form Ce^{3+} cations within a bixbyite lattice, but fluorite inclusions could not be excluded. In a first temperature dependent study on the reduction behavior, it was demonstrated by the linearly increasing behavior of the integral O_2 desorption signal and the total lattice spacing difference of heated $Ce_{1-x}Pr_xO_{2-\delta}$ mixed oxides that the oxygen storage capacity can be tailored by Pr doping due to the Pr^{4+}/Pr^{3+} redox system. Furthermore, it was found that the hydrocarbon oxidation process is mainly triggered by the Ce^{4+}/Ce^{3+} redox system, since the desorption temperature of CO_2 decreased with increasing Ce content.

__Outlook:__ In terms of future investigations, such epitaxial single crystalline $Ce_{1-x}Pr_xO_{2-\delta}$/Si(111) heterostructures are of interest in both research fields, catalysis and microelectronics. They can be used as model catalytic systems in order to gain a deeper understanding of the structure and electronic correlation with the reaction mechanisms by a stepwise increasing of the system`s complexity under defined reaction conditions. Furthermore, new applications of such a system might be evaluated in the field of microelectronics. Oxygen vancancy engineering is currently discussed in such rare earth oxides to explain and establish room temperature ferromagnetism phenomena in the area of spintronics.

Table of contents

Chapter 1

Introduction

1.1 Motivation

Research and development in materials science are always faced to new challenges to increase the performance of industrial commodities. In general, different fields of application seem to have no intersection in their interest due to their quite different array of products, as in the case of microelectronics and catalysis. However, for research and development of new materials the tasks are becoming more and more difficult. In nano science the complexity of problems and their microscopic origin are based on similar solid state physical questions limiting the performance. This idea can be illustrated by the art of "pointillism". Although the pictures of Fig. 1 are showing totally different motifs, the enlargements reveal their common and similar base. In this sense: "Microelectronics meets Catalysis" in fundamental questions of material science. These structural and compositional connections become closer in nano scaled objects concerning surface and bulk effects, which are of interest for the thin film research. To efficiently overcome these challenges the resources from different research fields have to be combined and an extensive knowledge transfer is obligatory. For instance, metal/oxide interactions are long known in oxide supported metal catalysts, but also became of crucial importance in microelectronic metal-oxide-semiconductor field-effect transistors (MOSFET)

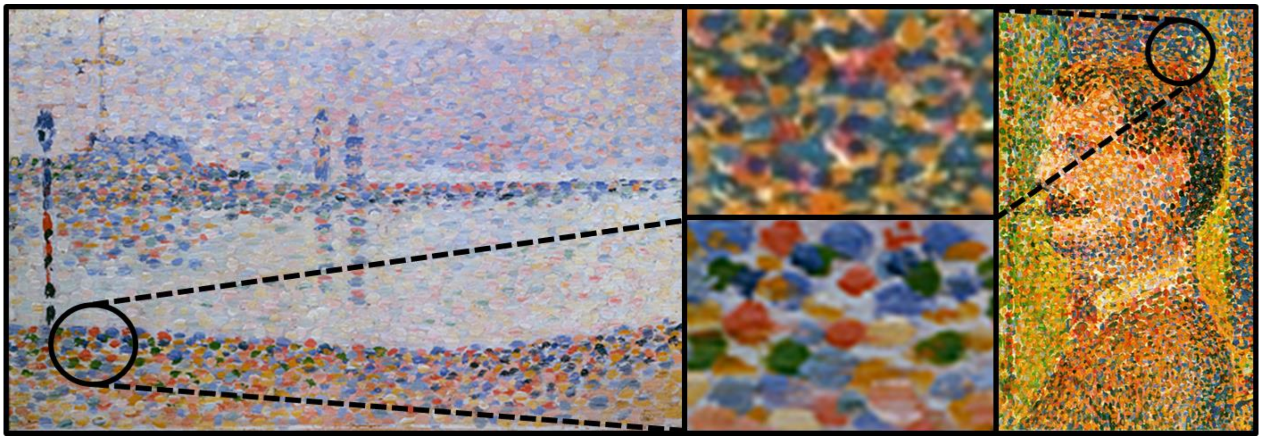

Figure 1: Pictures from Georges Seurat: "Le Port de Gravelines" (left) and "The Slide Show"(right) and zoom-in of certain areas.

as metal-gate/oxide stacks in terms of preparation (wetting behavior, impurity migration) and electronic characteristics (interface states).

One still important topic of such an interdisciplinary research field is related to rare earth oxides (REOs), which are of high interest for new technologies. Firstly, they demonstrated wide applications in catalysis for oxidative and dehydrogenating reactions.[1] Furthermore, the REOs are of great interest in microelectronics, where they are discussed as alternative gate oxide for the scaling of devices[2] and as buffer layers for the integration of functional materials[3]. Of special interest are the oxides of cerium and praseodymium, also called ceria and praseodymia, due to their inherent properties.[4, 5] Furthermore, the combination of ceria and praseodymia allows tuning these properties, whose microscopic origin is still not fully understood up to now.

Both oxides are known for their well fitting lattice constant to the silicon substrate and thus this characteristic offers the opportunity to grow high quality epitaxial single crystal thin films on a wafer scale. In this thesis, such single crystalline heteroepitaxial $CeO_2(111)$ and mixed $Ce_{1-x}Pr_xO_{2-\delta}(111)$ thin films are grown with the help of a Pr_2O_3 buffer layer on a $Si(111)$ substrate and characterized in terms of structure, valency and redox behavior for two kinds of application:

I. At first, this enables to deliver a new kind of model support system for model catalytic studies, which is important since this thin film approach allows to apply more surface science investigation methods needing a conducting substrate. In this way, large scale ceria and praseodymia samples of identic quality can be delivered for several investigation methods and thus allows to generate consistent multitool surface science studies.

II. These oxides can serve as buffer layer for the integration of other functional materials as semiconductors or oxides. Thus, virtual substrates for module integration might be created keeping the know-how of a silicon based technology platform. Additionally, investigations of the inherent functional properties of such mixed oxide thin films themselves may be as well of scientific interest.

1.2 Structure of the thesis

In this doctoral thesis a growth and characterization study of combined cerium and praseodymium oxide systems on a Si(111) substrate will be presented in order to allocate proper oxide thin films for the introduced applications. The chapters are arranged in the following way:

Chapter 2: The significance of REOs in microelectronics and catalysis will be shown. It will be pointed out that both research fields pay attention to similar scientific questions. Afterwards, an introduction to the related material systems is presented focusing on the structural properties. From their quite complex behavior arises the necessity of transferring the knowledge from ceria and praseodymia growth studies to further model studies.

Chapter 3: The sample preparation, concerning the substrate pre-treatment, the oxide deposition and annealing procedure will be shown. Furthermore, the used investigation methods will be summarized to get an insight into the theoretical background. Especially, X-ray diffraction, X-ray photoemission spectroscopy and Raman spectroscopy will be explained in more detail.

Chapter 4: Chapter four is based on the results gained within the scope of this doctoral thesis. The first part points out the necessity of a CeO_2/Pr_2O_3 bilayer system for the growth on Si(111) on the basis of an extensive structure characterization. In the second part the growth technique is applied to grow single crystalline epitaxial $Ce_{1-x}Pr_xO_{2-\delta}$ thin films with help of a Pr_2O_3 buffer layer. After structure and compositional characterization, the redox behavior of such $Ce_{1-x}Pr_xO_{2-\delta}$ mixed oxide heterostructures on a Si(111) support is presented and discussed.

Chapter 5: Finally, the results of the thesis will be concluded and the implications on structure, valency and reactivity will be pointed out. At the end a short outlook is given on recent and ongoing investigations concerning catalytic and microelectronic applications.

Chapter 2

Background on ceria and praseodymia

2.1 Rare earth oxides in microelectronics

2.1.1 REOs as alternative gate oxides

Since the first metal oxide semiconductor field-effect transistor (MOSFET) by Khang and Atalla in 1960 was found, the complementary-MOS (CMOS) technology became the dominating technology opening the era of information society.[6, 7] This device needs an insulating layer (SiO_2) to separate the gate electrode from the semiconductor channel, which conducts the current from source to drain in on state (Fig. 2.1).

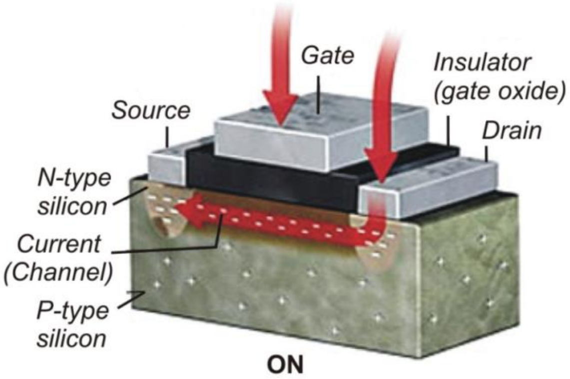

Figure 2.1: Scheme of a MOSFET in ON-state (technical current flow direction indicated).[8]

Within the scope of miniaturization fast progress was achieved by reducing the transistor dimensions and hence by decreasing the gate oxide thickness. According to an empirical prediction, Moore's law describes this development leading to a doubling of the transistor number per area each two years. However, the reduction of the MOSFET dimensions is reaching its physical limits due to leakage current by tunneling of electrons through the insufficient thick SiO_2 layer.[9] In order to follow the "More Moore" scaling the researchers were looking for alternative gate oxides to achieve a higher equivalent oxide thickness (EOT). Therefore, the oxides have to fulfill several requirements:[10]

1) To allocate a smaller EOT, the gate oxide should exhibit a higher permittivity k (Fig. 2.2a). This is the reason why they are also called high-k oxides. Furthermore, a high band offset (Fig. 2.2b) with respect to silicon is needed to increase the tunnel barrier.
2) The oxide/Si interface has to be thermodynamical stable to avoid interface reactions between Si and the high-k oxide forming SiO_2, silicates or silicides.
3) The interface defect density and hence the interface trap states have to be minimized to reduce the flatband voltage shift.
4) It turned out that the film morphology greatly influence the electrical properties and that amorphous films are the better choice suppressing leakage current at grain boundaries.
5) The oxide thin films should exhibit a good compatibility with materials and processes used in state-of-the-art CMOS technology.
6) A high reliability of the electrical properties in terms of stress-induced leakage current, time-dependent dielectric breakdown and mean time to failure measurements is needed.

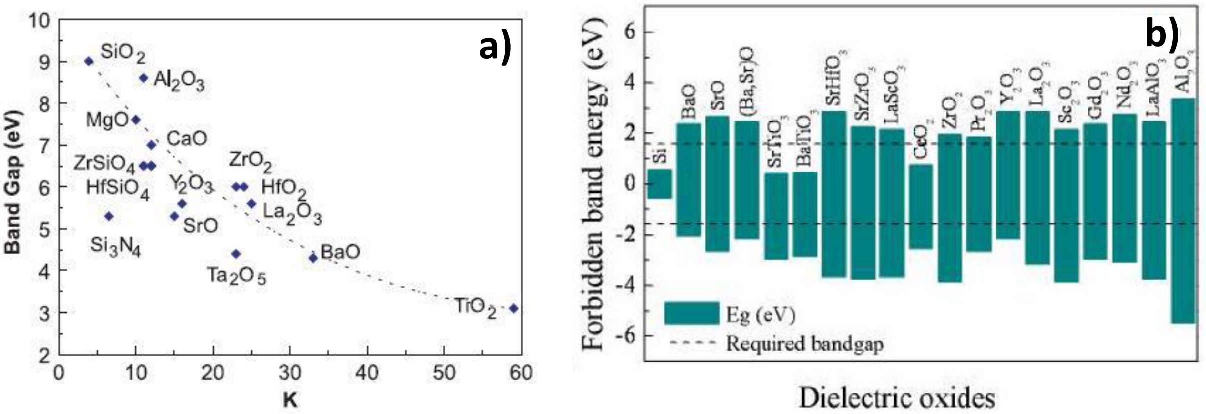

Figure 2.2: (a) Band gap vs. dielectric constant[11] and (b) minimum required insulator band gap (dashed lines) with respect to silicon for several insulating oxides[12].

A lot of oxides including the ones from earth alkalines (BaO, SrO), transition metals (ZrO_2, HfO_2, Y_2O_3) and lanthanides (La_2O_3, CeO_2, Pr_2O_3) were investigated for these properties,[13-15] but only some of them give appropriate results for the application as alternative gate oxide. Unfortunately, materials with a high permittivity appear with a small band gap leading to a trade-off (Fig. 2.2a).[11, 16] Although, ceria and praseodymia have high permittivities they turned out to be less promising because their band gap is closely located to the forbidden region (dashed lines in Fig. 2.2b). Hubbard and Schlom could exclude several binary oxides by investigating the thermodynamical stability with the silicon interface.[15, 17] However, vice versa they could not predict stable oxides, since the thin film properties vary from the bulk ones. Although single crystalline oxides were widely studied, amorphous films turned out to be the better choice. Meanwhile, amorphous HfO_2 and Hf-silicate films with metal gate are established for 45nm technology in microelectronic industry,[18] but for future developments it might be necessary, e.g. to combine several materials in ternary oxides ($LaLuO_3$, $PrYO_3$)[19, 20] or bilayers ($LaLuO_3/Al_2O_3$)[21], what possibly helps to improve certain characteristics as permittivity, band alignment or interface states.

2.1.2 REOs as buffer layers

To add new functionalities to Si microelectronics not by scaling ("More Moore") but by non-classical module integration, the "More than Moore" approach is followed, which often relies on functional material integration on a Si-wafer platform. Heteroepitaxial single crystalline oxides on silicon (COS) are of elementary importance for this "engineered wafer approach", because they contain the crystallographic information.

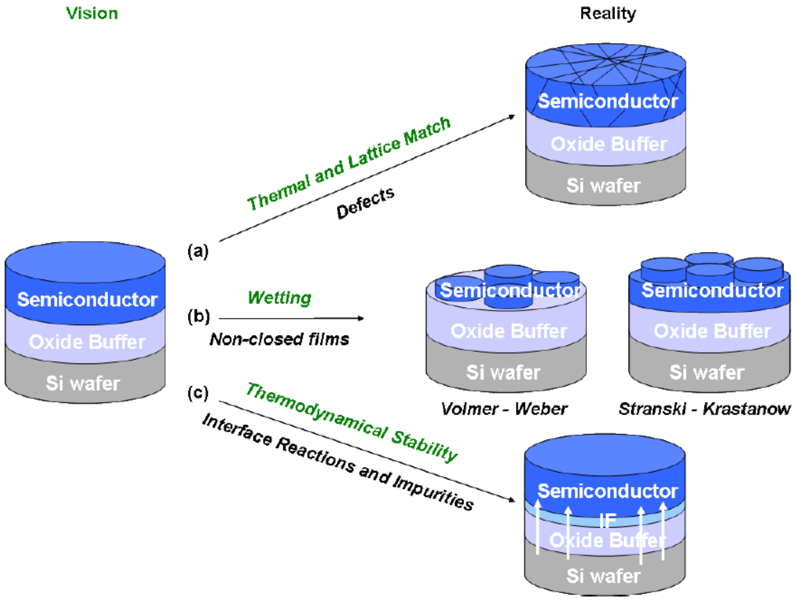

Figure 2.3: Schematic challenges of the engineered wafer approach.[22]

However, several challenges have to be overcome (Fig. 2.3):[22]

1) The oxide buffer should exhibit a good thermal and lattice match not only to the silicon substrate but also to the integrated semiconductor. In this way defects like misfit dislocations and threading dislocations in the semiconductor can be reduced.

2) The wetting behavior of the semiconductor on the oxide buffer should be based on Frank-van-der-Merwe growth to achieve closed films and to avoid surface roughness as in the case of Volmer-Weber and Stranski-Krastanov growth.
3) Thermodynamically stable interfaces reduce interface reactions and impurities.

Fortunately, the high number of oxides crystallizing in the bixbyite lattice and further closely related crystal structures allows to tune the buffer properties:

1) Lattice constant and coefficient of thermal expansion (CTE) reducing defect formation.
2) Surface energies improving the wetting behavior.
3) Chemical reactivity reducing impurities.

This plays a crucial role for the buffer layer applications, because the integrated material can at best only be as good as its buffer layer is. Therefore, it is important to know the crystallographic properties well, as a buffer is only an approximation to a perfect single crystal. REOs are of special interest for this "engineered wafer approach" considering the well-fitting lattice constants. Furthermore, the REOs can profit from their flexibility by combining different materials as bilayer stackings or mixtures, as presented for Sc_2O_3/Y_2O_3 bilayers or $PrYO_3$[23] mixed oxides. A high expertise for the growth of epitaxial single crystalline REOs on silicon was developed at IHP. For instance, the growth of silicon[24-26] (e.g. SOI for photonics, micro-electro-mechanical systems), germanium[27] (e.g. GeOI for photonics, concentrated photovoltaics), III-V semiconductors (e.g. GaN for solid state lighting, high-electron-mobility transistors)[28] or functional oxides (e.g. $CoFe_2O_4$ for spintronics)[29] was demonstrated on a Si platform (Fig. 2.4).

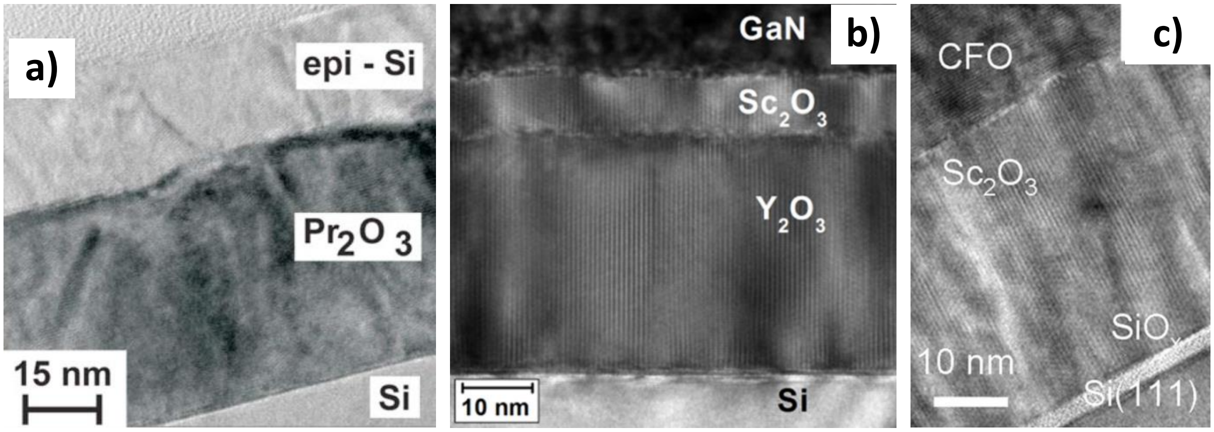

Figure 2.4: TEM images of (a) $Si/Pr_2O_3/Si(111)$[26], (b) $GaN/Sc_2O_3/Y_2O_3/Si(111)$[28] and (c) $CoFe_2O_4/Sc_2O_3/Si(111)$[29].

2.2 Rare earth oxides in catalysis

2.2.1 Catalytic reactions of REOs

Heterogeneous catalysis plays a crucial role for industrial applications serving daily life needs. This kind of catalysis is used for the industrial production of several basic chemicals, e.g. the famous Haber-Bosch process for ammonia (NH_3) synthesis.[30] An application which is better known in the public is the automotive exhaust emission control by catalytic converters.[31]

These processes are good examples for the complexity of the heterogeneous catalysis. Here, the catalyst and the reactants are provided in different phases, whereby the catalyst is usually a solid. Furthermore, the catalyst is not only consisting of a single material. Besides metals, more and more oxides become important. These oxides have great influence on the catalytic activity and fulfill multifunctional tasks. They can be used as structure promoter to increase the surface area, as refractory substrate to avoid sintering, as electronic promoter for higher activity, to avoid poisoning of the catalyst or to support the catalyst dispersion.[32]

Considering the supply and activation of atomic or molecular oxygen in chemical reactions, oxides with variable valence states are of interest, e.g. Ti_3O_5, V_3O_5, Fe_3O_4. In this context, REOs are also well known as oxygen buffer and activator. They exhibit several similarities and tendencies in their catalytic behavior, due to their inherent promoting properties (chapter 2.4).[4] These characteristics of the REOs make them interesting for several catalytic applications,[1] e.g. oxidative dehydrogenation (ODH),[33] oxidative coupling of methane (OCM),[34] partial oxidation to synthesis gas,[35] three-way catalysis (TWC)[36] and water-gas shift reaction for hydrogen production.[37] Especially, a lot of studies on the REOs were already performed related to the activity and selectivity of oxidative and dehydrogenating reactions.

Fig. 2.5 shows the relative activities of the rare earth oxides for the oxygen exchange and the hydrogen oxidation. Antoshin *et al.*[38] found in both cases for praseodymia the highest and for terbia the second highest activity noting that both oxides exhibit variable valences, resulting thus in extremely complicated phase diagrams (forming so called non-stoichiometric oxides with mixed valences).

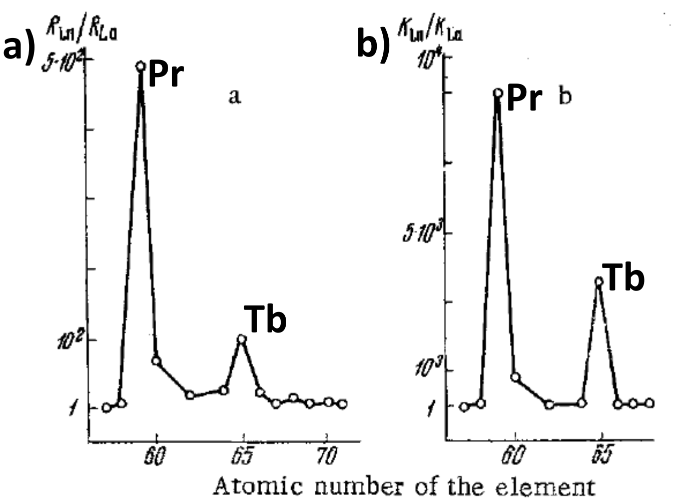

Figure 2.5: Relative activities of the rare earth oxides for (a) isotopic oxygen exchange at 370° and (b) hydrogen oxidation at 340°.[38]

DeBoy *et al.*[39] and Otsuka *et al.*[40, 41] performed a screening of the oxides for the OCM activity. The educts are methane (CH_4) and oxygen (O_2) and the desired reaction products are ethane (C_2H_6) and ethene (C_2H_4):

$$CH_4 + O_2 \rightarrow C_2H_x + H_2O$$

La_2O_3 and Sm_2O_3 were found to have the highest reactivity and selectivity for these C_2-compounds (C_2H_x). They also investigated that the selectivity is the lowest for ceria, praseodymia and terbia among the REOs. The REOs with variable valence states (under reaction condition) rather tend to total oxidation with carbon dioxide (CO_2) as product. (Fig. 2.6)

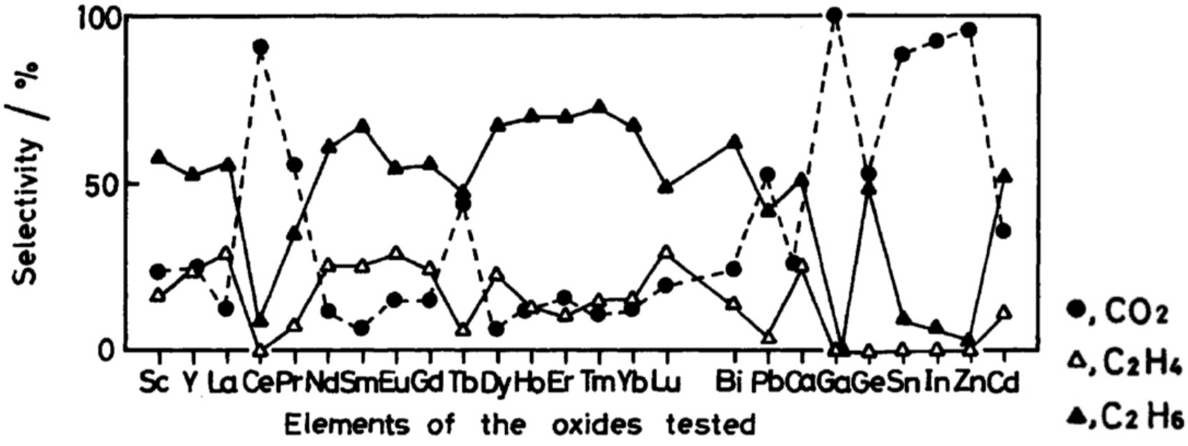

Figure 2.6: Selectivities of various oxides (including REOs) for the oxidative coupling of methane with molecular oxygen at 700°C.

Another study of Asami *et al.*[34] related to the OCM with CH_4 and CO_2 as educts shows different results:

$$CH_4 + CO_2 \longrightarrow C_2H_x + H_2O + CO$$

Here, ceria, europia and terbia were found to have the highest conversion of CH_4. However, ceria shows again low C_2-selectivity. In contrast to the studies with O_2 feed, praseodymia and terbia surprisingly show very high activities and selectivitities. It seems that the variable valence states are supporting the activation of the oxygen from CO_2. It is suggested that the mechanism differs, due to the formation of carbonates. This would also explain the low activity of the lanthania, which has the highest basicity and tendency for carbonate formation.[42] (Fig. 2.7)

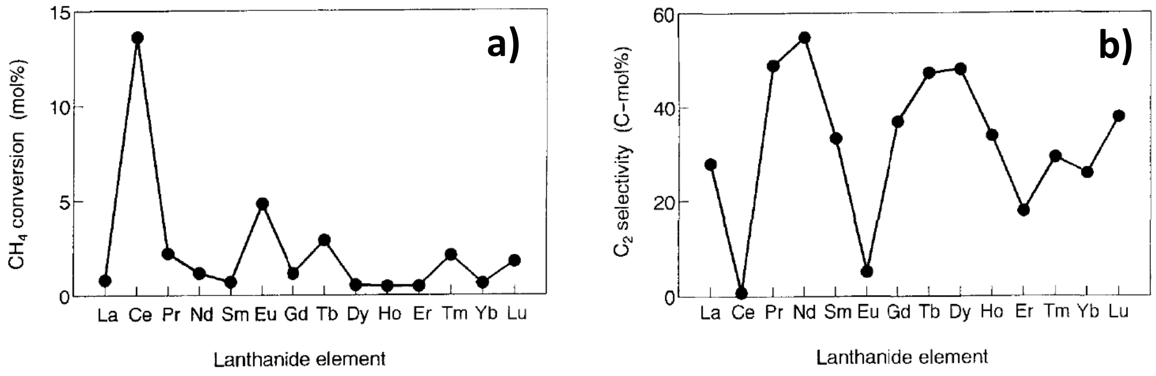

Figure 2.7: (a) Methane conversion and (b) C_2 selectivity for the oxidative coupling reaction of methane with carbon dioxide over the lanthanide oxides at 850°C.[34]

2.2.2 Mechanism of dehydrogenating reactions on REOs

Here, the mechanism of dehydrogenating reactions on REOs is shortly summarized from literature, to get a better understanding which properties and why these properties are important and how they influence the activity and selectivity. Many studies were performed on rare earth oxides to explore the corresponding reaction pathways and kinetic mechanisms.[5]

For ODH and OCM, a dehydrogenation step occurs which is mainly responsible for the conversion or rather activity. For the OCM, it is generally accepted that methyl radicals (CH_3•) are involved in this process.[43, 44] Furthermore, it is reported that the coupling of the methyl radicals subsequently takes place in the gas phase.[45-47] However, a lot of aspects concerning the reaction pathway are still unclear. The C-H bond activation could occur reversible with recombination to CH_4 or irreversible leading to the final products CO_x and C_2-compounds. A *reversible reaction* via a *heterolytic activated* C-H bond rupture was proposed by Choudhary *et al.*[48, 49] Here, adsorbed carbanions (CH_3^-) and oxygen molecules are involved in the radical formation. The qualitative tendency for this reaction is analog to the basicity, except for the oxides with multiple oxidation states (CeO_2, Pr_6O_{11} and Tb_4O_7).[42, 44] So, the abstraction of hydrogen from methane seems to be not only dependent on the basicity but on a complex acid-base pair interaction of the rare earth oxide surface with the molecule. The acid-base properties of the REOs were investigated by thermal desorption of CO_2 and NH_3.[48] The stronger the carbanion is bonded to the metallic acid site on the surface, the more combustion products are formed. Indeed, it was found that the acidity strength order of the rare earth oxides is inverse to the C_2 selectivity. The reason for the total oxidation is suggested to be related to such electrophilic surface oxygen species, as O_2^-, O_2^{2-} or O^- specie. It is controversially discussed if the reversible activation is just an intermediate step for an irreversible reaction or just a secondary reaction.[47, 50] Another *irreversible reaction* pathway leading to the products could be the *homolytic activation* proposed by Ito *et al*.[51] Here, the methane activation is initiated from the gas phase by an O^- surface specie leading to a homolytic bond rupture.

The kinetic of most heterogeneous catalytic reactions with two components are based on the Langmuir-Hinshelwood (LH) or Eley-Rideal (ER) mechanism, as for the heterolytic C-H activation or for the homolytic C-H activation. Reactions involving an adsorbed molecule specie and a lattice anion, such as an oxide, sulfide, chloride or hydride, can be described by the Mars-van-Krevelen mechanism.[52, 53] Fig. 2.8 schematically shows this mechanism by taking the example of CO oxidation on RuO_2.[54] A CO molecule adsorbs at a coordinatively unsaturated Ru atom on the oxide surface and reacts with the lattice oxygen. After CO_2 desorption an oxygen vacancy is left behind, which can be refilled by oxygen from the gas phase or travels by oxygen diffusion to another lattice positions. Due to the complexity, the OCM and the ODH do not proceed typically with a certain reaction pathway and kinetic for different oxide materials.[55, 56]

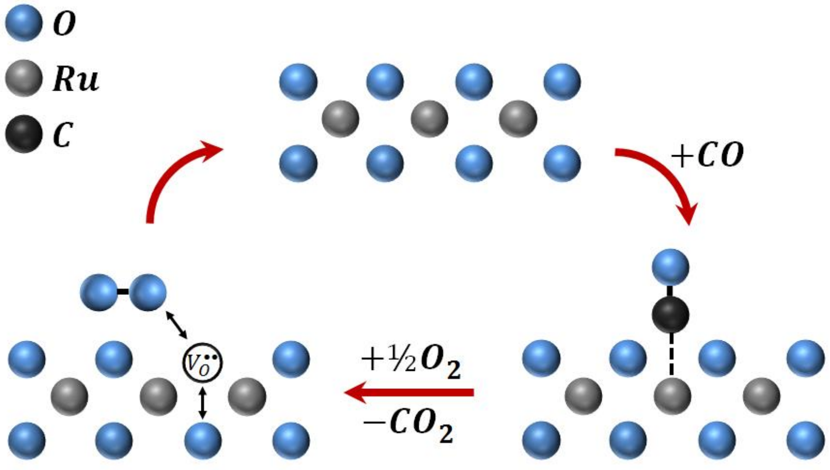

Figure 2.8: Schematic CO oxidation on oxide surface described by the Mars-van-Krevelen mechanism.[54]

For reactions involving the exchange of oxygen, e.g. for the Mars-van-Krevelen mechanism, reversible oxidation-reduction cycles are obligatory. In correlation, the oxygen exchange activity and oxygen mobility in the lattice play an important role. In REOs, ceria and praseodymia provide a high oxygen storage capacity (OSC) and oxygen mobility, due to their crystal structure and reversible change in their valence states 3+ and 4+. Therefore, they are considered to be appropriate catalysts for dehydrogenating reactions of hydrocarbons. In order to tune the properties of ceria and praseodymia, the combination of both compounds is a possible approach.[57-60] However, to obtain an insight into the increasing complexity of their properties and reaction behavior, model catalytic studies are often a helpful basic science research approach.

2.3 Microelectronics meets catalysis

2.3.1 Surface science approach

As shown in the previous chapters, similar scientific questions and prerequisites concerning defects and oxide interfaces in functional oxide materials are of interest for microelectronics as well as for catalysis. In particular, surface and bulk defects strongly affect the structural and chemical properties of materials, which consequently influence their electrical characteristics (e.g. leakage current, flatband voltage shift) and catalytic characteristics (e.g. oxygen diffusion, adsorption sites, reactivity). Therefore, it is necessary to understand the structure-property correlation in order to possibly improve the materials performance in both fields. However, the reality is often quite complex considering three dimensional (3D) amorphous or polycrystalline material compositions. For instance, REOs show polymorphism and varying oxygen stoichiometry.

In terms of catalytic activity and selectivity, the complexity makes it difficult to explore and correlate the structural and chemical properties. A better methodology would consist in performing such investigations on single crystalline oxides. If these are not accessible, model support systems (as single crystalline thin films on a single crystal support) are a valuable approach in surface science. The idea of a stepwise simplification to planar systems was created by Irving Langmuir.[61] He is the eponym for the Langmuir adsorption isotherm, which defines the equilibrium coverage of a surface by molecules from the gas phase in dependency of the temperature and the partial pressure. This one is valid for the monolayer adsorption on a surface with energetically equal occupation positions and no interactions between adsorbed molecules or adsorption positions.[62] This concept was the basis for the so called "surface science approach" developed by Gerhard Ertl,[63] which was already successfully applied to the clarification and development of the catalytic hydrogenation of nitrogen to ammonia.[64, 65] Therefore, model catalytic surface science experiments are a valuable approach to first understand and later tailor catalytic properties.

Meanwhile, ultra-high vacuum (UHV) growth studies and investigations of single crystalline oxide thin films on a silicon support are quite common in microelectronics (see chapter 2.4). Therefore, this expertise about oxide thin film preparation can be transfered from microelectronics to catalysis and one can use this knowledge in the field of model catalytic systems. By using single crystalline thin oxide films on plane substrates, e.g. ceria and praseodymia on a silicon support as model catalyst systems, one can reduce the industrial complexity to two-dimensional (2D) films with specific orientation and defined defect densities.[66] This simplification offers the advantage to correlate the catalyst properties with its behavior under different environmental conditions by applying the plethora of surface science tools even for atomistic studies. However, to profit from this approach, the thin film systems have to fulfill several prerequisites:

1) Well-ordered, flat and continuous single crystalline thin films are required in order to allocate only a specific surface and to avoid influence from the substrate.
2) To keep equivalent chemical conditions, varying stoichiometries, impurities and external influences (substrate, holder, etc.) have to be excluded.
3) To correlate between the properties and catalytic behavior, the model system should exhibit the opportunity to be analyzed. Therefore, electrical conductivity is important to enable measurements causing otherwise charging effect, such as scanning tunneling microscopy (STM) or photoemission spectroscopy (PES).
4) In order to know the properties considering point 1) and 2), the sample should be well-characterized and invariant (e.g. stable under UHV conditions) to achieve defined and reproducible results.

If these prerequisites are fulfilled or at least partially fulfilled for certain scientific questions, one can increase step by step the complexity by varying the parameters. The experimental setup needs to be arranged to balance the advantages to disadvantages. For instance, vacuum cleaved samples, surface sputtering, annealing cycles or plasma treatment can allocate flat, clean or stoichiometric surfaces.

2.3.2 Obstacles of model catalysis

In case that one can fulfill the prerequisites mentioned above, the model catalytic surface science is a valuable approach. However, concerning the model catalytic conditions and real catalytic conditions, one has to keep in mind that there are some intrinsic differences, namely the pressure, complexity and materials gap. Researchers have been doing efforts to bridge these gaps.[67, 68]

Pressure gap: UHV conditions ($<10^{-12}$ bar) are helpful for model catalytic studies to enable the use of certain surface sensitive investigation tools. For instances, PES and electron diffraction tools are depending on electrons, which would lose their information in non-UHV conditions due to diffuse scattering at gas atoms. Further surface science tools, such as scanning probe microscopy, are also strongly dependent on the cleanness of the surface. In real catalytic applications as TWC or ammonia synthesis much higher pressures are usual (>1bar). So the order of magnitude for this pressure gap amounts at least to 12 decades. Higher pressures might influence the structure of the catalyst and the reaction mechanisms.[69, 70] However, new experimental setups with high pressure (HP) cells enable to partially bridge this gap, e.g. HP-STM and HP-XPS. Quartz crystal microbalance (QCM) allows analyzing mass changes in the ng/cm^{-2} region corresponding to adsorption of gas molecules. Even the investigation of high pressure gas/solid, liquid/solid, liquid/liquid and solid/solid interfaces became possible by sum frequency generation (SFG) vibration spectroscopy.[68, 71]

Complexity gap: The complexity between model and real catalysis is twofold. This duality is based on the material and reaction kinetic differences, which is shown in Fig. 2.9.[72, 73] The first part of this complexity is related to the chemical reaction and its kinetics (*"reaction kinetics gap"*). The second part arises from the compositional and structural properties of the material, hence it is also called the *"materials gap"*.

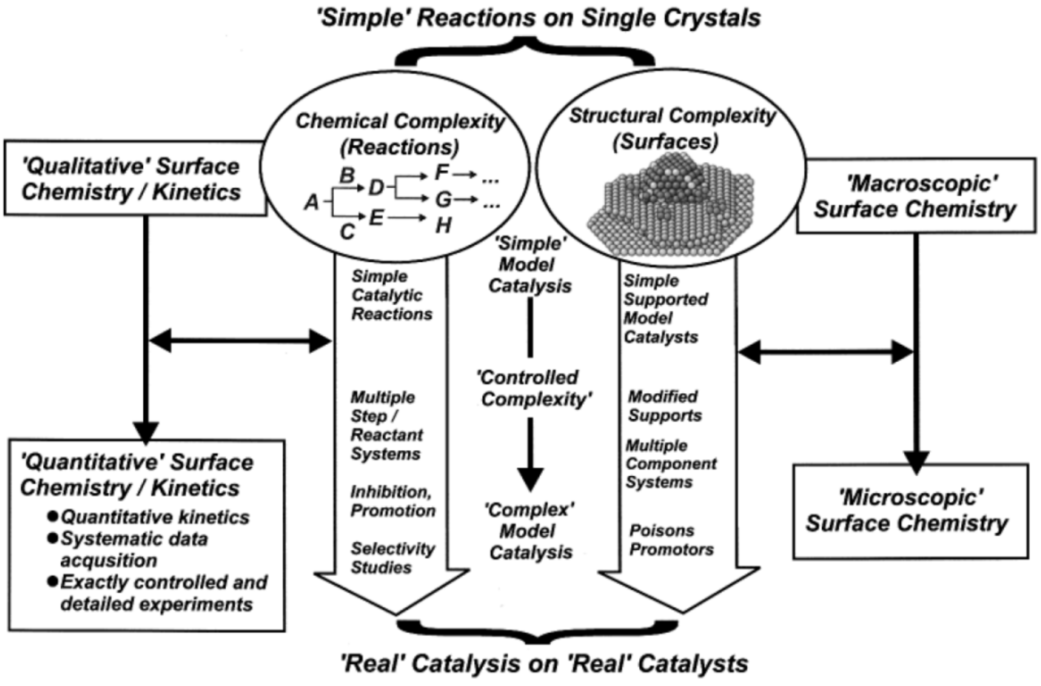

Figure 2.9: Duality of the complexity gap – chemical and structural complexity.[72]

1) *Reaction kinetics gap:* In surface science studies simple reactions, as CO oxidation, are preferentially investigated. However, in real catalytic reactions multiple reactants with several steps and pathways are quiet often involved. Certain pathways can lead to promoting or inhibiting cross talk effects. Interactions of the catalyst materials can

induce further changes to the kinetics, e.g. pathways including the support material, confinement phenomena of the active particle, communication effects.[73] Such modifications of the reaction kinetics lead to an inherent complexity. One approach to achieve an insight to certain reaction steps are molecular beam experiments, profiting from just a single interaction of the reactants with the surface in general.[74, 75] This could be supported by microkinetic models and theoretical mean field and Monte Carlo simulations.[72] Furthermore, macrokinetic mass and heat transport, influencing the activity, selectivity and the behavior during the reaction, have to be considered.

2) *Materials gap:* The materials gap appears as compositional and structural complexity of the catalyst.[72, 73] Firstly, as already mentioned in chapter 2.2.1 the composition and structure of the catalyst has great influence to its behavior. Here, multiple compounds fulfill multifunctional tasks. For example, in TWC a ceramic is used as catalyst carrier, a wash coat consisting of alumina or silica avoids sintering and increases the surface area, CeO_2 supplies oxygen, while on metal clusters (Pt, Rh or Pd) the adsorption and reaction happens. Therefore, it is not surprising that the interplay of these materials becomes more complex. Mixed compounds can have improved abilities as enhanced OSC and oxygen mobility.[57-60] Furthermore, the interaction between oxide support and the active metal cluster can have further effects, e.g. Strong-Metal-Support Interaction (SMSI) and metal-induced gap states (MIGS).[76] Secondly, the structure of a real catalyst is not as simple as for surface science investigations (just a single crystalline material of a certain surface orientation and low defect density is used). Polycrystalline supports with catalytic clusters of a size distribution in the nano scale are common. One has to consider the crystal structures, for example polymorphic materials can have different phases in dependence on the reaction conditions. Furthermore, the shape and porosity of the catalyst plays an important role, considering the macrokinetics. Defects as oxygen vacancies, steps, kinks, corners and grains can have a multiple influence, e.g. as clustering of the metal catalyst or as adsorption sites for reactants are concerned.

The evolution of the structural and compositional complexity of planar supported model catalyst is shown in Fig. 2.10. Starting from single compound and single crystalline materials one can stepwise increase the complexity of the model catalyst to bridge the materials gap. The decoration of a support with metal clusters and the modification of the support by inducing defects are the first challenges.[69, 77, 78] Afterwards, one can investigate multiple compounds and modify the model catalyst by further poisons or promotors.

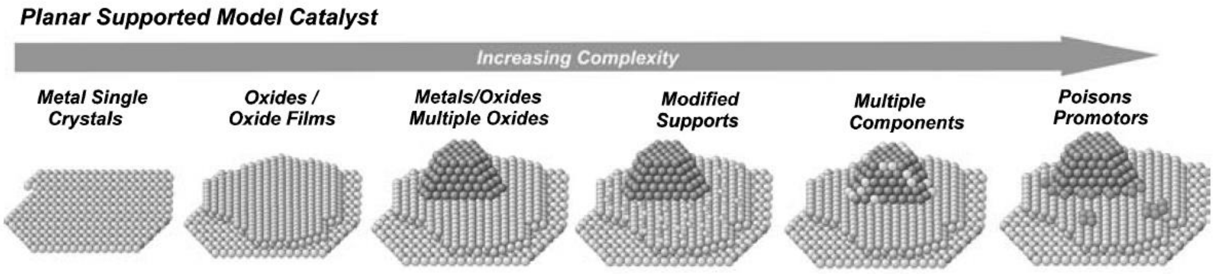

Figure 2.10: Evolution of planar supported model catalysts with increasing complexity.[73]

2.4 State of the art rare earth oxide films on Si

2.4.1 Electronic and structural properties of the rare earth oxides

Previously, a detailed knowledge and extensive characterization is obligatory to correlate structural and chemical properties with the behavior under certain conditions. As already mentioned in the previous chapters, the REOs exhibit some similarities and tendencies within the series of the rare earth elements (REEs). Besides relativistic effects the reason for this behavior is based on the fact that the f-electrons are ineffective in shielding the outer $5d^1$ and $6s^2$ electrons from the nucleus charge, leading to a contraction of the atom with increasing atomic number. In other words, with increasing the nucleus charge by one each time an f-electron is added witin the series of the REE, the imperfect shielding of the nucleus charge results in a stronger contraction of the outer $5d^1$ and $6s^2$ electrons. This phenomenon is called lanthanide contraction. Furthermore, the same microscopic origin is responsible for a similar chemical reactivity. Thus, from all REE the rare earth sesquioxide RE_2O_3 can be formed with the favored 3+ valence state of the rare earth cation due to the three outer $5d^1$ and $6s^2$ electrons.[79, 80] However, REOs of the REO or REO_2 type with a 2+ or 4+ valence state are also existing, e.g.

EuO, YbO, CeO_2, PrO_2, TbO_2. Besides praseodymium dioxide, the deviations of monoxides and dioxides can be explained by the energetically favored unfilled, half-filled or completely filled 4*f* shell. The origin for the 4+ valence state in praseodymium dioxide is controversially discussed. Kotani *et al.*[81, 82] suggested a localized model with “mixed valence compounds” (Pr^{3+}/Pr^{4+}). On the contrary, Petit *et al.*[83] favour the idea of a delocalized model with an “extended f state” and a related Pr4*f*-O2*p* hybridization, whereby the remaining 4*f* electron is localized at the Pr cation site.[84]

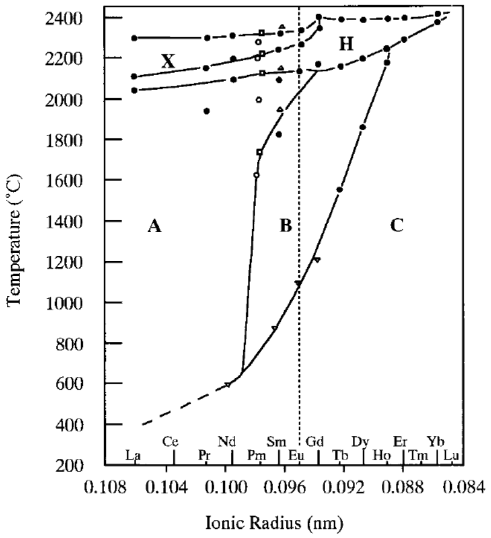

Figure 2.11: Phase diagram of the polymorphic rare earth sesquioxides.[4]

The REOs exhibit several crystallographic structures in dependence on the environmental conditions and their oxygen content. The REO monoxides as EuO and YbO exhibit a NaCl structure which is a face centered cubic structure (fcc). However, the monoxides will not be considered in more detail here. All REOs can form the sesquioxides of the RE_2O_3 stoichiometry for which five different crystal structures are known. This behavior is called polymorphism and is shown in the phase diagram of Fig. 2.11. Besides two high temperature phases H and X (formed above 2000°C), three low temperature phases are known. The A-type phase has a hexagonal (hex) structure with the *P*32/*m* space group corresponding to Hermann-Mauguin notation (Fig. 2.12a). The B-type phase is a monoclinic distortion of the hex structure and has the *C*2/*m* space group. The C-type phase exhibits the cubic (cub) bixbyite structure with the *Ia*3 space group (Fig. 2.12b). With decreasing ionic radius and increasing temperature the phases are thermodynamically favored in the order A-type > B-type > C-type. The phase change to the hexagonal phase occurs by shearing operations, e.g. for Pr_2O_3 at 800°C. In the same order, the

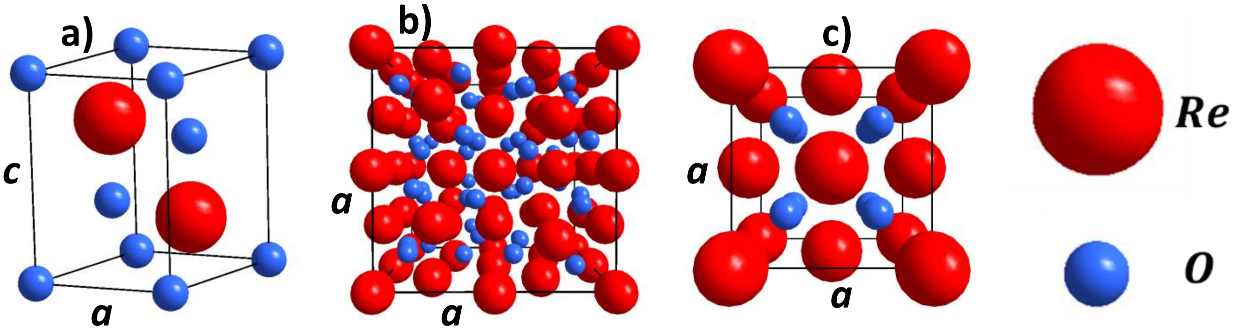

Figure 2.12: Crystallographic structures of the (a) hex-RE_2O_3, (b) cub-RE_2O_3 and (c) REO_2.

density is increasing. Only the middle REOs can form all five polymorphic phases. In contrast, only Ce, Pr and Tb can form the tetravalent rare earth dioxide (CeO_2, PrO_2, TbO_2) and all of them exhibit a fluorite structure, which is a fcc lattice with the F*m*-3*m* space group (Fig. 2.12c).[4]

It should be noted that the fluorite and bixbyite structures are crystallographically closely related to each other. One can transform the fluorite REO_2 to the bixbyite RE_2O_3 structure by doubling the lattice constant of REO_2 and removing one-fourth of all oxygen atoms along non-intersecting $\langle 111 \rangle$ directions.[4, 13, 85] This leads to a slight rearrangement of the rare earth ions and increase of the volume. The lattice constant *a* behaves analog to Vegard's law in a linear relationship, as shown for CeO_2:[13, 86]

$$\boldsymbol{a_{CeO_{2-x/2}} = x * a_{Ce_2O_3} + (1 - x) a_{CeO_2}} \tag{1}$$

The easy transformation of the crystal structure and the reversible valences quite well explain the high oxygen exchange activity and mobility. The phase diagrams for the CeO_x-O_2 and PrO_x-O_2 systems, which are of interest of this thesis, are presented in Fig. 2.13. Here, it is shown that the phases are depending on the temperature and the composition or rather the oxygen pressure. The limitations for the compositions are at x = 1.5 for the bixbyite RE_2O_3 phase and at x = 2.0 for the fluorite REO_2 phase (RE = Ce, Pr). Here, at higher temperatures the fluorite related oxygen rich σ-phase ($RE_2O_{3+\delta}$) and oxygen deficient α-phase ($REO_{2-\delta}$) occur within a wider non-stoichiometric range.[4] In contrast, at lower temperatures several defined intermediate compositions of the generic formula RE_nO_{2n-2m} exist in this oxygen interval, which all exhibit a fluorite related crystal structure and mixed valence states (+3 and +4). These phases arise from ordered oxygen vacancies. The phases of such a homologous series are called Magnéli phases, e.g. also known for V_nO_{2n-1} or Mo_nO_{3n-1}. At atmospheric conditions, the most stable stoichiometry of praseodymia is Pr_6O_{11} (n =12, m = 1), which is even difficult to oxidize under oxygen rich conditions to PrO_2.[87] In contrast, ceria prefers the CeO_2 stoichiometry and its reducibility is sluggish for single crystals.[88]

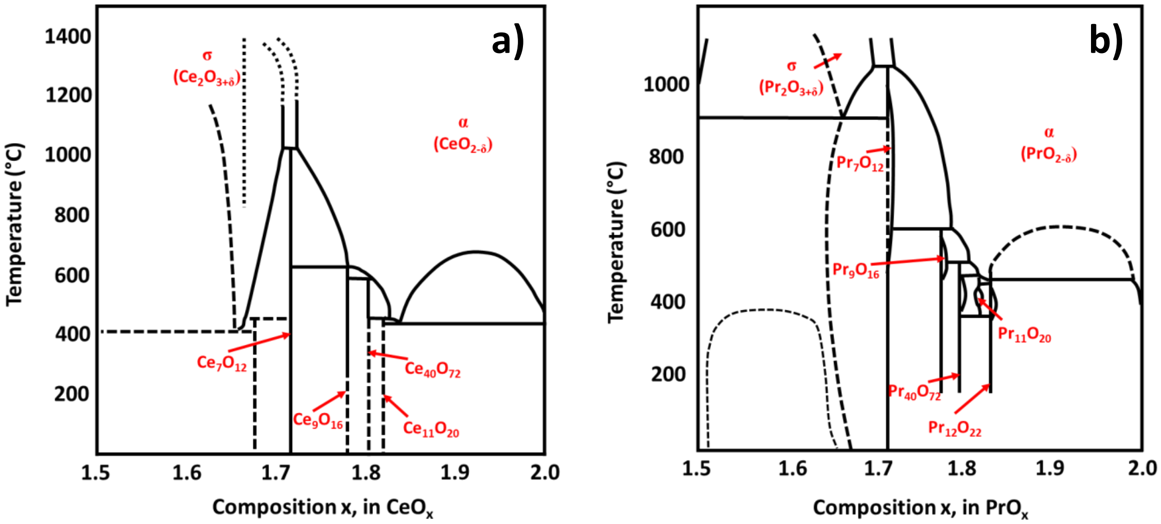

Figure 2.13: Phase diagrams for the systems (a) CeO_x-O_2 and (b) PrO_x-O_2. (Reproduced from [4])

2.4.2 Growth studies of ceria and praseodymia on Silicon substrates

The crystallographic structure and defects (surface and bulk) mainly influence the complex properties of ceria and praseodymia. Therefore, model studies in UHV of these oxides as thin films on a defined flat substrate are of interest. Mainly, due to the microelectronic applications, epitaxial growth studies of REOs on Si substrates were pushed forward. Here, these state of the art depositions of ceria and praseodymia thin films on silicon substrates will be presented. Although, the Si(001) substrate is the most important for CMOS microelectronics, Si(111) substrate was used in the present thesis and will be explained in more detail, because this is the substrate of choice for virtual GaN substrates, where bixbyite buffer oxides are currently investigated.

Growth on Si(001): As already mentioned in a previous chapter CeO_2 and cub-Pr_2O_3 are especially suitable for the growth on Si substrates due to their almost perfect lattice match of only -0.35% and +2.7%, respectively. Nevertheless, CeO_2 as well as cub-Pr_2O_3 grown on Si(001) prefers the (110) orientation.[89, 90] In general, this is an usual behavior for the REOs, which is assigned to two effects. On the one hand Nagata *et al.*[91] stated that Coulombic interactions between the Si(001) surface and the RE-O specie are responsible for this growth orientation.

On the other hand Inoue *et al.*[92] additionally addresses this effect to the lattice alignment showing 1:1 matching in one direction and 3:2 matching in the orthogonal direction. More recent studies with lattice matched $Pr_{0.9}$ $Y_{1.1}O_3$ mixed oxides indicate that the first effect is responsible for the (110) growth orientation.[93] In this model the epitaxial relationship is defined by $RE_2O_3(110);\langle 010\rangle||Si(001);\langle 110\rangle$, so that the rectangle oxide (110) base is 45° tilted to the quadratic Si(001) base. This leads to two orthogonal in-plane oriented domains, caused by the likewise orthogonal Si$(2x1)$ dimer rows of neighboring terraces. Furthermore, REO_2 type oxides less favorably grow in the $REO_2(110)||Si(001)$ orientation, because additional unsaturated oxygen bonds and interface charges occur by the 3:2 matching relation but 2:1 O/RE ratio.[2] It is reported that (001) oriented CeO_2 is grown without buffer layer on Si(001) at room temperature by depositing the cerium metal with additional O_2 supply.[94] Furthermore, REO(001) can also be grown on Si(001) with a cube-on-cube orientation using an ultra-thin yttria-stabalized zirconia (YSZ)[95, 96] or strontium titanate (STO)[91] buffer layer.

<u>Growth on Si(111):</u> Although, it was shown that $CeO_2(111)$ can be also grown on oxidized Si(001),[97] it is more straightforward to grow it on Si(111). First growth studies were published by Inoue *et al.*[98] via molecular beam epitaxy (MBE) and by Koinuma *et al.*[99] via pulsed laser deposition (PLD). Inoue additionally found that higher growth rates are better for the crystalline quality by preventing surface oxidation.[100] This kind of oxidation even occurred by using the above mentioned buffer layers on Si(001) substrates due to oxygen diffusion.[92, 101] Detailed investigations support a growth mechanism assuming post coverage reaction of the first CeO_2 layers with the Si interface. A transmission electron microscopy image and the corresponding interface formation model is presented in Fig. 2.14.[102, 103]

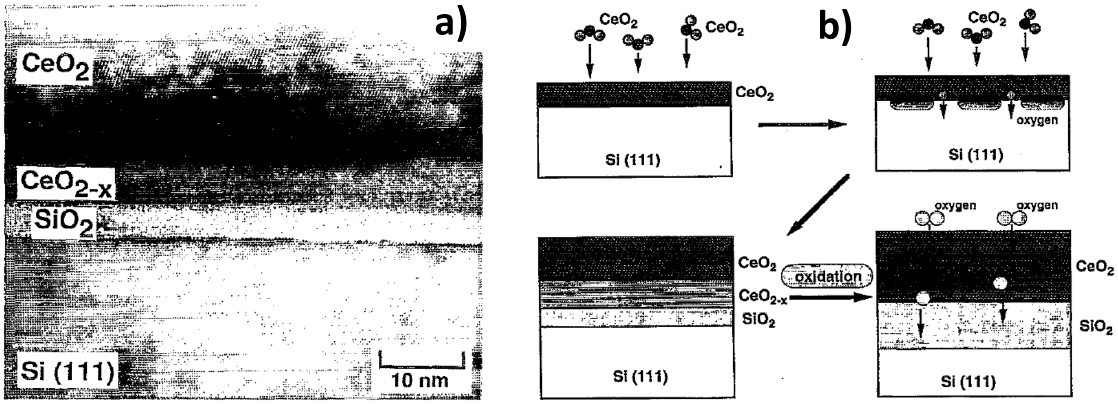

Figure 2.14: (a) $CeO_2(111)$/Si(111) TEM image and (b) interface formation mechanism.[102]

Well-defined sharp $CeO_2(111)$ /Si(111) interfaces were achieved by depositing pure cerium metal with ozone (O_3) supply.[104, 105] Another recent approach with reactive MBE has shown $Ce_2O_3(111)$ growth of large grain size on chlorine passivated Si(111) surfaces.[106] The in-plane orientation of the $CeO_2(111)$/Si(111) stacking was investigated and a corresponding interface model was proposed by Nagata *et al.* (Fig. 2.15).[107] A type-B $CeO_2(111);\langle\bar{1}10\rangle||Si(111);\langle 1\bar{1}0\rangle$ epitaxial relationship was found, which corresponds to a 180° rotation around the (111) axis with respect to the Si substrate orientation.

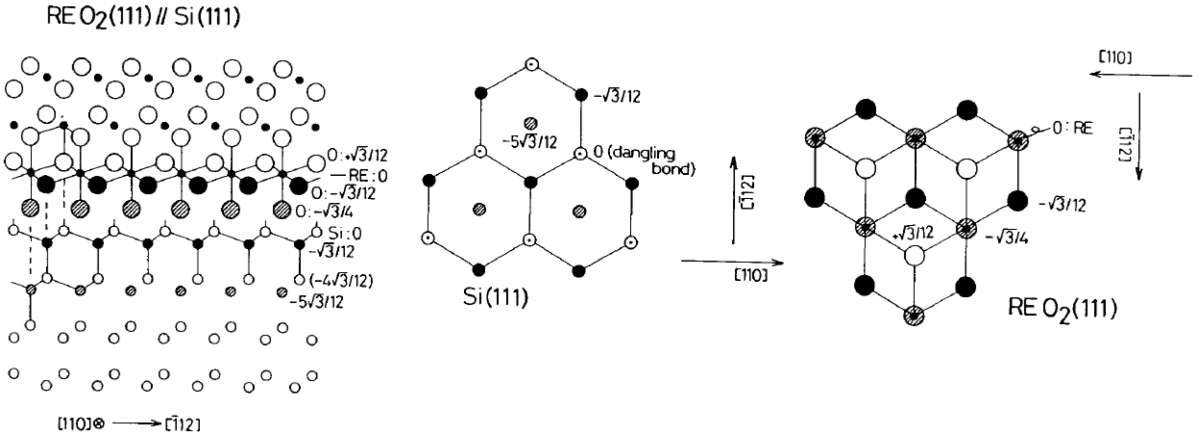

Figure 2.15: $CeO_2(111)$/Si(111) interface model.[107]

The growth of single crystalline praseodymia films on Si(111) emerged as more complicated due to polymorphism and the higher influence of the oxygen concentration leading to different phases. On Si(111) Pr_2O_3 grows hexagonal with a hex-$Pr_2O_3(0001);\langle 11\bar{2}0\rangle||Si(111);\langle 1\bar{1}0\rangle$ orientation.[24, 108] The hexagonal phase is induced by the smaller lattice mismatch of less than +0.5% for hex-$Pr_2O_3(0001)$ compared to +2.7% for cub-$Pr_2O_3(111)$. With a proper deposition rate, layer-by-layer growth occurs and leads to an initial pseudomorphic growth.[109, 110] Although, Pr_2O_3 of the type-A phase is called hexagonal it exhibits a threefold symmetry arising from the space group P32/m mentioned in chapter 2.4.1. Here, two in-plane growth orientations are possible. In particular, the initial growth stage investigated by scanning tunneling microscopy shows preferential triangular islands of a certain orientation on the (7×7)-Si(111) reconstruction (Fig. 2.16a).[111] Jeutter *et al.*[112, 113] generated two growth models where the first oxygen layer always positions on top of the Silicon atom, but the following praseodymium layer has the opportunity to occupy the position above the H3 or T4 site. It was shown by X-ray diffraction and corroborated by theoretical calculation that the model with praseodymium ions above the T4 site is correct (Fig. 2.16b). This explains the two different growth models. After the initially pseudomorphic layer by layer growth mode, a successively relaxation from 4nm up to 12nm thickness of the hex-$Pr_2O_3(0001)$ film occurs.[109] This is accompanied by an increasing roughness of the surface (Stranski-Krastanov growth mode) and decreasing average domain size (plastic relaxation by defect insertion).[66]

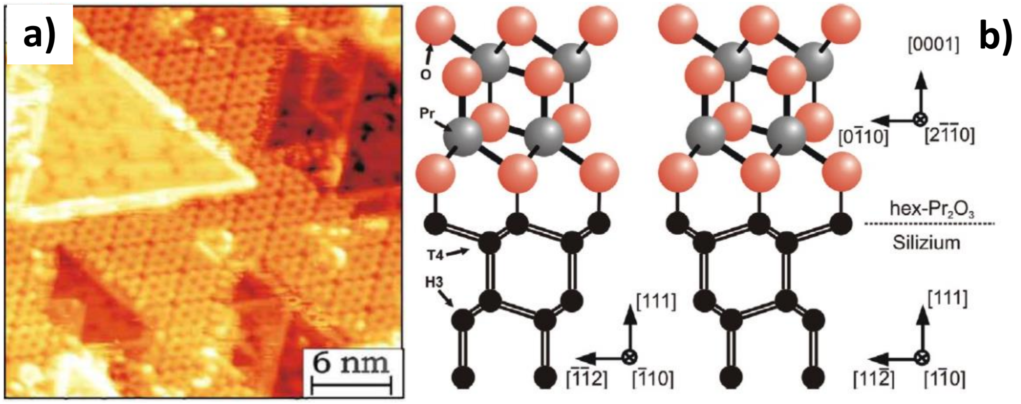

Figure 2.16: (a)[111] $Pr_2O_3(0001)/Si(111)$ initial growth STM image and (b)[113] 2 different interface models.

Preparation methods via N_2 or low pressure O_2 annealing were found to induce phase transformation from hex-$Pr_2O_3(0001)$ films to single crystalline cub-$Pr_2O_3(111)$ with an exclusive type-B oriented epitaxial relationship cub-$Pr_2O_3(111);\langle 11\bar{2}0\rangle || Si(111);\langle \bar{1}10\rangle$.[114, 115] This hex-cub phase transformation goes along with a stacking order rearrangement from ACACAC… (for hex-$Pr_2O_3(0001)$ along $\langle 0001\rangle$) to ABCABC… (for cub-$Pr_2O_3(111)$ along $\langle 111\rangle$). Furthermore, an interface oxidation occurs by oxygen diffusion through the oxide layer, forming a praseodymium silicate and SiO_x interface layer (similar to the growth of CeO_2 films).[114] It was also achieved to grow directly $PrO_2(111)$ films by PLD.[116] As the bixbyite cub-Pr_2O_3 bears a closely crystallographic relationship to the fluorite PrO_2 phase, the preparation of the later phase with a high degree of oxygen deficiency became possible by annealing under oxygen atmosphere.[117] It is reported that a higher oxygen concentration in the $PrO_{2-\delta}$ film can only be achieved by oxygen plasma treatment.[87, 118] Considering that for future catalytic studies the oxygen exchange becomes important, one should be aware of the oxidation and reduction influence on the film crystallinity. A two-column model with laterally coexisting praseodymia phases was developed to describe the structural and morphological changes of these praseodymia films with varying oxygen concentration.[119, 120]

Chapter 3

Experimental Part

3.1 Sample Preparation

3.1.1 Silicon substrate

4 inch, 525 µm thick, on-oriented (±0.5°) Si(111) wafers grown by Czochralsky process were used as substrate (supplier Siltronic). The silicon is p-type (boron-doped) with a resistivity of 5-15 Ωcm. Before introducing the wafers into the MBE chamber, the sample was treated by a wet chemical procedure in 6 steps:[121]

1) 10 min etching in a 4:1 mixture of 95-97% concentrated sulphuric acid (H_2SO_4) and 30% hydrogen peroxide (H_2O_2). The so called piranha acid reaches a temperature of about 80°C, due to its exothermic reaction. By this process the organic contaminants are removed and a defined SiO_2 layer is formed.
2) 1 min rinsing in de-ionized water to remove the residual sulfuric acid.
3) 1 min etching in 50% hydrofluoric acid (HF) diluted in de-ionized water with a ratio of 1:20 to remove the silicon oxide from the surface.
4) 5 min rinsing in de-ionized water to remove the residual hydrofluoric acid.
5) 30 min etching in a 40% ammonia fluoride (NH_4F) solution. By this soft etching step a flattening and hydrogen termination of the Si(111) surface occurs.
6) 10 min displacement purging by de-ionized water in order to avoid fluorine contaminations on the surface and consequently in the oxide films.

Subsequently, the sample was introduced to the UHV ambience within 5 min in order to keep the clean, flat and hydrogen terminated Si(111) surface and to avoid re-oxidation. In the load-lock the sample was degassed at 200°C to prevent water contamination in the UHV system. To achieve the (7×7) reconstruction of the Si(111) surface, the substrate was heated up to 750°C for 5 min in the UHV chamber. Fig. 3.1a shows the surface model of the reconstruction. In order to control this formation, reflection high energy electron diffraction (RHEED) was in-situ monitored. Fig. 3.1b demonstrates the RHEED pattern along the Si$[110]$ azimuth. The solid and dotted arrows mark the integral and fractional streak lines, respectively.

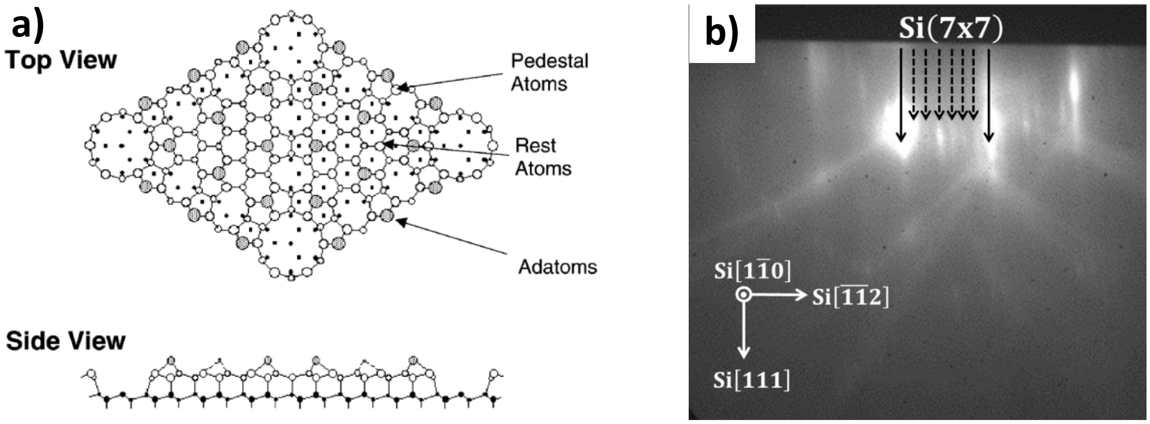

Figure 3.1: (a)[122] Dimer adatom stacking-fault (DAS) model from Takayanagi *et al.*[123] and (b) RHEED image of the (7 × 7)-Si(111) reconstruction.

3.1.2 Oxide deposition

For the growth of ceria and praseodymia thin films, the molecular beam epitaxy (MBE) deposition technique (MBE *DCA 600* chamber) was used. Fig. 3.2 shows its configuration and a photo. The base pressure of $3*10^{-10}$ mbar is kept by a pumping system consisting of membrane pump, a turbo molecular pump and a cryo pump. The principle of the MBE technique is based on a focused electron beam impinging on the target material (Pr_6O_{11}, CeO_2) in graphite crucibles. The electron beam is generated by an electron gun with a certain acceleration voltage (U_B = 10kV) and emission current (I_E = 20-70mA). In order to scan over the oxide for a homogenous heating the electron beam sweeping is controlled by an electromagnetic field. The impinging electrons transfer their kinetic energy to the target and heat it up. With this technique a temperature higher than 2000°C is generated, which is necessary to evaporate the oxides. Thereby, a molecular beam consisting of different metal oxide species, pure metal and oxygen is released to the UHV of the growth chamber. During the deposition the pressure rises typically up to $1*10^{-6}$ - $1*10^{-5}$ mbar, disabling to grow directly high quality single crystalline CeO_2 on Si. Therefore, the double-walled MBE chamber was additionally cooled by liquid nitrogen. The deposition rate (3 nm/min) is controlled and stabilized by a quartz crystal microbalance (QCM) system. For the growth of mixed ceria-praseodymia samples, both materials were co-evaporated keeping a constant deposition rate (6 nm/min) for all mixtures. The sample itself is rotated (20 rpm) to achieve a homogenous oxide film thickness over the 4 inch Si wafer. The oxide crystallizes once the molecular beam reaches the heated substrate surface (625°C). For in-situ monitoring of the epitaxial growth process, the chamber is equipped with a RHEED tool. Compared to the chemical vapor deposition, which is used for mass production purposes, the MBE enables an atomic controlled deposition with in-situ monitoring of the growth process. Furthermore, MBE growth is more flexible than CVD deposition, as no need for chemical precursor development is necessary, making the MBE technique suitable for fundamental research studies. State-of-the-art growth studies of praseodymia and ceria are presented in chapter 2.4.2. For more information concerning MBE technique and crystal growth, the reader is referred to the literature.[124-127]

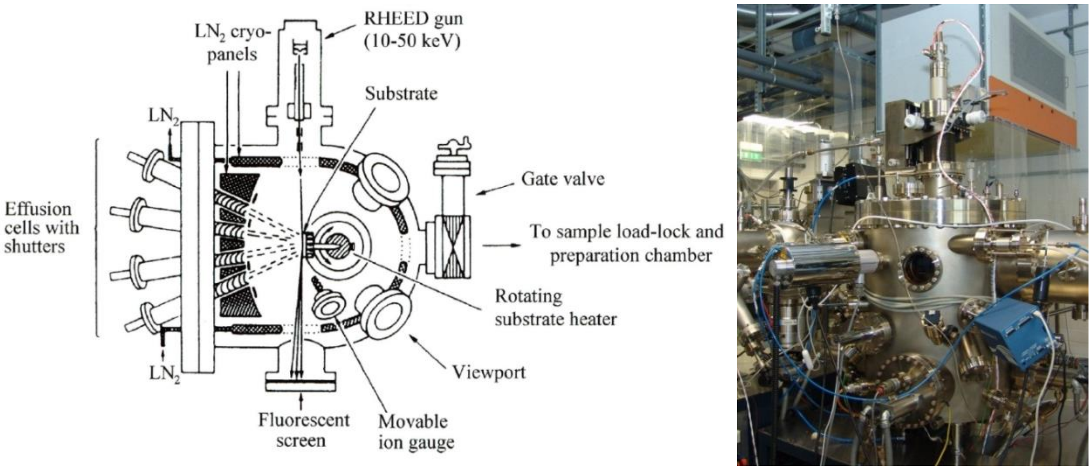

Figure 3.2: (a)[128] Schematic drawing of a UHV chamber setup and (b) a picture of the MBE chamber for oxide deposition at IHP equipped with electron guns, effusion cells, RHEED system and QCM controller.

3.1.3 Phase transformation and oxidation process

As already mentioned in chapter 2.4.2, two different ex-situ processes were applied for the phase transformations:

1) The hex-Pr_2O_3 to cub-Pr_2O_3 transformation proceeded in 1 atm N_2 (purity 6.0) at 600°C for 5 min.[114]
2) The oxidation from hex-Pr_2O_3 to $PrO_{2-\delta}$ proceeded in 1 atm O_2 (purity 5.5) at 400°C for 30 min.[117] The mixed oxides where oxidized in the same manner.

For all processes a horizontal furnace (model *PEO 601*) for 4 inch wafers was used (Fig. 3.3).

Figure 3.3: Picture of the PEO 601 furnace.

3.2 Sample Characterization

3.2.1 X-ray photoelectron spectroscopy

3.2.1.1 X-ray photoelectron spectroscopy setup

X-ray photoelectron spectroscopy (XPS) was used in the present thesis for the chemical analysis of the ceria and praseodymia thin films. In detail, the stoichiometry of the mixed oxides and the valence state was determined by this technique. Therefore, as-grown samples were in-situ analyzed with a photoelectron spectroscopy tool connected to the MBE (Fig. 3.4). As excitation energy the characteristic $\mathrm{MgK}_{\alpha1,2}$ (E_{exc} = 1253.6 eV) fluorescence lines were used from a dual anode X-ray source (*04-548 Physical Electronics*). This energy causes the emission of the praseodymium, cerium and oxygen core level electrons, which are analyzed by a hemispherical detector (*Scienta Phoibos 100 Specs*) at a detection angle of 45° in the constant pass energy mode.

The temperature dependent measurements were performed with $\mathrm{AlK}_{\alpha1,2}$ excitation energy (E_{exc}=1486.6eV) and a *PHI-5000 VersaProbe II* tool from *Physical Electronics*, which is an ex-situ stand-alone tool. The data were analyzed via background subtraction and peak signal fittings by the *CasaXPS* program.

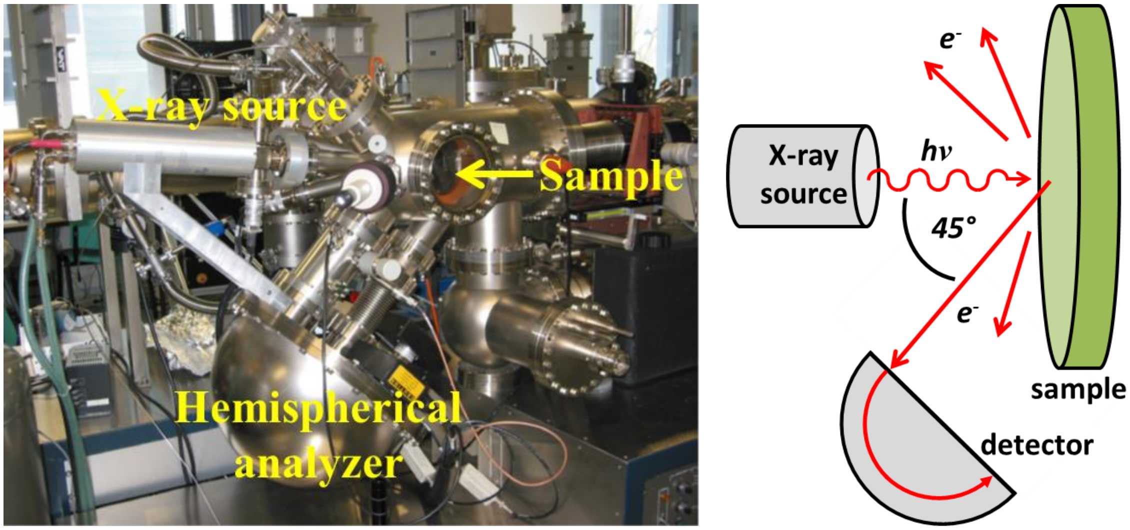

Figure 3.4: Picture and sketch of XPS setup mounted to the MBE cluster for in-situ measurements at IHP.

3.2.1.2 *Qualitative analysis*

The chemical sensitivity of XPS is related to the characteristic photoemission lines of the investigated material which enables a qualitative statement of the sample´s composition. Therefore, the binding energy E_{bin} of the photoemission lines or rather the kinetic energy E_{kin} of the photoelectrons has to be analyzed. The transfer of the photon energy E_{exc} allows the electron to overwhelm the vacuum energy level E_{vac} and the effective binding energy $E_{bin,eff}$, leaving a hole behind. It is thus important to note that XPS is an ion spectroscopy, because the invasive photoelectric effect[129] leaves the atom in an ionized state. Moreover, for analyzing E_{kin} the work function of the spectrometer φ_{sp} has also to be considered (Fig. 3.5a). Thus, the measured E_{kin} of the ejected electron is:[130]

$$\boldsymbol{E_{kin} = E_{exc} - E_{bin,eff} - e\varphi_{sp}} \qquad (3.01)$$

The effective binding energy is referenced to the Fermi energy E_F and includes several terms:

$$\boldsymbol{E_{bin,eff} = E_{bin} - \Delta E_{chem} - \Delta E_{Mad} - \Delta E_{ext} - \Delta E_{int}} \qquad (3.02)$$

Here, E_{bin} is the binding energy related to the Fermi level, ΔE_{chem} is the energy difference due to the chemical state of the atom (e.g. partial charge) and ΔE_{Mad} is the Madelung term considering the electrostatic Coulomb potential of the material. Within the material, also extra-atomic effects occur by interaction of the photoelectron with extrinsic electrons, resulting in ΔE_{ext}, e.g. by inelastic plasmon scattering. Furthermore, the “sudden approximation” or “frozen orbital approximation” predicts that the electron excitation is fast compared to the electronic/nuclear relaxation. It is assumed that the orbital energy does not change during the ionization process, which is called Koopmans’ theorem. This assumption is made when XPS spectra are analyzed in terms of *electron spectroscopy for chemical analyzis* (ESCA). However, this does not consider several intra-atomic relaxation effects leading to additional satellite peaks and shifted energy ΔE_{int}, since the initial state is different from the final state:

1) The electronic excitation of the atom from the initial state creates an ionized atom whose electronic configuration might relax. Thus, the final state might change on the time scale of the photoelectron emission process.
2) If during the excitation of the photoelectron a further valence electron is excited to a higher bonded energy state the energy comes from the photoelectron reducing its E_{kin}. This is called shake-up process.

3) For the shake-off process also a secondary valence electron might be involved, which becomes excited to a non-bonded state or rather becomes emitted.
4) Also shake-down processes are possible, which is the case when an empty energy state exists below the Fermi level. Thus, one electron from a higher state can occupy this level causing a higher kinetic energy of the photoelectron by screening the core charge.
5) The Auger effect is based on a three electron process. After the core hole is left behind, another electron from a higher energy state can fall in this lower energy state releasing energy, which is able to eject another third electron.
6) Spin-orbit interactions are leading to a splitting of the respective photoemission line contributions. The spin of an unpaired electron $\vec{s}$ (remaining electron from the core level after photoelectron emission) couples with the magnetic field induced by the angular momentum $\vec{l}$ of the electron. So the total angular momentum $\vec{j} = \vec{l} \pm \vec{s}$ is resulting, depending whether the spin is parallel or antiparallel to $\vec{l}$. An example is given by photoemission line splitting $p_{3/2}$, $p_{1/2}$; $d_{5/2}$, $d_{3/2}$; and $f_{7/2}$, $f_{5/2}$. For more complex situations (heavier atoms), the interaction of the total angular momentum of the atomic electron configuration with the spin of the hole state needs to be considered.

For a more detailed insight into XPS interpretations and analysis, several books can be consulted.[131, 132]

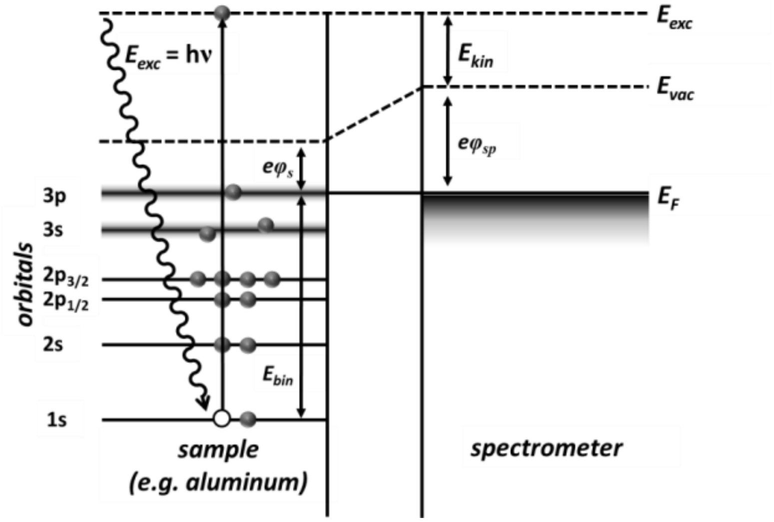

Figure 3.5: Schematic drawing of the energy levels of the analyzed atom in relation to the spectrometer. The Koopmans´ theorem is indicated predicting the orbital energy being equal to the ionization energy.

3.2.1.3 Quantitative analysis

For a quantitative analysis of the photoelectron peaks and their intensity the underlying photoemission process has to be considered in a three-step model:[132]

1) Photon adsorption and ejection of the photoelectron
2) Matrix transition to the sample surface
3) Passing the sample surface to the vacuum

However, only the first two steps will be discussed considering the purpose of stoichiometry determination. Furthermore, the spectrometer influence to the photoelectron intensity is pointed out. For a flat sample, which is uniformly illuminated and analyzed with a small detector aperture, the intensity I_{Anl} of a photoemission line from element A and subshell nl in the XPS spectra is given by:[131]

$$\boldsymbol{I_{Anl} = \sigma_{Anl}(E_{exc}) * L_{Anl}(\theta) * \lambda_M(E_{Anl}) sin\alpha * G(E_{Anl}) * D\left(E_{pass}\right) * J_0 * N_A} \qquad (3.03)$$

Here, the parameters are the absolute cross-section $\sigma_{Anl}(E_{Exc})$, the asymmetry function $L_{Anl}(\theta)$, the inelastic mean free path (IMFP) $\lambda_M(E_{Anl})$, the étendue $G(E_{Anl})$, the detector efficiency $D(E_{pass})$, the X-ray flux to the sample J_0 and the atomic density N_A, which has to be determined for obtaining the stoichiometry. Furthermore, α is the take-off angle from the photoelectrons with respect to the surface. For homogenous binary materials the intensity ratio I_A/I_B between the elements A and B simplifies by reducing to:[131]

$$\boldsymbol{\frac{I_{Anl}}{I_{Bnl}} = \frac{\sigma_{Anl}(E_{Exc}) * L_{Anl}(\theta) * \lambda_M(E_{Anl}) * E_{Bnl} * N_A}{\sigma_{Bnl}(E_{Exc}) * L_{Bnl}(\theta) * \lambda_M(E_{Bnl}) * E_{Anl} * N_B}} \qquad (3.04)$$

The residual parameters are explained in the following in more detail:

<u>Photon adsorption and ejection of the photoelectron:</u> In particular, the emission process of the photoelectron is based on the photoelectric effect. The photoelectron emission is schematically shown in Fig. 3.5. For the interaction of the X-rays with the electrons the differential cross-section $d\sigma_{Anl}/d\Omega$ from the element A and the subshell nl is given by:[133]

$$\boldsymbol{\frac{d\sigma_{Anl}}{d\Omega} = \frac{\sigma_{Anl}}{4\pi} L_{Anl}(\theta) = \frac{\sigma_{Anl}}{4\pi}\left[1 + \frac{1}{2}\beta_{Anl}\left(\frac{3}{2}sin^2\theta - 1\right)\right]} \qquad (3.05)$$

$L_{Anl}(\theta)$ is the asymmetry function with the asymmetry parameter β_{Anl}, which describes the angular distribution of the relative intensities depending on the angle θ between incident photon beam and electron emission direction. Scofield gives tabulated values for $d\sigma_{Anl}/d\Omega$ with MgK_α and AlK_α as excitation energies E_{exc}.[134] Furthermore, Reilman *et al.*[135] published β_{Anl}

values for certain atomic numbers Z and E_{exc} (ZrM_{ζ}, MgK_{α} and AlK_{α}). If the electrons are detected at an angle of 54.7° (This "magic angle" is used for most XPS set-ups) in relation to the excitation direction of the photon, the asymmetry function becomes negligible for most purposes.

<u>Matrix transition to the sample surface:</u> Although the X-ray attenuation length of the used E_{exc} is much longer than the thickness of all considered samples of this thesis, the information depth is limited to several nm by the inelastic scattering of the photoelectrons. Therefore, XPS is a surface sensitive investigation tool. After the photoemission the electrons travel with a certain E_{kin} (initially depending on E_{Anl}) through the material before transition through the surface to the vacuum. Being more concrete, along the way through the matrix M, inelastic scattering can occur causing a decrease of the E_{kin}. For example, interactions with plasmons from an occupied conduction band are responsible for the limitation. The inelastic mean free path λ_M (which is the length without an inelastic interaction) and the take-off angle α between sample surface and detection direction are determining the sampling depth d_M:

$$\boldsymbol{d_M = 3\lambda_M sin\alpha} \tag{3.06}$$

This equation is defined in such a way that 95% of the photoelectrons (including inelastic scattered electrons in the background of the elastic photoelectron signal) originate from a depth of $3\lambda_M$ with a 90° take-off angle. Furthermore, the IMFP $\lambda_M(E_{kin})$ depends on the E_{kin} of the electrons and several material specific parameters. Nevertheless, the IMFP of certain material classes show a similar behavior depending on the energy. This is shown by the "universal curve" in Fig. 3.6 derived from characteristic photoemission lines of metals. The minimum of the curve is in between 50-100eV, due to efficient plasmon interactions in that energy range.

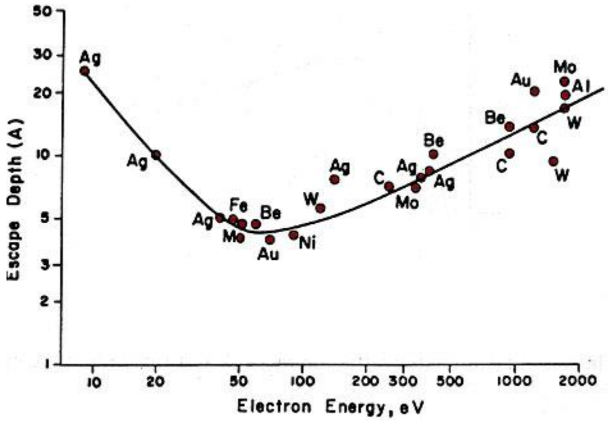

Figure 3.6: "Universal curve" of the IMFP in dependence on E_{kin} for several metals.[136]

For a specific measurement, the universal curve is not precise enough and the IMFP needs to be calculated by the TPP-2M equation developed by Tanuma, Powell and Penn (which is considered to be a good estimation in the energy range from 50-2000eV)[137, 138]:

$$\boldsymbol{\lambda_M(E_{kin}) = \frac{E_{kin}}{E_P^2[\beta\, ln(\gamma E_{kin}) - (C/E_{kin}) + (D/E_{kin}^2)]}} \qquad (3.07)$$

The parameters β, γ, C, D and U are given by:

$$\boldsymbol{\beta = -0.1 + 0.944/(E_P^2 + E_G^2)^{0.5} + 0.069\rho^{0.1}} \qquad (3.07a)$$

$$\boldsymbol{\gamma = 0.191\rho^{-0.5}} \qquad (3.07b)$$

$$\boldsymbol{C = 1.97 - 0.91U} \qquad (3.07c)$$

$$\boldsymbol{D = 53.4 - 20.8U} \qquad (3.07d)$$

$$\boldsymbol{U = N_V/M = E_P^2/829.4} \qquad (3.07e)$$

Furthermore, several material specific parameters are needed: the free-electron plasmon energy ($E_P = 28.8(N_V\rho/M)^{0.5}$), the band gap ($E_G$), the molecular weight (M) and the number of valence electrons (N_V). However, the parameters are not so straight forward to determine, because different values can be found in literature or might simply not yet be determined for novel complex materials. Especially, for E_G and N_V high uncertainties exist.[139]

<u>Spectrometer influence:</u> After the photoemission, matrix transition and passing the sample surface to the vacuum, the photoelectrons are collected by the analyzer to determine their kinetic energy E_{kin} and intensity I.

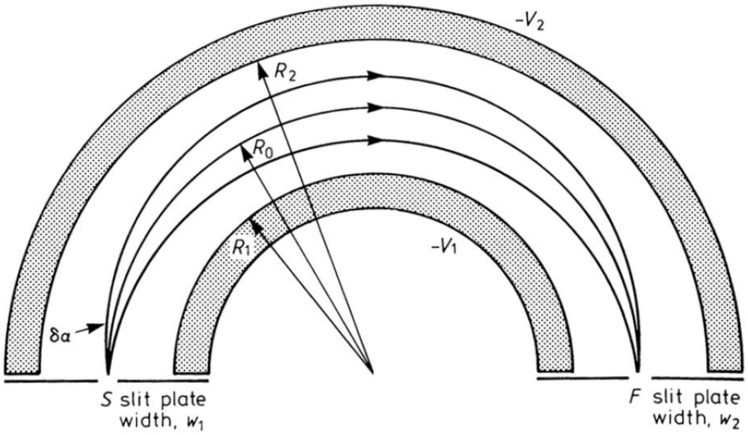

Figure 3.7: Schematic cross-section of a concentric hemispherical analyzer (CHA).[131]

Before, an electro-optic lens system images the sample plane on the entrance plane S, defines the probed area and the acceptance angle. Furthermore, an electric field U_0 accelerates/decelerates the electrons. In series with the concentric hemispherical analyzer (schematic drawing of the CHA is shown in Fig. 3.7), only electrons of a certain energy (pass energy E_{pass}) are filtered and detected. Here, the voltages $-V_1$ and $-V_2$ are applied to the two hemispheres with the radii R_1 and R_2. At the median radius R_0 the equipotential is $V_0 = (V_1R_1+V_2R_2)/2R_0$. The electrons entering the slit plate tangential at the scource S with a certain E_{pass} are focused to the point F. Due to the divergence angle $\delta\alpha$ also electrons with an energy deviation ΔE_{pass} from the R_0 trajectory are detected. By biasing $-V_1$ and $-V_2$, electrons with a defined E_{pass} can be selected to pass F to the detector. The lower E_{pass} is, the better the energy resolution and the lower the signal intensity becomes. Both are constant over the whole spectrum in the constant pass energy mode, since the electric field U_0 is scanned and not V_1/V_2. Thus, the analyzed area $A(E_{pass})$ and the detector efficiency $D(E_{pass})$ are kept at a constant value k, which means they are independent of the investigated core level E_{Anl}. Therefore, the étendue of the analyzer $G(E_{kin})$ becomes just dependent on the transmission efficiency $T(E_{kin})$, which shows a reciprocal proportionality to the kinetic energy of the electrons:[131]

$$\boldsymbol{G(E_{kin}) = k * T(E_{kin}) = k * E_{kin}^{-1}} \qquad (3.08)$$

This relationship explains the overall shape of a XPS spectrum measured by a CHA in constant pass energy mode. Certainly, the constant pass energy mode makes it possible to quantitatively compare XPS peaks from different energy ranges of the spectrum.

3.2.2 X-ray scattering

3.2.2.1 X-ray scattering setup

X-ray scattering experiments are a non-destructive way to analyze the crystallographic structure of a material which enables conclusions about the physical and chemical structure-property relationship. Here, these experiments were performed to analyze the crystal structure, the thickness, the temperature dependent oxygen release, the strain and potential foreign phases of the combined cerium-praseodymium oxide thin films. Different diffraction tools are used at IHP laboratories for this thesis, namely the diffractometers *DMAX 1500* (Fig. 3.8a) and the *SmartLab* from *Rigaku* (Fig. 3.8b). For standard specular investigations in Bragg-Brentano configuration the *DMAX 1500* was used. For asymmetric and temperature dependent measurements the *SmartLab* was needed. Both tools exhibit a rotating anode creating the characteristic CuK$_\alpha$ radiation ($\lambda = 0.154\ nm$) with high intensity.

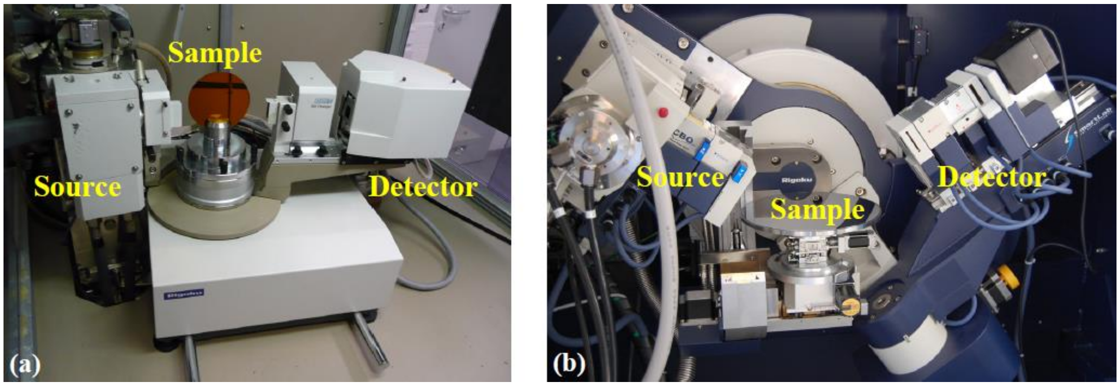

Figure 3.8: Pictures of (a) *DMAX 1500* and (b) *SmartLab* used at IHP laboratories.[128]

Furthermore, synchrotron based scattering experiments were performed at the Doris III positron storage ring in the Hamburger Synchrotronstrahlungslabor (HASYLAB) of the Deutsches Elektronen-Synchrotron (DESY), which is part of the Helmholtz association (Fig. 3.9a). Synchrotron radiation facilities exhibit the advantages of high brilliance (resulting in a high intensity and high resolution) and tunable photon energies. In the present thesis, synchrotron radiation (SR) was needed to find low intense defect inclusions by specific Bragg reflections in grazing incidence (GI) geometry. For the creation of the X-rays, a wiggler was used at the beamline W1. Due to a higher oscillation deflection of the positrons by such a dipole magnet array, higher photon energies can be reached in comparison to undulators. However, the brilliance of wigglers is smaller caused by the higher divergence and spectral bandwidth. For the diffraction experiments, an energy of $E = 10.5\ keV$ ($\lambda = 0.118\ nm$) was used. The X-ray beam was

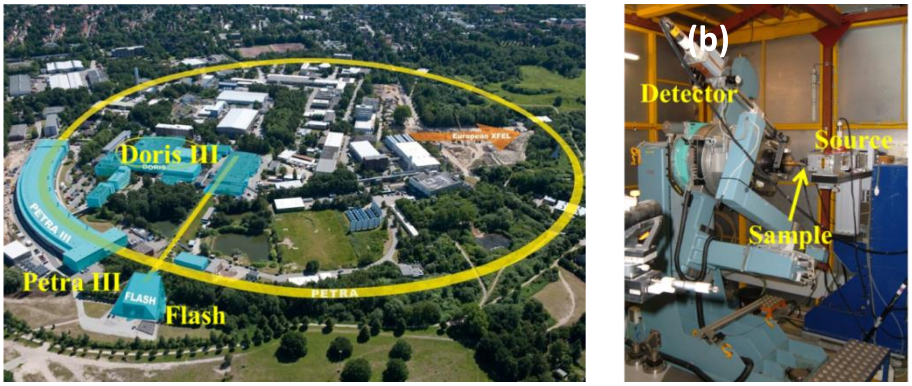

Figure 3.9: (a) Aerial photo from Doris III, Petra III and Flash of the DESY in Hamburg and (b) picture of the six-circle goniometer at the entrance of the synchrotron beam.

monochromatized by Si(111) crystals, and cut to a certain beam size by a horizontal and vertical slit system before scattered at the sample. Furthermore, a six circle goniometer was used for the positioning of the sample and a linear MYTHEN detector scanned the diffracted X-rays (Fig. 3.9b).

A proper investigation method was assigned to each scientific question. The purpose of the respective analysis, the corresponding X-ray scattering techniques and employed investigation tools are summarized in Tab. 3.1. Further details on the X-ray scattering experiments performed in this thesis are explained in the following chapters. Details about X-ray diffraction (XRD) and X-ray reflectivity (XRR) can be found in the literature.[140, 141]

purpose	**technique**	**Tool**
Off-plane lattice spacing	specular θ-2θ scans	Rigaku DMAX 1500
Thin film thickness	XRR	Rigaku DMAX 1500
T dependent off-plane lattice spacing	T dependent θ-2θ scans	Rigaku SmartLab
Crystal phase determination	pole figure mapping	Rigaku SmartLab
Strain determination	$cos^2\chi$ method	Rigaku SmartLab
Stacking twin detection	GIXRD l-rod scans	Beamline W1
Bixbyite inclusion detection	GIXRD in-plane scans	Beamline W1

Table 3.1: Table of the purposes of the respective analysis, the corresponding applied scattering technique and the employed investigation tool.

3.2.2.2 X-ray diffraction

XRD is based on elastic scattering of X-rays with the periodic electron distribution in the investigated material (e.g. interatomic distance in a crystal: 0.15 - 0.4 nm). If the wavelength (e.g. wavelength of X-rays: 0.01 - 10 nm) is in the order of this periodicity and certain geometric conditions of incident and scattered beam are applicable, the corresponding interference of the electromagnetic wave may be constructive. In dependence on the crystallographic structure, these conditions can be fulfilled for several geometries resulting in a diffraction intensity pattern in reciprocal space and enabling conclusions about the real space crystal structure. The following discussion is based on the kinematical theory of diffraction, neglecting multiple scattering events, which is a good assumption for non-ideal crystal lattices and due to the inefficient scattering of X-rays by matter. For an unpolarized and monochromatic beam scattered at a crystal, the intensity of the interference is given by:

$$\boldsymbol{I = I_e \cdot F^2 \cdot G^2} \qquad (3.09)$$

Here, I_e is the form factor giving the scattering intensity from a single electron interaction with the X-rays, F is the structure factor describing the atomic arrangement within the crystal unit cell and G is the lattice factor containing the information about the periodicity of the crystal unit cells.

In detail, the interaction of electromagnetic radiation (e.g. X-rays) with charged particles (e.g. electrons) is described by Thomson scattering, which is an elastic scattering process. The electromagnetic wave forces the electron to oscillate like a Hertz dipole. In turn, the electron emits radiation of the initial wavelength. This process is described by the Thomson scattering equation:

$$\boldsymbol{I_e = I_0 \cdot \frac{e^4}{m^2c^4} \cdot \frac{1}{R^2} \cdot \left(\frac{1+cos^2 2\theta}{2}\right)} \qquad (3.10)$$

The intensity I_e of the scattered radiation depends on the initial intensity I_0, the detection distance R and the detection angle 2θ relative to the incoming beam. The term $(1+cos^2 2\theta)/2$ is denoted as the polarization factor of the unpolarized light. Furthermore, the prefactor $e^4/(m^2c^4)$, containing the constants for the elementary charge e, the electron mass m and the speed of light c, is about ~$8*10^{-26}$ cm^2 and exemplifies the inefficiency of X-ray scattering by electrons. However, it is noteworthy that the scattering is independent of the wavelength λ of the radiation.

As already mentioned, the structure factor *F* and lattice factor *G* are describing the scattering not only at a single electron but at a small crystal with the edges $N_i a_i$ $(i = 1; 2; 3)$ parallel along the a_i crystal axes. F and G are given by:

$$\boldsymbol{F = \sum_n f_n \cdot exp\left[i\frac{2\pi}{\lambda}(s-s_o)r_n\right]} \qquad (3.11)$$

$$\boldsymbol{G = \frac{sin\left[\frac{\pi}{\lambda}(s-s_o)N_1a_1\right]}{sin\left[\frac{\pi}{\lambda}(s-s_o)a_1\right]} \cdot \frac{sin\left[\frac{\pi}{\lambda}(s-s_o)N_2a_2\right]}{sin\left[\frac{\pi}{\lambda}\cdot(s-s_o)a_2\right]} \cdot \frac{sin\left[\frac{\pi}{\lambda}(s-s_o)N_3a_3\right]}{sin\left[\frac{\pi}{\lambda}(s-s_o)a_3\right]}} \qquad (3.12)$$

The scattering of parallel radiation is illustrated by Fig. 3.10 with the unit vector s_0 and s as the propagation direction of incident and scattered beam, respectively. We first discuss the structure factor, which contains the information about the atomic arrangement inside the crystal unit cell. The electronic structure of the scattering center is described by the atomic form factor f_n. The scattering center is the n^{th} atom at the position r_n within the cubic unit cell, whereas the respective unit cell is located at R_m. Thus, *F* is an important factor to determine the crystal structure by summing over all n^{th} atoms in the unit cell. For example, it contains information about the intensity of Bragg reflections and thus describes forbidden and allowed reflections.

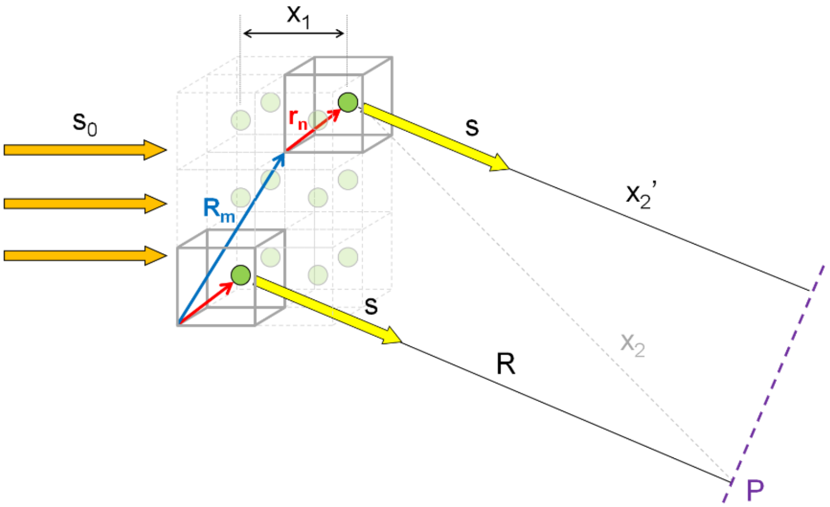

Figure 3.10: Schematic scattering of a parallel x-ray beam on a small crystal. R_m denotes the position of the m^{th} unit cell whereas r_n corresponds to the position of the n^{th} atom in a unit cell.[142]

The long range order of the crystal unit cells is described by *G*, giving thus information about the crystallite size and its defects. Since the intensity and shape of the signal is dependent on the square of *G*, the number of coherently scattering unit cells N_i has a big influence. With increasing N_i the peak intensity increases and the full width at half maximum decreases. Furthermore, the XRD signal can only be obtained close to certain geometric conditions for constructive interference, namely when all three *sin* terms in equation 3.13 are simultaneously close to their maximum. This condition is satisfied if the three Laue equations are fulfilled:

$$(\boldsymbol{s}-\boldsymbol{s_0})/\boldsymbol{\lambda}\cdot\boldsymbol{a_1}=\boldsymbol{h} \qquad (3.13a)$$

$$(\boldsymbol{s}-\boldsymbol{s_0})/\boldsymbol{\lambda}\cdot\boldsymbol{a_2}=\boldsymbol{k} \qquad (3.13b)$$

$$(\boldsymbol{s}-\boldsymbol{s_0})/\boldsymbol{\lambda}\cdot\boldsymbol{a_3}=\boldsymbol{l} \qquad (3.13c)$$

Here, h, k and l are integer numbers named the Miller indices. The quotient $(s\text{-}s_0)/\lambda$ is also called scattering vector Q and consists of the incident and scattered wave vectors $K_0 = s_0/\lambda$ and $K = s/\lambda$, respectively ($Q = K - K_0$). Due to elastic scattering and impulse/energy conservation $|K_0| = |K|$. When the scattering vector Q is equal to the reciprocal lattice vector H_{hkl} ($Q = H_{hkl}$) the Laue conditions are fulfilled and a diffraction peak can be observed, which is equivalent to the Bragg law:

$$n\lambda = 2d_{hkl}\sin\theta \tag{3.14}$$

This means if the path difference of the scattered beam at parallel net planes with the distance d_{hkl} is an integer multiple of the wavelength $n\lambda$, a Bragg peak can be observed at certain geometric conditions determined by θ, λ and d_{hkl} values.

Specular θ-2θ scans: In specular scan conditions, the angle ω of the incident X-ray beam to the sample surface is equal to θ (incident angle with respect to the net planes) shown in Fig. 3.11. By equally varying in a simultaneous way the angle of the X-ray source (θ) and the detector (2θ), the directions of the wave vectors K_0 and K are changing in such a way that the length of the scattering vector Q scans along the sample normal. If the scattering conditions for a Bragg reflection are fulfilled ($Q = H_{hkl}$), a diffraction maximum can be found. In this case, the lattice spacing of the (hkl) net planes along the growth direction can be determined by $d_{hkl} = 1/H_{hkl}$. In other words, the value of specular θ-2θ XRD scans allows determining the crystal phase and the growth orientation of a film on a substrate.

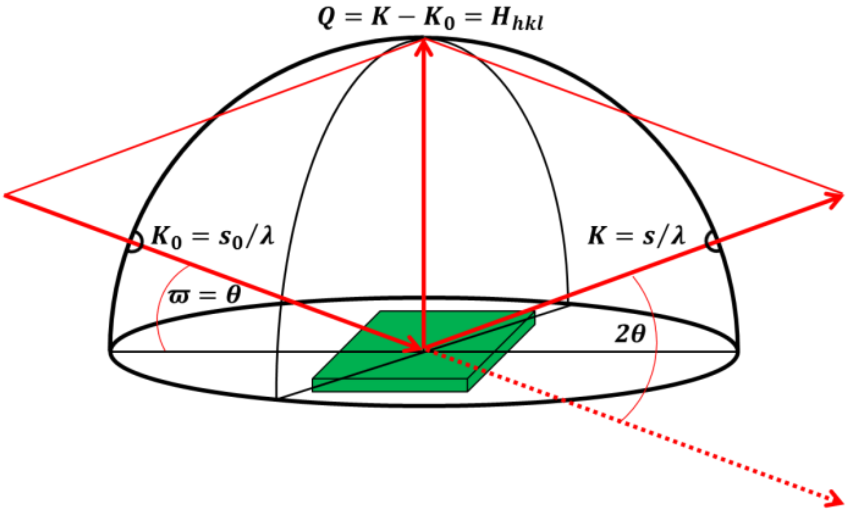

Figure 3.11: Schematic of the geometric configuration of a specular θ-2θ scan under Bragg conditions.

$cos^2\chi$ method: The $cos^2\chi_{hkl}$ method enables to determine the strain status of epitaxial thin film layers with a cubic crystal structure, as described in literature by Zaumseil.[143] The tetragonal distortion of the cubic lattice, which is determined by the poisson's ratio, causes a variation of the lattice plane distance d_{hkl} in dependence of the inclination angle χ. Here, χ_{hkl} is the angle between the sample orientation, e.g. (001), and the measured (hkl) net plane (Fig. 3.12a). As previously mentioned, by performing $\omega\text{-}2\theta$ measurements the lattice spacing d_{hkl} of the net plane (hkl) can be determined. Under the assumption that the distortion is small compared to the cubic lattice constant a, one can calculate from the measured Bragg peak position a theoretical cubic lattice constant a_{hkl} for various net planes at different tilts. Since the assumed lattice constant a_{hkl} is linearly proportional to $cos^2\chi_{hkl}$ this method allows a regression analysis (Fig. 3.12b). By a linear fit, the in-plane lattice constant a_0 can approximated at $cos^2\chi_{hkl} = 0$, which is equivalent to a 90° net plane tilt. The out-of-plane lattice constant a_1 is given at $cos^2\chi_{hkl} = 1$ corresponding to 0° tilt. Exemplary plots for strained and unstrained films are shown in Fig. 3.12b:

- When the film is fully relaxed the theoretical lattice constant is equal to the bulk value for all tilts, which means $a_0 = a_1$ (black dashed line with no slope).
- For in-plane compressive strain $a_0 < a_1$ (blue line with positive slope).
- For in-plane tensile strain $a_0 > a_1$ (red line with negative slope).

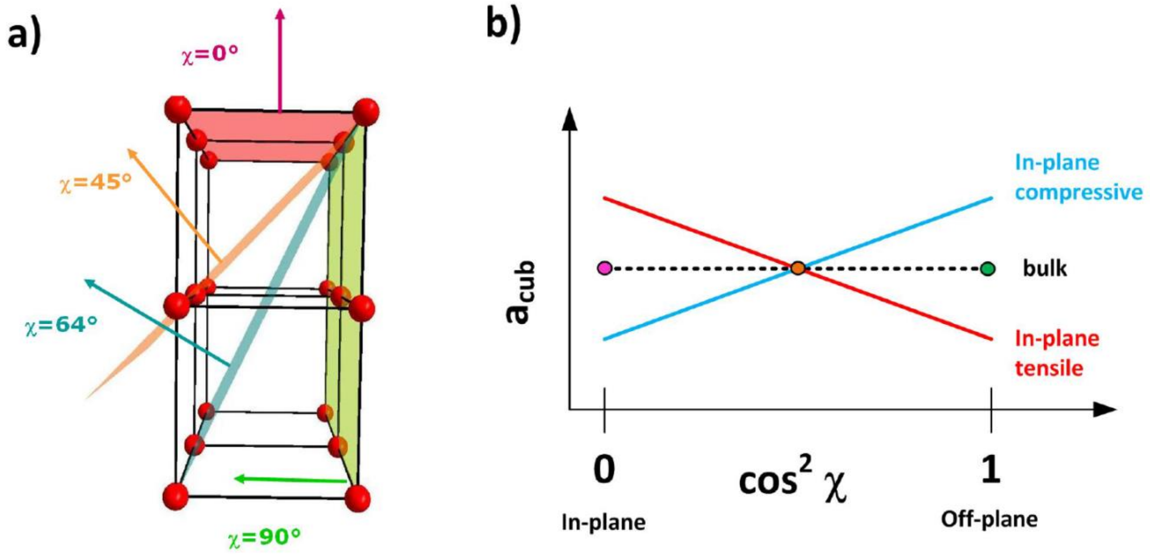

Figure 3.12: (a) Sketch of certain net planes with different inclination angles χ with respect to the (001) surface in a primitive cubic unit cell. (b) Scheme of a $cos^2\chi$ plot for the in-plane compressive, in-plane tensile and fully relaxed case.[144]

φ-scan and pole figure mapping: For a φ-scan the sample rotates around the sample normal, while the X-ray source and the detector are aligned at a fixed χ and ω-2θ configuration. So the scattering vector Q scans along the azimuth given by the scan direction S (Fig. 3.13). This technique allows finding Bragg reflections (at the corresponding χ and ω-2θ configuration) and determining the in-plane orientation of an epitaxial thin film for $\chi > 0°$. For several φ-scans at different inclination angles χ one can get a pole figure mapping corresponding to the hemisphere surface, whose radius is given by Q or rather the ω-2θ values. This technique was used to determine the in-plane symmetry and thus to discriminate between the cubic and the hexagonal phase. Furthermore, microtwins in cubic structure can also be detected in this way.

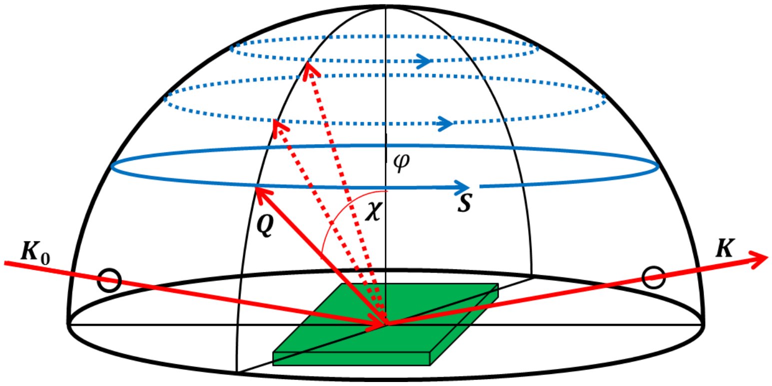

Figure 3.13: Schematic geometric conditions of scattering vector Q and the wave vectors K_0 and K for φ-scans along the scan direction S for different inclination angles χ.

GIXRD scans: In grazing incidence configuration the incoming wave vector K_0 is typically impinging with a small angle θ_i to the surface. By varying the incident angle from below to above the critical angle, the structure of a material can be probed in a non-destructive way from surface to bulk. To get also information from the bulk, the GIXRD measurements were performed in this study at $\theta_i = 0.5°$, which is above the critical angle for total reflection for the here considered oxides (CeO_2: $\theta_c = 0.27°$, Pr_2O_3: $\theta_c = 0.27°$ at $E = 10.5\ keV$). For the in-plane measurements the outgoing wave vector K was likewise detected at small angles θ_f to keep the scattering vector almost parallel to the surface (Fig. 3.14a). In contrast, for l-rod scans by GIXRD the in-plane components (Q_h, Q_k) of the scattering vector Q are kept constant and only the out-of-plane component Q_l is varied. Therefore, the angle θ_f has to increase in order to reach the out-of-pane reflections.

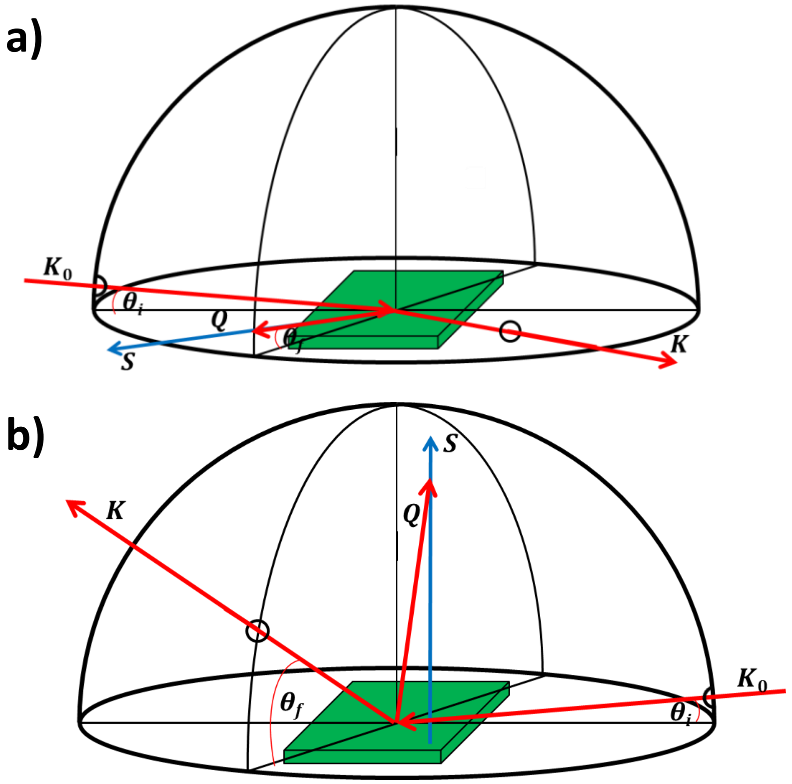

Figure 3.14: Schematic GIXRD geometric setup with an impinging beam at a small angle θ_i for (a) in-plane scans and for (b) l-rod scans.

At this point, it is useful to introduce the transformation from the cubic bulk (B) coordinate system (Cartesian) to a hexagonal like surface (S) coordinate system, which is related to the Si(111) orientation of the considered samples. Therefore, the surface coordinate axes are given by the Si lattice vectors $[10\bar{1}]$, $[110]$ and $[111]$:[128, 140]

$$\boldsymbol{a_1^S} = \frac{1}{2} \cdot \begin{bmatrix} \mathbf{1} \\ \mathbf{0} \\ \bar{\mathbf{1}} \end{bmatrix} \cdot \boldsymbol{a_{Si}^B}, \qquad \boldsymbol{a_2^S} = \frac{1}{2} \cdot \begin{bmatrix} \bar{\mathbf{1}} \\ \mathbf{1} \\ \mathbf{0} \end{bmatrix} \cdot \boldsymbol{a_{Si}^B}, \qquad \boldsymbol{a_3^S} = \frac{1}{3} \cdot \begin{bmatrix} \mathbf{1} \\ \mathbf{1} \\ \mathbf{1} \end{bmatrix} \cdot \boldsymbol{a_{Si}^B} \qquad (\mathbf{3.15})$$

Here, a_{Si}^B is the bulk Si lattice constant and a_i^S $(i = 1, 2, 3)$ corresponds to the new set of surface lattice vectors. The transformation from bulk h, k, l to surface H, K, L indices and vice versa can be carried out by these matrix operations:

$$\begin{bmatrix} \boldsymbol{h} \\ \boldsymbol{k} \\ \boldsymbol{l} \end{bmatrix}^{\boldsymbol{B}} = \frac{1}{6} \cdot \begin{bmatrix} \mathbf{4} & \bar{\mathbf{4}} & \mathbf{6} \\ \mathbf{4} & \mathbf{8} & \mathbf{6} \\ \bar{\mathbf{8}} & \bar{\mathbf{4}} & \mathbf{6} \end{bmatrix} \cdot \begin{bmatrix} \boldsymbol{H} \\ \boldsymbol{K} \\ \boldsymbol{L} \end{bmatrix}^{\boldsymbol{S}}, \qquad \begin{bmatrix} \boldsymbol{H} \\ \boldsymbol{K} \\ \boldsymbol{L} \end{bmatrix}^{\boldsymbol{S}} = \frac{1}{6} \cdot \begin{bmatrix} \mathbf{3} & \mathbf{0} & \bar{\mathbf{3}} \\ \bar{\mathbf{3}} & \mathbf{3} & \mathbf{0} \\ \mathbf{2} & \mathbf{2} & \mathbf{2} \end{bmatrix} \cdot \begin{bmatrix} \boldsymbol{h} \\ \boldsymbol{k} \\ \boldsymbol{l} \end{bmatrix}^{\boldsymbol{B}} \qquad (\mathbf{3.16})$$

Therefore, this nomenclature allows referring the surface coordinates to the more widely used Si bulk system. In Fig. 3.15 a top view of the Si(111) surface reciprocal lattice is shown corresponding to the $[00L]^S$ direction in surface coordinates. This direction is parallel to the so called l-rods, e.g. $[01L]^S$ and $[10L]^S$, which were scanned in this thesis. Furthermore, the in-plane direction $[11\bar{2}]$ or rather $[H00]^S$ direction will be of interest. For further discussions, the indices B related to the bulk are skipped for simplification.

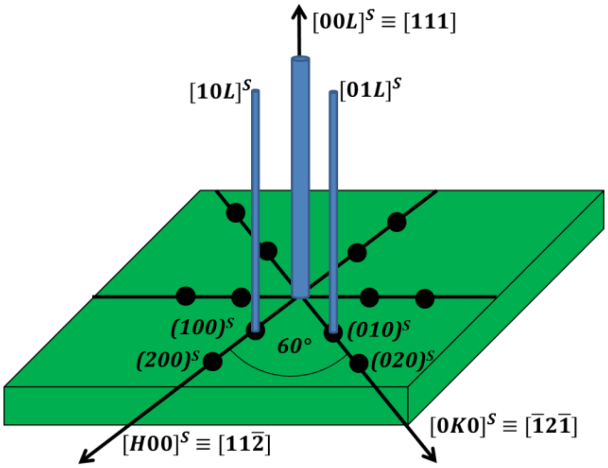

Figure 3.15: Schematic of the reciprocal Si(111) lattice space in the surface coordinate system. The *H, K, L* coordinate axes and the $[10L]^S$ and $[01L]^S$ l-rods are labeled.

3.2.2.3 X-ray reflectivity

The X-ray reflectivity technique was used to determine the thicknesses of the oxide thin films and bilayer oxide stackings. Thus, XRR includes information about the material specific electron density and the roughness of the surface and interface. The geometric configuration of this investigation method is similar to a specular θ-2θ setup within a typical scan range of $2\theta = 0° - 7°$ (Fig. 3.16a). The corresponding intensity signal can be separated in three parts:

1) The intensity is increasing by several orders of magnitude between 0° - 0.2°, because in the low angle region the X-ray beam is cut by the sample or in other words, the X-ray footprint on the sample increases.
2) An intensity plateau exists up to a value which is equal to the critical angle θ_c due to the total reflection of the primary beam. The value of θ_c is material specific, and increases with increasing electron density (Fig. 3.16b).
3) The intensity signal starts to drop (Fig. 3.16c) and oscillate (Fig. 3.16d) above θ_c. This is related to the scattering at the thin film interfaces and gives information about the thickness and roughness, due to the materials constants “seen” by the X-ray beam.

The resulting intensity signal as a function of θ can be expressed by this equation:

$$\boldsymbol{\frac{I_R}{I_0} = \left|\frac{\theta - \sqrt{\theta^2 - \theta_c^2 - 2i\beta}}{\theta + \sqrt{\theta^2 - \theta_c^2 - 2i\beta}}\right|^2} \qquad \mathbf{(3.17)}$$

I_0 and I_R are the incident and reflected intensities. The critical angle is also given by $\theta_c = \sqrt{2\delta}$ (δ includes the electron density ρ). Furthermore, $i\beta$ (β includes the attenuation coefficient μ) considers the imaginary part of the dielectric susceptibility. In other words, the reflected intensity depends on the refractive index given by $n = 1 - \delta - i\beta$. Thus, δ and β or rather the electron density ρ and attenuation coefficient μ can be estimated. For an ideally smooth surface, the drop of the intensity scales with $1/Q^4 = (4\pi\lambda/sin\theta)^4$ above θ_c. An increasing surface roughness σ leads to a faster intensity decrease, which influence the equation (3.17) by multiplication with a Debye-Waller like factor $\exp(-\sigma^2 Q^2)$.

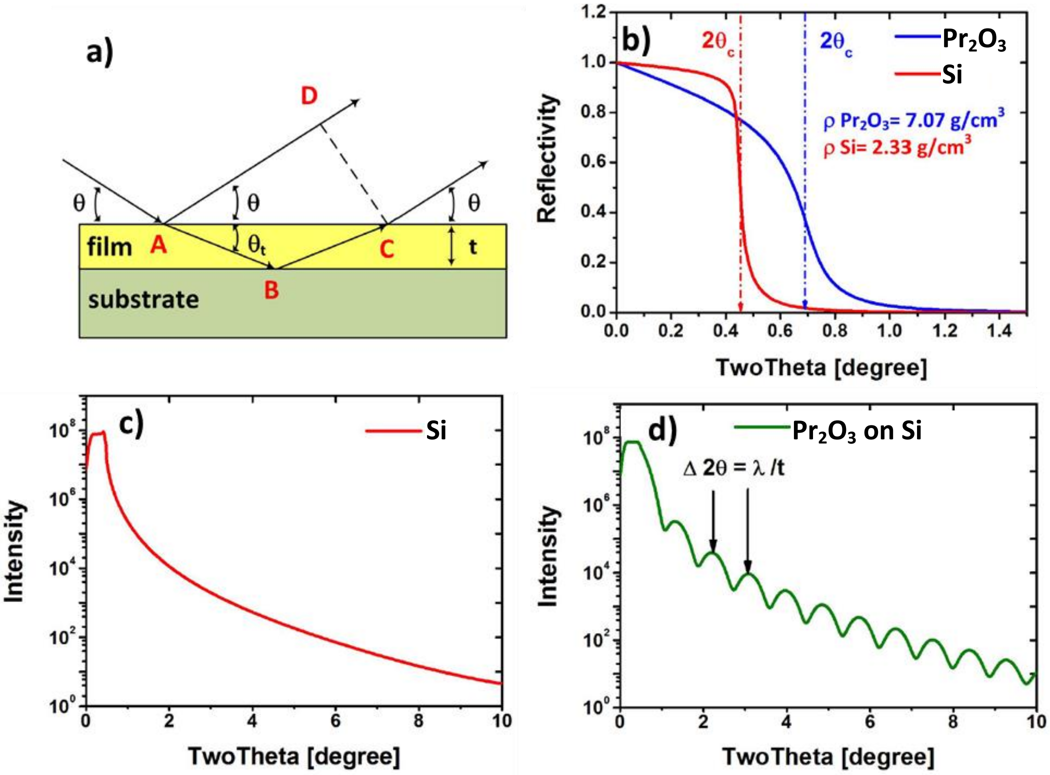

Figure 3.16: (a) Beam path for different reflected and transmitted X-rays at a thin film/substrate structure (b) Reflectivity plot and related critical angle for Si and Pr_2O_3 showing the electron density dependence (c) XRR scan of the Si substrate (d) XRR scan of an Pr_2O_3 thin film on Si demonstrating Kiessig fringes.[144]

The oscillations (also called Kiessig fringes) are reaching their maxima when the phase difference Δ between the reflected and refracted beam is an integer multiple of the wavelength expressed by $\Delta = n(AB + BC) - AD = 2t \cdot sin\theta_t$. Here, t is the layer thickness and θ_t the angle between transmitted beam and layer surface (Fig. 3.16a). Assuming Fresnel equation, one can determine the thickness from the angular distance $\Delta 2\theta = 2\theta_{m+1} - 2\theta_m$ of two neighboring maxima:

$$\boldsymbol{t \approx \frac{\lambda}{2\theta_{m+1} - 2\theta_m}} \qquad (3.18)$$

By applying fitting procedures based on the Fresnel equations and estimating the fitting parameters (layer thickness, electron density, surface and interface roughness) one can derive the thickness. In this PhD thesis, the program RCRefSim from Zaumseil was used to analyze the XRR data.[145]

3.2.3 Raman spectroscopy

3.2.3.1 Raman setup

Via Raman spectroscopy one can investigate vibrational states within a material. The Raman effect is based on the inelastic scattering of monochromatic light. Here, a He-Cd UV-laser (λ = 325 nm) was used to observe specific oxygen deficient and complex reconstruction phonon modes and shifts. After the interaction of the laser light with the matter, the inelastic scattered light is detected by an InVia Renishaw spectrometer (Fig. 3.17).

Figure 3.17: Picture of the InVia Renishaw Raman spectrometer.

3.2.3.2 Raman scattering

By the electric field of the laser light, the electric charges within the investigated medium are brought to oscillation, consequently these charges serve as emitting dipoles of diffuse light. It is noted that the incoming light energy $\hbar\omega_0$ is smaller than the difference between the electronic ground and electronic excited state and thus is absorbed by a virtual state resulting from the vibrational mode. The polarization of the charges is given by:

$$\boldsymbol{P} = \boldsymbol{\varepsilon_0 \chi E(\omega_0 t)} \tag{3.19}$$

Here, ε_0 is the vacuum permittivity and χ the susceptibility, describing the interaction of the medium with an electrical field:

$$\boldsymbol{E} = \boldsymbol{E_0} \cos(\boldsymbol{\omega_0 t}) \tag{3.20}$$

Limiting the phonon modes in the medium to the first order Raman tensor $(\partial\chi/\partial Q_k)$ (with the phonon mode amplitude *Q = 0*), the susceptibility modulated by the lattice vibration around the equilibrium position χ_0 is:

$$\chi = \chi_0 + \sum_k \left(\frac{\partial\chi}{\partial Q_k}\right)_{Q=0} Q_k \tag{3.21}$$

Considering all vibrational modes *k*:

$$Q_k = Q_{k0} \cos(\varpi_k t) \tag{3.22}$$

Regarding equation (3.19) – (3.22), the polarization is given by:

$$\begin{aligned} \boldsymbol{P} &= \chi_0 E_0(\omega_0 t) \\ &+ 1/2 \left(\frac{\partial\chi}{\partial Q_k}\right)_{Q=0} Q_{k0} E_0 \cos((\omega_0 - \omega_k)t) \\ &+ 1/2 \left(\frac{\partial\chi}{\partial Q_k}\right)_{Q=0} Q_{k0} E_0 \cos((\omega_0 + \omega_k)t) \end{aligned} \tag{3.23}$$

From this equation one can classify three cases (schematically shown in Fig. 3.18.):

1) Is the emitted light of the same wavelength as the incoming light ($E = \hbar\varpi_0$), the process is called Rayleigh scattering.
2) If the final ground state has a higher energy level than the initial ground state the inelastic scattered photon exhibits less energy $E = \hbar(\varpi_0 - \varpi_k)$ (Stokes Raman scattering).
3) Vice versa, if the final ground state has a lower energy level than the initial ground state the inelastic scattered photon exhibits more energy $E = \hbar(\varpi_0 + \varpi_k)$ (Anti-Stokes Raman scattering). Thus, the Anti-Stokes signals exhibit less intensity and are strongly dependent on the temperature, since they depend on the population in the vibrational state.

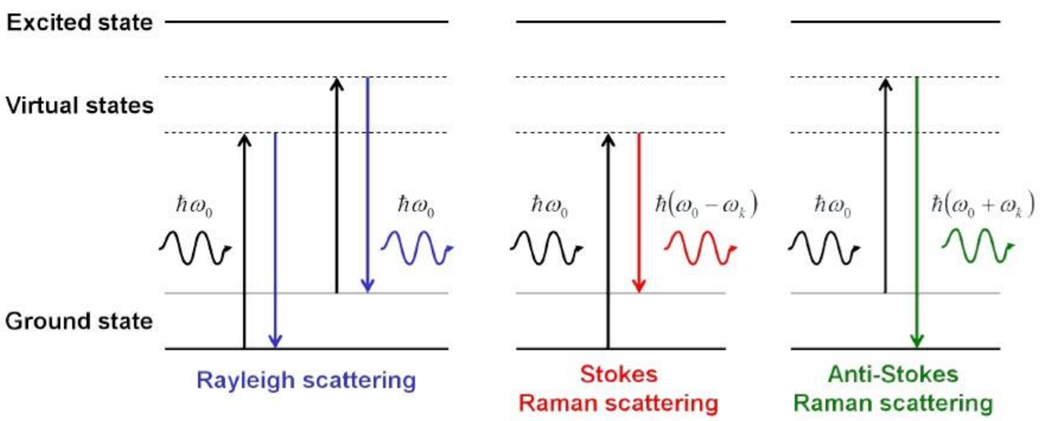

Figure 3.18: Energy level diagram from different phonon scattering processes.[142]

The both last cases related to the Raman effect are caused by inelastic scattering, which occurs when the unit electric polarization vectors *e* of the incoming light (e_i) and the scattered light (e_s) couple with the Raman tensor ($R_k = (\partial\chi/\partial Q_k)_{Q=0}$) of a vibrational mode. The proportionality of the Raman signal intensity is described by:

$$\boldsymbol{I \sim \sum_k |e_i R_k e_s|^2} \qquad (3.24)$$

Thus, Raman signals are linked to certain selection rules, determined by the phonon modes or rather by the crystal structure and orientation of the medium. Since the Brillouin zone boundaries of the considered crystals ($\pm 2\pi/a$ with a ~ 0.5 *nm*) are much bigger than the wave vector ($2\pi/\lambda$ with $\lambda = 325$ *nm*) of the incoming light, only processes near the Brillouin zone center Γ are considered. An example for the phonon dispersion curves of CeO_2, calculated by the rigid ion model, is presented in Fig. 3.19. As mentioned for equation (3.21), second order scattering will not be considered here. A nuclear site group analysis gives for the fluorite (f) and bixbyite (bb) lattice the following irreducible representations of the acoustical (ac) and optical (op) modes:[146, 147]

$$\boldsymbol{\Gamma_{op}^{f} = F_{2g} + F_{1u}, \quad \Gamma_{ac}^{f} = F_{1u}} \qquad (3.25)$$

$$\boldsymbol{\Gamma_{op}^{bb} = 4A_g + 4E_g + 14F_g + 5A_u + 5E_u + 16F_u, \quad \Gamma_{ac}^{bb} = F_u} \qquad (3.26)$$

From a group theoretical point of view, there are several vibration modes but only some of them are Raman-active ($\boldsymbol{F_{2g}, A_g, E_g, F_g}$) due to the selection rules presuming a change in the polarizability. In this PhD thesis, in particular the investigation of the F_{2g}mode of $Ce_{1-x}Pr_xO_{2-\delta}$ (x = 0-1) in a backscattering Raman geometry set-up will be of special importance. An extensive description of Raman spectroscopy is given in the literature.[148-152]

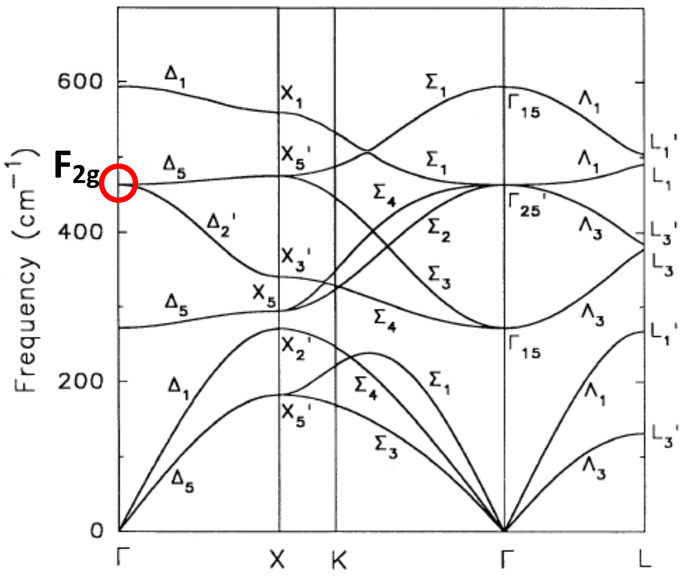

Figure 3.19: Phonon dispersion curves for CeO_2 calculated by the rigid ion model.[153]

3.2.4 Further techniques

3.2.4.1 Ab-initio calculations

Figure 3.20: JUROPA super computer in Jülich within the Neumann Institute for Computig. (NIC).

Ab-initio calculations were carried out in support for this PhD thesis by Dr. Jarek Dabrowski from IHP at the JUROPA supercomputer in Jülich within the Neumann Institute for Computing (NIC) shown in Fig. 3.20. The purpose was to determine the energetic difference of the Si(111)/hex-Pr_2O_3(0001)/CeO_2(111) interface models as explained in the chapter 4.1.3. The calculation parameters and results were published in detail in Physical Review B by Zoellner *et al.*[154] Details about the theoretical calculations are extracted from this publication by our group:

"Ab initio calculations were performed with the parallelized pseudopotential plane-wave code QUANTUM ESPRESSO.[155] Exchange and correlation energies were expressed in the local density approximation (LDA) form, as parametrized by Perdew and Zunger.[156] Oxygen, silicon, and hydrogen atoms were described with pseudopotentials from ESPRESSO distribution (ultrasoft pseudopotentials were used for oxygen). For praseodymium and cerium atoms, custom pseudopotentials were created. The n = 5 shell electrons were treated as semicore electrons.[157] In order to circumvent the LDA problem with the open f shell, the 4f shell was frozen in the core. Consequently, the lanthanide atoms Ln with valence 3 and 4 (Ln^{3+} and Ln^{4+}, where Ln = Ce, Pr) were represented by separate pseudopotentials, meaning that in the calculation they were treated as separate species: the number of f electrons was fixed and no conversion between the Ln^{3+} and Ln^{4+} "species" was possible during the self-consistent run. All four Ln pseudopotentials included the 5p shell as semicore electrons. The pseudopotentials were verified to be free of ghost states. They reproduced the lattice parameters of the corresponding bulk oxide with an accuracy better than 1%, which is typical for this kind of calculation. Also, the computed bulk moduli were in a satisfactory agreement with the experimental data.[158] For the interface calculations, the Brillouin zone was sampled with eight surface special k points equivalent to the (1/4, 1/4, 0) point of the 5 × 3 primitive rectangular surface cell with dimensions 1.945 × 2.021 nm^2, corresponding to volume-relaxed hexagonal Pr_2O_3 bulk. The energy cutoff for plane waves was set to 40 Ry."

3.2.4.2 Reflection high-energy electron diffraction

As already mentioned in chapter 3.1.1, a RHEED apparatus from Staib Instruments was used to verify the (7×7) reconstruction of the Si(111) surface as well as the crystalline properties of the heterostructure. It monitored the growth of the oxide films in-situ in order to control the quality and orientation. For this purpose, the equipment accelerates an electron beam from an electron gun with an energy E = 15.8 keV under an impinging angle $\alpha \sim 2°$ to the sample surface. The scattered electron beam creates a diffraction pattern on a fluorescent screen. This pattern is formed according to the fulfillment of the scattering condition $Q = H_{hkl} = K - K_0$ similar to XRD. This can be illustrated by the Ewald construction (Fig. 3.21).[159, 160] Here, K_0 is the direction of the incoming electron beam pointing to the origin of the reciprocal space from which the Ewald sphere is constructed by the radius $K_0 = 2\pi/\lambda$. At the intersection points of K with a reciprocal lattice vector, constructive interference appears. Due to the glancing incidence angle and the low penetration depth of the electrons, an atomically smooth surface may be regarded as a 2D mesh with crystal truncation rods (CTR) along the surface normal. Thus, as the third Laue condition is missing the reciprocal lattice degenerates to a 2D arrangement of rods perpendicular to the sample surface. Due to the high energy electrons, K_0 is much bigger than the distance of the rods. In other words, the “huge” Ewald sphere approximates a flat plane with respect to the CTRs and the Bragg condition is fulfilled for a planar cut through the reciprocal space. Thus, the fluorescent screen gives a 2D projection of the rods along the z direction and perpendicular to the surface. However, considering the dynamical scattering theory (multiple scattering) and a finite surface roughness, intensity modulations along these rods (even in form of diffraction spots) are observed. The RHEED technique and the corresponding diffraction theories are comprehensively explained in the literature.[161, 162]

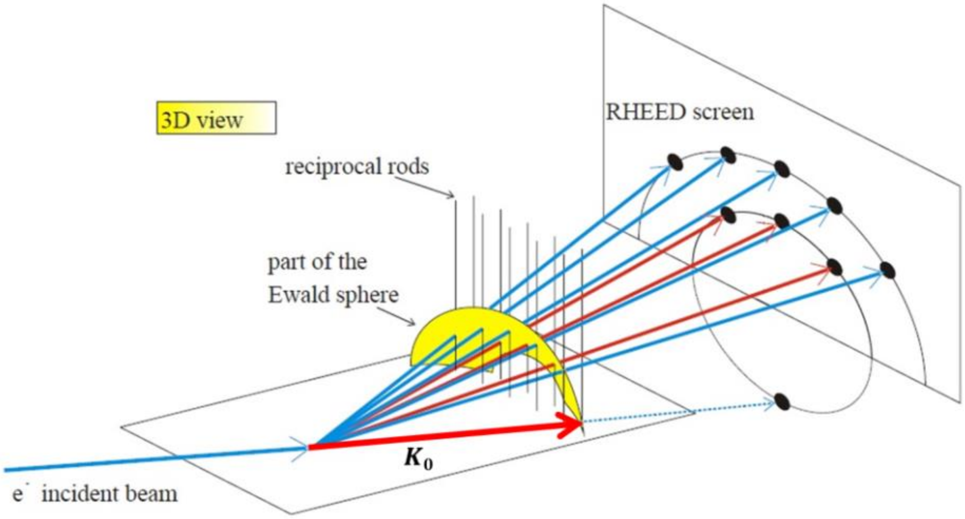

Figure 3.21: 3D Sketch of an Ewald sphere part cutting the reciprocal lattice rods and the corresponding RHEED image on the screen.[163]

3.2.4.3 Transmission electron microscopy

Transmission electron microscopy (TEM) is based on the interaction of monochromatic electrons with a specimen. Therefore, an electron beam is extracted from a heated filament and accelerated to energies of 20-300 keV. The TEM tool Phillips CM200 used at IHP (Fig. 3.22a), operates with an energy of 200 keV. By electromagnetic lenses it is possible to focus the beam (point resolution 0.27 nm) and scan over the sample surface, which is called scanning TEM (STEM). This technique was applied by Dr. Markus Andreas Schubert from IHP to Ce-Pr-Oxide bilayer structures to get information about the local crystal structure and the interface.

TEM profits from the high resolution due to the small de-Broglie wavelength of the high-energy electrons. The impinging electrons are causing several scattering processes (Fig. 3.22b), which give information about the crystal structure, the morphology and the composition. One can distinguish between inelastic and elastic scattered electrons. The former ones can be analyzed by electron energy loss spectroscopy (EELS). Furthermore, by inelastic scattering secondary and Auger electrons are created, which can be used for surface imaging or spectroscopy, respectively. Due to the high energy electrons, also X-rays are emitted enabling energy-dispersive X-ray spectroscopy (EDX) for element mapping on the nanoscale. The elastically backscattered electrons can be used for the surface imaging similar to scanning electron microscopy (SEM). For the TEM imaging the elastically scattered electrons are used. For more detailed information on TEM the reader is referred to the literature.[164]

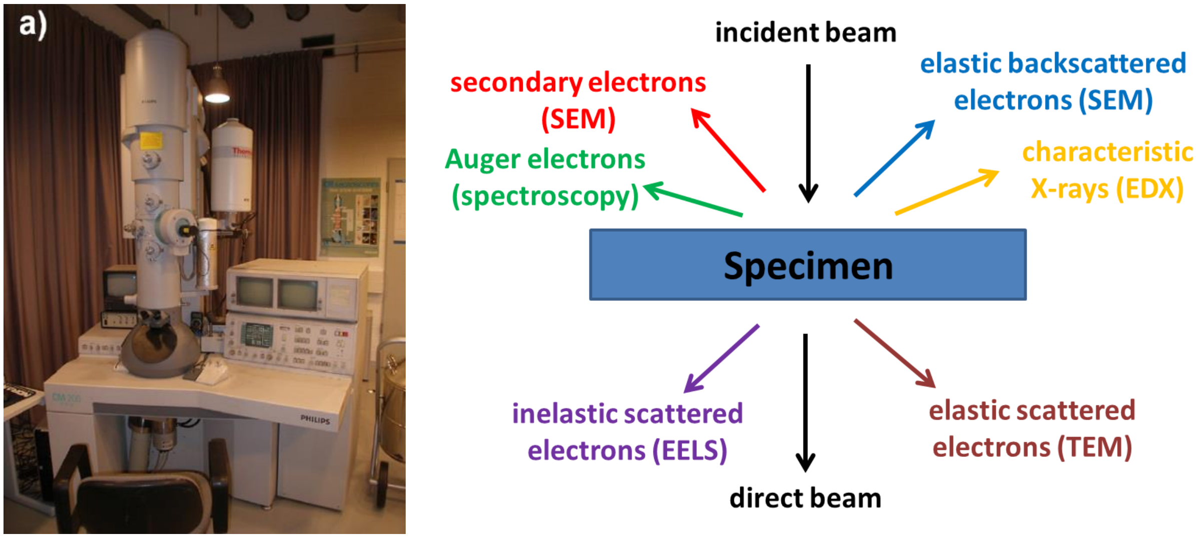

Figure 3.22: (a) Philips CM200 TEM tool at IHP and (b) scheme of the different electron scattering processes occurring for high energy electrons.

3.2.4.4 Temperature Programmed Desorption

To detect oxygen (O_2), carbon dioxide (CO_2) and water (H_2O) molecules desorbing from the sample surfaces for temperature dependent investigations of the ceria-praseodymia mixed oxide heterostructures, temperature programmed desorption (TPD) experiments were performed by PhD student Jin-Hao Jhang from the University of Bremen at the “Institut für Angewandte und Physikalische Chemie” (IAPC) within the working group of Prof. Dr. Bäumer. The base pressure in the respective UHV chamber is typically $1*10^{-10}$ mbar (Fig. 3.23a). The heating proceeded continuously and linearly (1K/s) by a tungsten filament up to 525°C for atmosphere exposed samples and up to 750°C for plasma-oxidized samples. The temperature was closely measured to the samples by a Ni/CrNi thermocouple element (type-K) and forwarded to a control unit, enabling to drive reproducible heating ramps. The desorbing molecule species were detected by a differentially pumped quadrupole mass spectrometer from *Hidden Analytical* (red arrow in Fig. 3.23b). The molecules become ionized by electrons and subsequently the ionized molecules follow a constant electromagnetic field towards the detector. Additionally, 4 opposed cylindrical electrodes, at which a superposed radio frequency field is applied, bring the ions to oscillation. Ions of a proper mass (*m*) to charge (*z*) ratio (*m/z*) in resonance with the field can reach the detector on a stabile trajectory. However, all other ions are filtered out by collision with the rods due to their instable path. More information on mass spectrometry can be found in literature.[165]

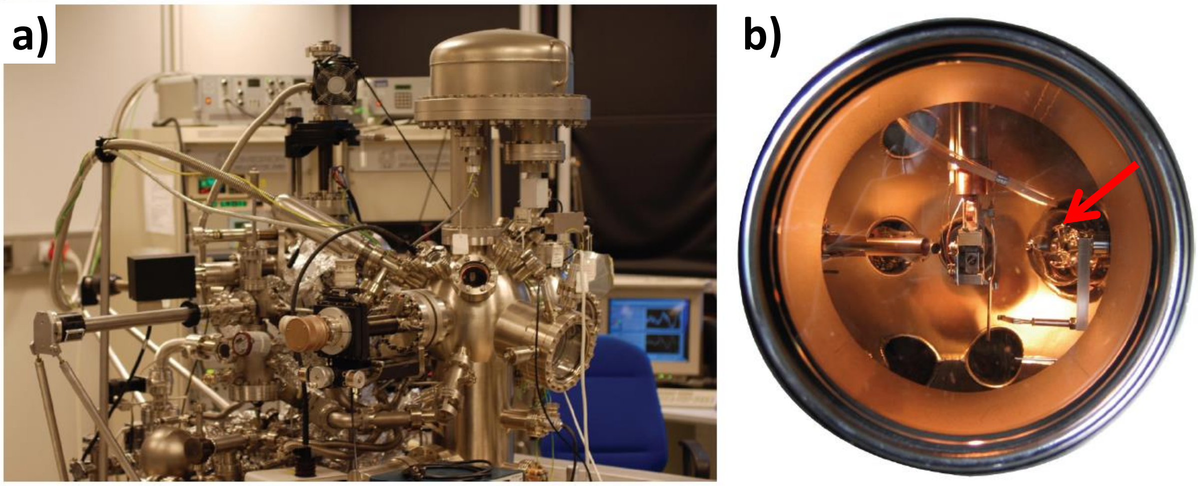

Figure 3.23: (a) UHV chamber at the IAPC from the university of Bremen within the working group of Prof. Dr. Bäumer (b) View insight the preparation chamber (quadrupole mass spectrometer is indicated by a red arrow)[8]

Chapter 4

Results & Discussion

4.1 CeO_2/Pr_2O_3 bilayer systems on Si(111)

4.1.1 Pr_2O_3 epitaxial thin films as buffer layer system for $CeO_2(111)$ growth

The epitaxial growth of CeO_2 with (111) orientation on $Si(111)$ by MBE is quite difficult, since a reaction of the evaporated CeO_2 and the Si substrate occurs as described in chapter 2.4. The formation of amorphous silicon oxide and silicates at the interface disables single crystalline $CeO_2(111)$ growth with high quality, instead a high mosaicity or even polycrystallinity with preferential (111) orientation is resulting (Fig. 4.1a). However, there are some possible opportunities for PLD deposition to avoid this interface reaction during the growth and delay the reaction after an initially crystalline CeO_2 interface layer is grown.[100, 102] However, as visible in the RHEED image (Fig. 4.1b and c) a reduction of the growth temperature (even at uncommon low deposition pressures $2x10^{-6}$ mbar) lead to an even more pronounced polycrystallinity.

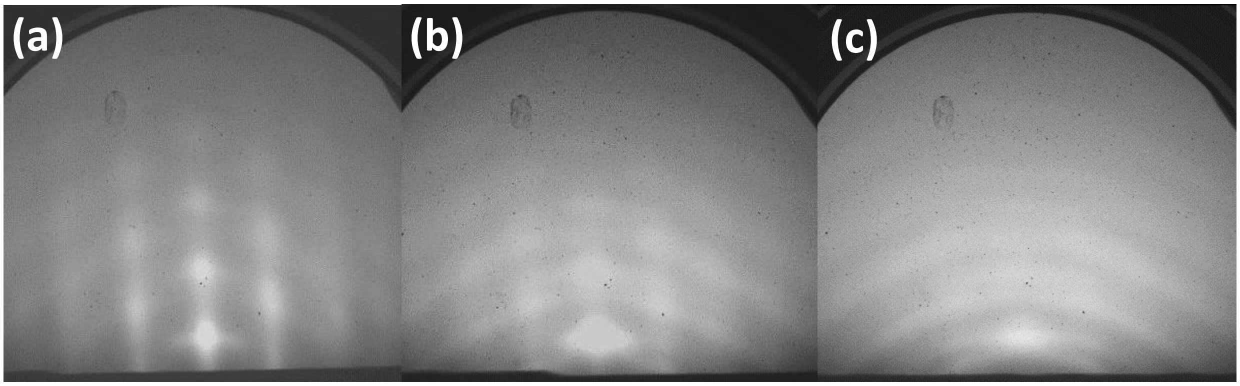

Figure 4.1: RHEED images of CeO_2 directly grown on Si(111) at (a) 625°C, (b) 525°C and (c) 425°C with a deposition pressure of $2x10^{-6}$mbar.

This is related to the too high oxygen partial pressure (typically $1x10^{-5}$ mbar) during the CeO_2 evaporation. In literature this problem was avoided by reactive MBE or by chlorine passivation of the $Si(111)$ surface.[106] These opportunities were not available at the MBE tool at IHP. Therefore, the introduction of an ultra-thin epitaxial oxide buffer layer is a proper way to protect the interface and ensure the epitaxial growth of $CeO_2(111)$ on $Si(111)$. Praseodymia was chosen as oxide buffer layer, since the growth of hex-$Pr_2O_3(0001)$ by MBE is known and exhibits one of the smallest lattice mismatches (+0.5%) among the REO to the Si(111) substrate besides CeO_2 itself (-0.35%). Furthermore, a phase transformation to cub-Pr_2O_3(111) is known.

However, the growth of (111) oriented CeO_2 on a Pr_2O_3/Si(111) support can exhibit two kinds of in-plane growth orientation, which are related to the type-A and type-B stacking configuration. Therefore, also the formation of type-A/B stacking twins may result, which means the simultaneous presence of type-A and -B domains. The type-A stacking sequence of the (111) planes from the Si substrate is defined as BACBAC… (coordinate axes in Fig. 4.2). Epitaxial cub closed packed (ccp) films grown on top of the Si(111) substrate can exhibit either the same BACBAC… stacking sequence defined as type-A configuration or can have an ABCABC… stacking sequence defined as type-B configuration (Fig. 4.2b). The cub-Pr_2O_3(111)/Si(111) heterostructure used as support for the CeO_2 growth exhibits a type-B stacking configuration known from literature.[114, 115] Since the type-B cub-Pr_2O_3(111) film contains the crystallographic information of an ABCABC… stacking, it is expected that CeO_2(111) would also grow with a type-B orientation. However, a hex-Pr_2O_3(0001) film exhibits a hexagonal closed packed (hcp) structure with an ACACAC… stacking sequence (Fig. 4.2c) using the notation introduced by Eyring *et al.*[166] Therefore, the stacking information should get lost and the formation of stacking twins is expected, as observed in the case of In_2O_3(111)/α-Al_2O_3(0001)[167] and γ-Al_2O_3(111)/α-Al_2O_3(0001)[168] and epi-Si(111)/hex-Pr_2O_3(0001)/Si(111)[25, 26].

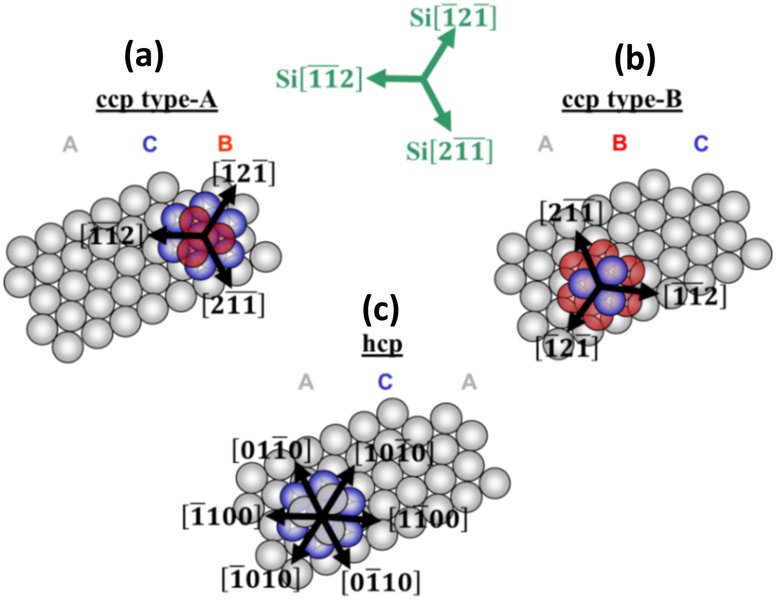

Figure 4.2: Schematic illustration in respect to the Si coordinate system of (a) the BACBAC…(type-A) stacking sequences in a ccp crystal structure; (b) the ABCABC…(type-B) stacking sequences in a ccp crystal structure; and (c) the ACACAC… stacking sequence in a hcp crystal structure.

4.1.2 Structure Characterization of epitaxial $CeO_2/Pr_2O_3/Si(111)$ bilayer systems

At first, the ***XRR*** analysis is presented in order to determine the thicknesses of the $CeO_2/Pr_2O_3/Si(111)$ bilayer heterostructures. In Fig. 4.3a and b the respective experimental XRR measurements (black curve) are shown for CeO_2/cub-$Pr_2O_3/Si(111)$ and CeO_2/hex-$Pr_2O_3/Si(111)$ up to $2\theta = 7°$. Furthermore, the simulated results (red curve) are presented with a displacement with respect to the experimental data for clarity. They were created by the program RCRefSim. Since an interface (IF) reaction occurs between the Pr_2O_3 layer and the Si(111) substrate, the model is based on a CeO_2/Pr_2O_3/IF/Si(111) layer stacking (Fig. 4.3c). It is resulting (Tab. 4.1) that the Pr_2O_3 buffer layer exhibits a thickness of 7-9 nm, and that 22 nm CeO_2 were grown on the cub-Pr_2O_3 buffer layer and that 38 nm CeO_2 were grown on the hex-Pr_2O_3 buffer layer. An interface layer up to 1 nm is observed, whereby the cub-$Pr_2O_3/Si(111)$ interface layer is thicker than the hex-$Pr_2O_3/Si(111)$ interface layer. This seems reasonable considering the additional ex-situ annealing step in 1 atm oxygen for the Pr_2O_3 phase transformation. It is also obvious that the assumed interface and surface roughness's are increasing with the thickness. For all layers a relative electron density below the normalized bulk value equal 1 is observed, which is probably related to the oxygen deficiency within the film during the growth process under UHV conditions.

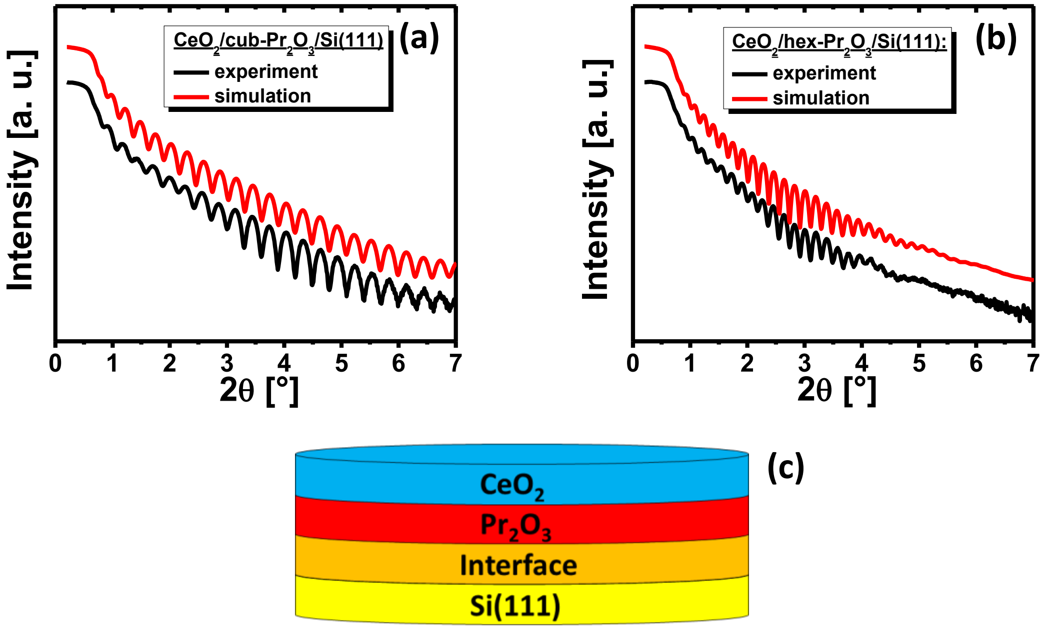

Figure 4.3: XRR measurements of (a) CeO_2/cub-$Pr_2O_3/Si(111)$; (b) CeO_2/hex-$Pr_2O_3/Si(111)$ and (c) used layer stacking model for XRR simulations.

	CeO_2/cub-Pr_2O_3/Interface/Si(111)				CeO_2/hex-Pr_2O_3/Interface/Si(111)			
	Si(111)	IF	Pr_2O_3	CeO_2	Si(111)	IF	Pr_2O_3	CeO_2
Thickness [nm]	---	0.9	7.7	22.1	---	0.2	8.8	37.9
rel. electron density	1	0.55	0.98	0.9	1	0.46	0.9	0.9
Roughness [nm]	0.20	0.29	0.40	0.46	0.06	0.41	0.47	0.82

Table 4.1: XRR simulation parameter of (a) CeO_2/cub-Pr_2O_3/Si(111) and (b) CeO_2/hex-Pr_2O_3/Si(111).

To monitor the crystal quality and growth orientation in-situ after each deposition step of the CeO_2/cub-Pr_2O_3/Si(111) and CeO_2/hex-Pr_2O_3/Si(111) heterostructure, a ***RHEED*** study was performed. Therefore, the electron beam and the fluorescent screen were aligned along the stacking sensitive Si$\langle\bar{1}10\rangle$ direction. In Fig. 4.4 the expected Bragg peak distributions are illustrated for the three potential cases of epitaxial oxide film growth, namely type-A cub(111) (blue open squares), type-B cub(111) (red open circles) and hex(0001) (green open triangles) structure and orientation. For simplicity, the sketch is performed for identical lattice constants, so that cub- and hex-Pr_2O_3 CTRs coincide. For identification, the related directions are labeled by the corresponding bulk Bragg indices.

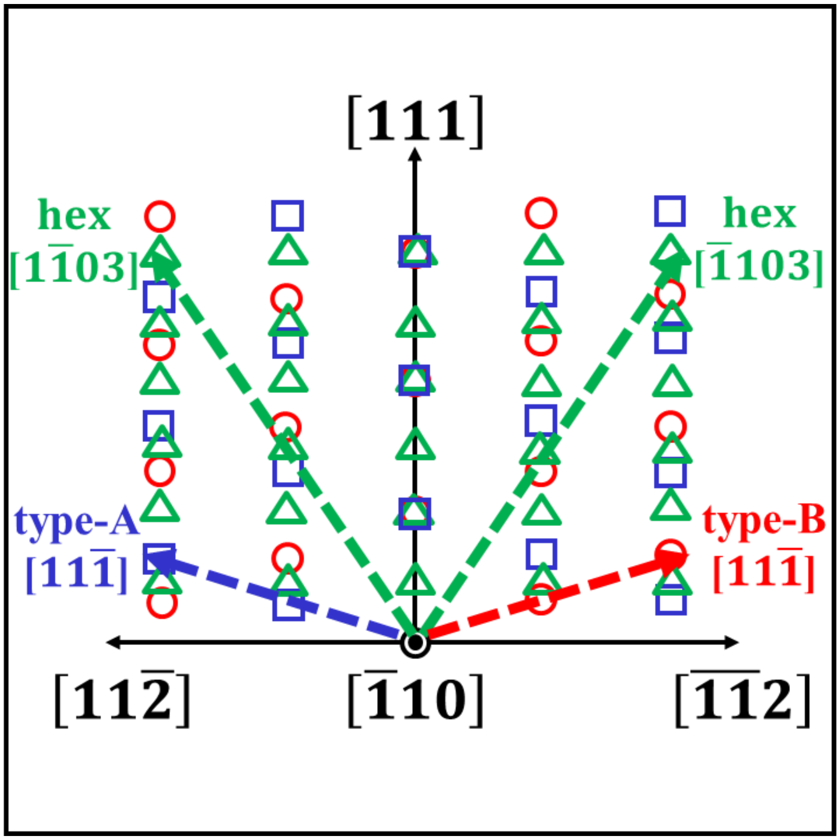

Figure 4.4: Sketch illustrating the expected Bragg reflections in reciprocal space for (111) oriented cub type-A (blue open squares), (111) oriented cub type-B (red open circles) and for a (0001) oriented hex (green open triangles) oxide films. The coordinate system is related to the bulk Si(111) substrate orientation.[154]

In all RHEED images spots appear along the crystal truncation rods (CTR), due to the onset of 3D growth. Therefore, it is possible to determine the vertical as well as horizontal oxide film orientation. Considering the theoretical Bragg peak distribution (Fig. 4.4), the dashed arrows in Fig. 4.5a and b illustrate that the samples exhibit a type-B cub-$Pr_2O_3(111)$ and hex-$Pr_2O_3(0001)$ orientation, respectively. After the deposition of CeO_2 on top of both samples, cub-$Pr_2O_3(111)$ (Fig. 4.5c) and hex-$Pr_2O_3(0001)$ (Fig. 4.5d), the same Bragg peak distribution can be observed, namely the one of a type-B oriented $CeO_2(111)$ surface. This oxide/oxide epitaxy result is expected for cub crystal structures, as reported for cub-Y_2O_3/cub-Pr_2O_3 and cub-Sc_2O_3/cub-Y_2O_3.[169, 170] Surprisingly, the CeO_2 deposition on top of hex-$Pr_2O_3(0001)$ also results in an type-B oriented $CeO_2(111)$ thin film. Concluding, the following growth orientations were found:

$CeO_2(111);\ \langle 11\bar{2}\rangle$||cub-$Pr_2O_3(111);\ \langle 11\bar{2}\rangle$||Si$(111);\ \langle \overline{11}2\rangle$

$CeO_2(111);\ \langle 11\bar{2}\rangle$||hex-$Pr_2O_3(0001);\ \langle \bar{1}100\rangle$||Si$(111);\ \langle \overline{11}2\rangle$

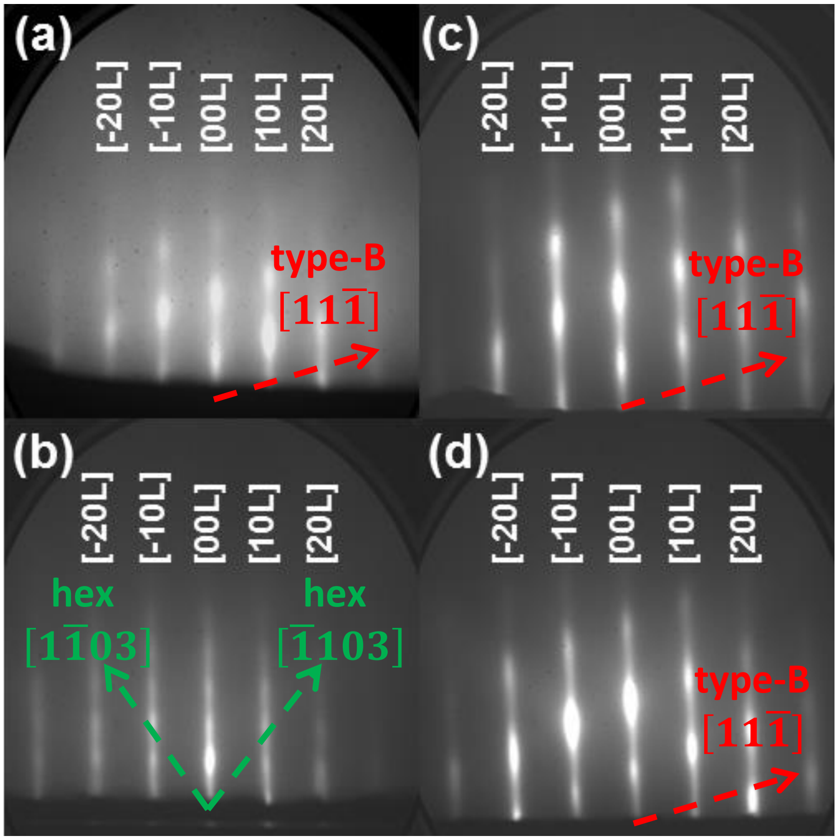

Figure 4.5: RHEED images along the Si$\langle\bar{1}10\rangle$ azimuth of (a) type-B oriented cub-$Pr_2O_3(111)$ on Si(111); (b) hex-$Pr_2O_3(0001)$ on Si(111); (c) type-B oriented $CeO_2(111)$ on type-B oriented cub-$Pr_2O_3(111)$/Si(111) support and (d) type-B oriented $CeO_2(111)$ on hex-$Pr_2O_3(0001)$/Si(111) support.[154]

Since the resolution and sensitivity of this RHEED analysis is not so precise and limited to the surface, further investigations were applied to these bilayer systems for corroboration. In the following, high-resolution ***TEM*** (HRTEM) results are discussed to gain a highly resolved insight into the crystal structure and into the layer stacking. In Fig. 4.6a and b, the respective HRTEM images of $CeO_2(111)$/cub-$Pr_2O_3(111)/Si(111)$ and $CeO_2(111)$/hex-$Pr_2O_3(0001)/Si(111)$ are shown. The interfaces are roughly indicated by arrows at the pictures´ sides. As discussed before, an interfacial layer (bright contrast in Fig. 4.6a,b) is observed, which is thicker than simulated from the XRR data. Nevertheless, it is confirmed that the cub-$Pr_2O_3(111)/Si(111)$ heterostructure exhibits a thicker interface layer than hex-$Pr_2O_3(0001)/Si(111)$, probably induced by the phase transformation annealing process. In general, it is surprising to observe an interfacial layer in the $CeO_2(111)$/hex-$Pr_2O_3(0001)/Si(111)$ heterostructure, since it was reported that hex-$Pr_2O_3(0001)$ grows without interfacial layer on $Si(111)$.[114, 171] Probably, excess oxygen during CeO_2 deposition diffuses through the hex-$Pr_2O_3(0001)$ buffer causing a post-deposition oxidation of the $Si(111)$ substrate. Furthermore, the thickness of 7-9 nm for the cub-/hex-Pr_2O_3 buffer layer is corroborated. The $CeO_2(111)$/cub-$Pr_2O_3(111)$ IF position is difficult to locate due to their similar projected potentials and crystal structures. Defects between the oxides can help to locate the interface. An edge dislocation is indicated by lines in Fig. 4.6a, which is caused by an additional $(11\bar{1})$ plane in the $CeO_2(111)$ top layer due to its smaller lattice constant. So it is found that the lattice mismatch is partially compensated by plastic relaxation and the interface can be roughly located. The lattice mismatch and relaxation process will be discussed in more detail by XRD results. The $CeO_2(111)$/hex-$Pr_2O_3(0001)$ interface is atomically sharp and was easily found due to crystal structure differences.

The coordinate system defines the crystal orientation of the $Si(111)$ substrate. The BACBAC… stacking sequence in $[111]$ direction (type-A configuration) is illustrated by an arrow pointing to the $[11\bar{1}]$ direction. The $(11\bar{1})$ planes were identified by the 70.5° tilt with respect to the (111) surface orientation. Since the $[11\bar{1}]$ direction is rotated by 180° around the $[111]$ direction in the cub-$Pr_2O_3(111)$ buffer layer as well as in the $CeO_2(111)$ top layer, these are type-B oriented as expected (Fig. 4.6a). On top of the hex-$Pr_2O_3(0001)$ buffer layer the $(11\bar{1})$ planes of the $CeO_2(111)$ top layer also show a type-B orientation with an ABCABC…stacking sequence, corroborating the surprising result from the RHEED study.

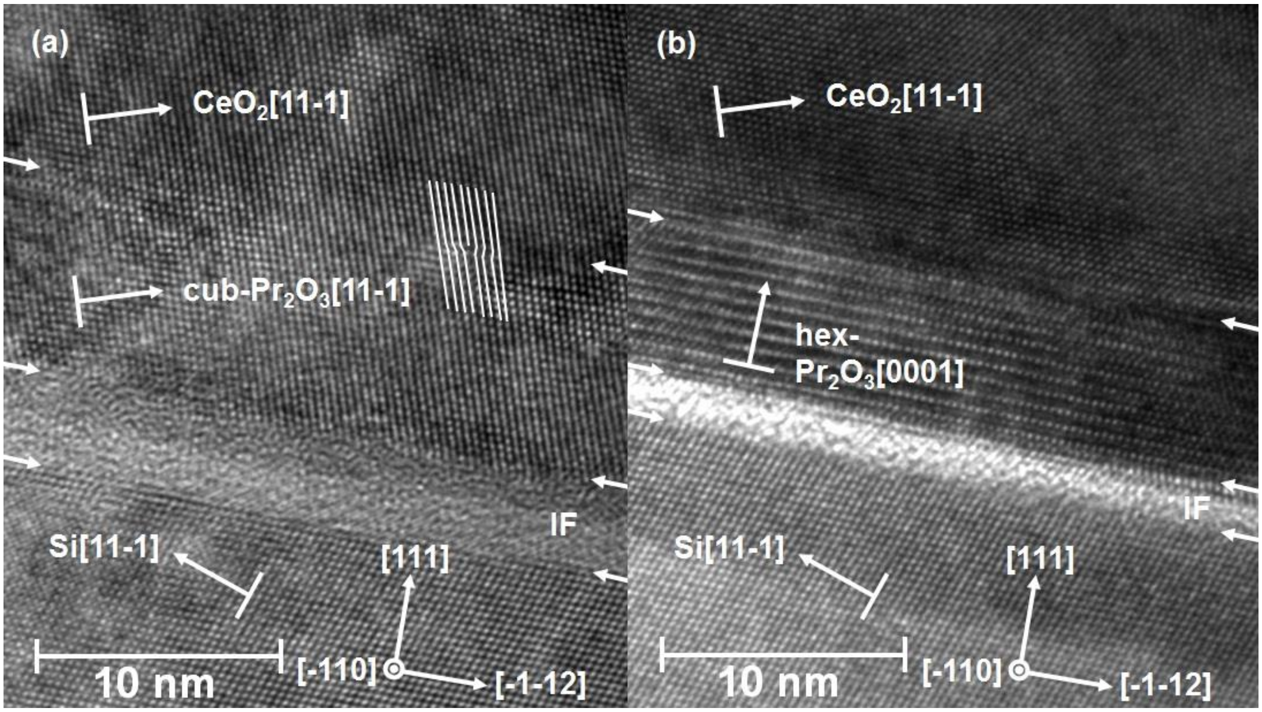

Figure 4.6: HRTEM cross-section images along the Si$[\bar{1}10]$ direction of (a) $CeO_2(111)$/cub-$Pr_2O_3(111)$/Si(111) and (b) $CeO_2(111)$/hex-$Pr_2O_3(0001)$/Si(111).[154]

However, the cross-section HRTEM results give only very local but no global information. Therefore, an extensive laboratory and synchrotron based ***XRD*** study was applied. In Fig. 4.7a wide angular **specular θ-2θ scans** are presented for the CeO_2/cub-Pr_2O_3/Si(111) and CeO_2/hex-Pr_2O_3/Si(111) sample, which corresponds to a measurement along the $[00L]^S$ rod in surface coordinates. One can find the off-plane Bragg reflections and thus determine the vertical epitaxial relationship. Within the range from 20° up to 105° the sharp and most intense Si(111) reflection and its higher orders (222) and (333) can be clearly identified. The double peak is resulting from the Cu $K_{\alpha 1}$ and Cu $K_{\alpha 2}$ radiation. The upper curve (red) shows the result from the CeO_2/cub-Pr_2O_3/Si(111) measurement. By the cub-$Pr_2O_3(nnn)$ (*n = 2-6*) reflections and the $CeO_2(nnn)$ (*n = 1-3*) reflections a (111) out-of-plane orientation can be determined for both layers. The CeO_2/hex-Pr_2O_3/Si(111) sample (lower black curve) exhibits as well a $CeO_2(111)$ top layer. However, the hex-Pr_2O_3 buffer layer is (0001) oriented, indicated by the $(000n)$ reflections with *n = 2-6*.

An enlargement of the angular range from 52.5° to 67.5° around the Si(222) enables to locate the Bragg reflections of the oxides more precisely, since the Si(222) is kinematically forbidden and exhibits the lowest intensity (Fig. 4.7b). On the hex-Pr_2O_3 support, the CeO_2(222) reflection (Fig. 4.7b lower black curve) is at $\theta = 59.24°$ (lattice spacing $d_{(222)} = 1.558$ Å), which is close to the theoretical bulk value (θ = 59.09°; $d_{(222)} = 1.562$ Å). Thus, due to the small in-plane lattice mismatch of the hex-Pr_2O_3 buffer layer with respect to the Si substrate (+0.5%) and to the CeO_2 layer (+0.8%), the CeO_2(111) film could grow almost fully relaxed on hex-Pr_2O_3(0001). In contrast, the in-plane lattice mismatch of cub-Pr_2O_3 to the Si substrate (+2.7%) and the CeO_2 film (+3.0%) is much bigger. Therefore, lateral in-plane tensile strain causes off-plane lattice compression. Thus, a shift to higher angles (θ = 59.84°; $d_{(222)} = 1.544$ Å) of the CeO_2(111) layer on the cub-Pr_2O_3(111) can be observed (Fig. 4.7b upper red curve).

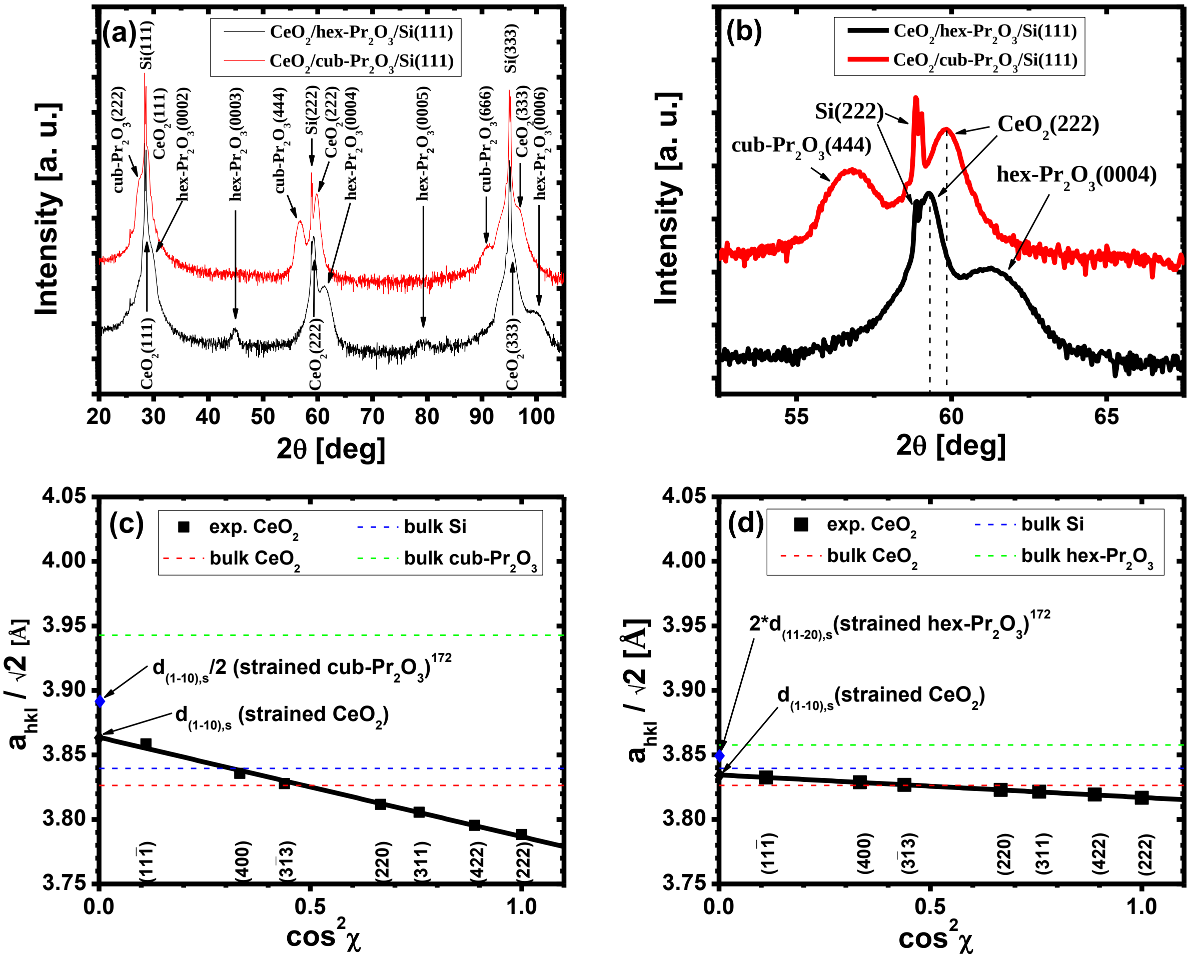

Figure 4.7: XRD specular θ-2θ measurements of CeO_2(111)/cub-Pr_2O_3(111)/Si(111) (upper red curve) and CeO_2(111)/hex-Pr_2O_3(0001)/Si(111) (lower black curve) (a) within the range from 20° to 105° and (b) within the range from 52.5° to 67.5°. Strain analysis using the $\cos^2\chi$ method of CeO_2(111) on (c) cub-Pr_2O_3(111)/Si(111) and (d) hex-Pr_2O_3(0001)/Si(111).[154]

A more detailed strain analysis including in-plane measurements can be achieved by applying the ***cos*²χ method** (introduced in chapter 3.2.2.2). Similar plots are shown with $a_{hkl}/\sqrt{2}$ to compare directly from the plots the in-plane lattice spacing for the $CeO_2(111)$ film ($d_{(1\bar{1}0),b}$= *3.826* $\AA$) on cub-Pr_2O_3/Si(111) and hex-Pr_2O_3/Si(111) (Fig. 4.7c,d). To determine the tetragonal distortion, the respective Bragg reflections were measured under certain angles χ by θ-2θ scans ($\chi_{(11\bar{1})}$ = *70.5°*,$\chi_{(400)}$= *54.7°*, $\chi_{(3\bar{1}3)}$= *48.5°*, $\chi_{(220)}$= *35.3°*, $\chi_{(311)}$= *29.5°*, $\chi_{(422)}$= *19.5°* and $\chi_{(222)}$= *0°*). By linear regression, a slightly strained in-plane lattice spacing $d_{(1\bar{1}0),s}$= *3.834* $\AA$ is resulting for the $CeO_2(111)$ film on a hex-$Pr_2O_3(0001)$/Si(111) support (Fig. 4.7d). Thus, the in-plane strain $\varepsilon_{||}$ amounts to +0.21%. The $CeO_2(111)$ film on cub-Pr_2O_3/Si(111) exhibits a much more strained in-plane spacing $d_{(1\bar{1}0),s}$= *3.834* $\AA$ (Fig. 4.7c), namely +0.78%. However, this strain value is larger than the mismatch to the Si(111) substrate. This becomes reasonable considering the Pr_2O_3 buffer layer and its strain status on Si(111). Typical results of the in-plane lattice spacings in a thickness range from 4-13 nm are $d_{(11\bar{2}0),s}$= *3.849* $\AA$ for hex-$Pr_2O_3(0001)$ and $d_{(1\bar{1}0),s}/2$= *3.890* $\AA$ for cub-$Pr_2O_3(111)$ (indicated at $cos^2\chi$ = *0°* in Fig. 4.7c and d).[172] From these values, an in-plane lattice mismatch of the hex-$Pr_2O_3(111)$ (+0.6%) and cub-$Pr_2O_3(111)$ (+1.67%) compared to the $CeO_2(111)$ top layer results. Thus, the $CeO_2(111)$ carries a partial strain due to mismatch to the cub-$Pr_2O_3(111)$ buffer and the residual lattice mismatch relaxed by plastic relaxation, as shown by an edge dislocation highlighted in the TEM image (Fig. 4.6a).

For the stacking twin analysis, ***φ-scans*** around the Si$[111]$ axis are presented in Fig. 4.8a and b. Here, in-plane information are collected from the film as well as from the substrate, given by the $CeO_2\{11\bar{1}\}$ and Si$\{11\bar{1}\}$ Bragg peaks. For these reflections, a scan around the azimuth at $\chi \approx 70.5°$ with $2\theta \approx 28.5°$ is necessary for the CeO_2/cub-Pr_2O_3/Si(111) (Fig. 4.8a) and the CeO_2/hex-Pr_2O_3/Si(111) (Fig. 4.8b) sample. Deviations from these values may result from strain and misorientation. The sharp $\{11\bar{1}\}$ Bragg peaks can be assigned to the Si substrate due to its high crystalline quality. These three peaks are resulting from the three fold symmetry of the F*d*-3*m* space group around the Si(111) surface normal. Therefore, they are separated by a 120° rotation around φ or rather the Si$[111]$ axis. Furthermore, three broader peaks are observed diffracted from the $CeO_2\{11\bar{1}\}$ net planes. These are rotated by 180° around φ with respect to the Si$\{11\bar{1}\}$ peaks and thus defined as type-B oriented, which is now corroborated for the $CeO_2(111)$ film on both (cub-Pr_2O_3/Si(111) and hex-Pr_2O_3/Si(111)) supports.

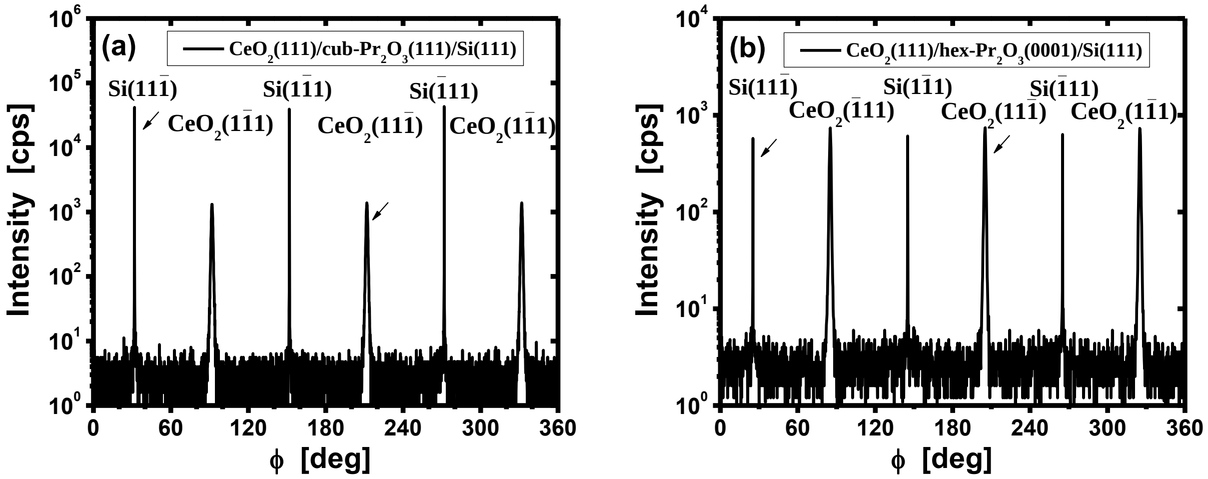

Figure 4.8: Stacking orientation analyzis using φ scan around the Si[111] axis at $\chi \approx 70.5°$ and $2\theta \approx 28.5°$ of (a) $CeO_2(111)$/hex-$Pr_2O_3(0001)$/Si(111) and (b) $CeO_2(111)$/cub-$Pr_2O_3(111)$/Si(111).[154]

However, the Si$\{11\bar{1}\}$ may cover additional type-A oriented $CeO_2(111)$ domains, which are called stacking twins. To verify the absence of these stacking twins, the Si$(11\bar{1})$ and the 180° rotated $CeO_2(11\bar{1})$ Bragg reflection (labeled by arrows in Fig. 4.8a and b) were measured by θ-2θ scans, presented in Fig. 4.9a and b. A sharp Si$(11\bar{1})$ (black curve) and a broad $CeO_2(11\bar{1})$ (red curve) peak can be observed. To estimate the stacking twin concentration, a criterion related to the $CeO_2(11\bar{1})$ maximum intensity (I_{max}) is labeled in the graphs. From this, one can conclude that less than 10% ($I_{10\%}$ criterion) of the $CeO_2(111)$ film exhibits domains of type-A orientation neither within the $CeO_2(111)$/cub-$Pr_2O_3(111)$/Si(111) nor within the $CeO_2(111)$/hex-$Pr_2O_3(0001)$/Si(111) sample.

Since this type-B stacking behavior of $CeO_2(111)$ on a hex-$Pr_2O_3(0001)$/Si(111) support is surprising, a more precise analysis of the stacking characteristic is presented in the following by high-sensitivity and high-resolution synchrotron radiation **GIXRD measurements**. In Fig. 4.9c and d the scans along the $[10L]^S$ rod and $[01L]^S$ rod are shown. The value L is related to the relative lattice unit of the Si(111) bulk coordinates (r.l.u.[Si(111)]). The respective Bragg peaks are designated by (hkl) bulk coordinates. At first, the $[10L]^S$ rod scan shows sharp signals at $L = 1/3$ r.lu. and $L = 4/3$ r.l.u., which can be attributed to the Si$(11\bar{1})$ and Si(220) peak, respectively. The $(10\bar{1}n)$ Bragg peaks of the hex-Pr_2O_3 buffer layer appear at the positions $L = 0.517n$ *r.l.u.* ($n = 1, 2, 3…$). The (002) and (113) reflections of the $CeO_2(111)$ layer are located at $L = 0.670$ r.lu. and $L = 1.675$ r.l.u., respectively. These values are close to the $L = 2/3$ r.l.u. and

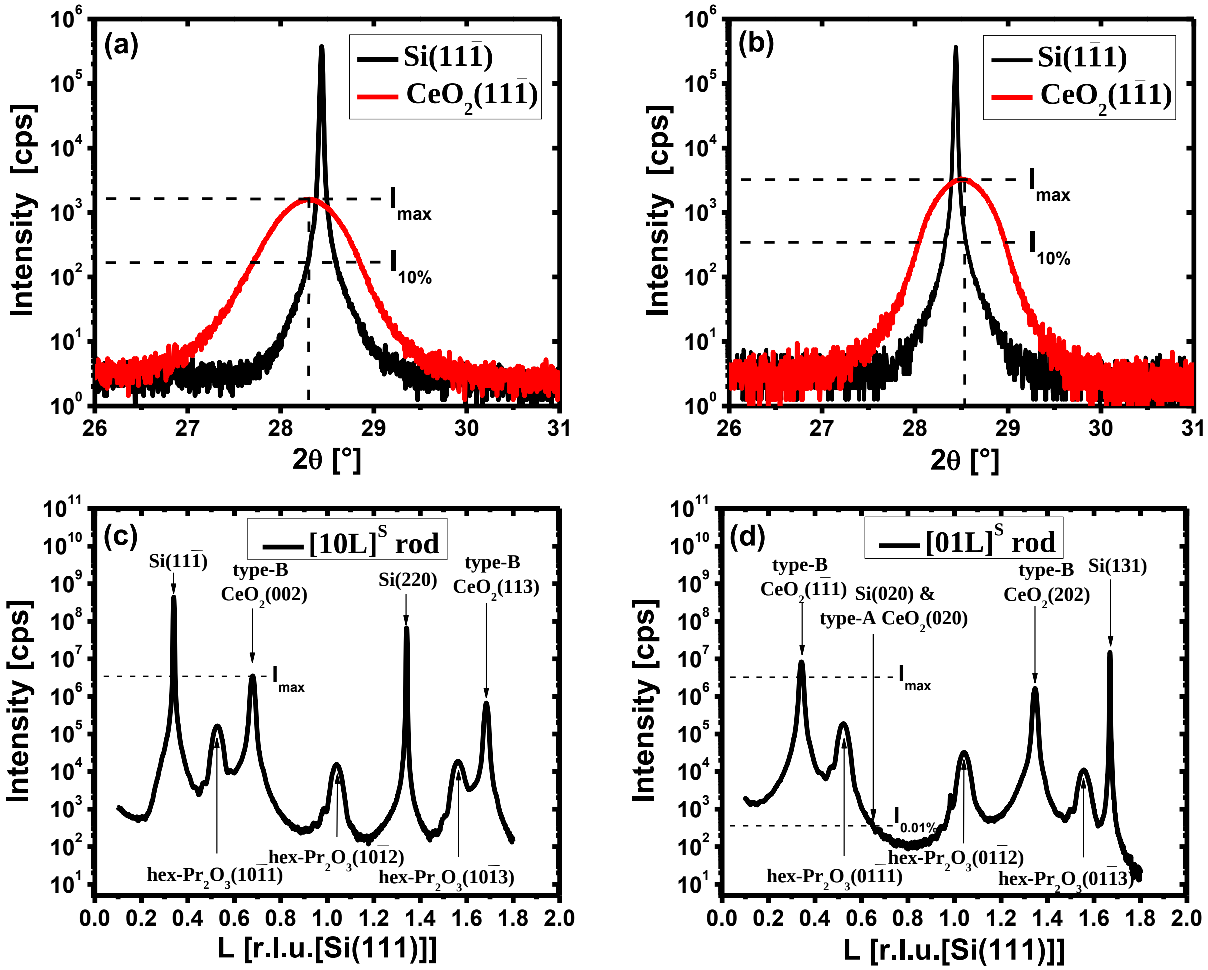

Figure 4.9: Stacking twin analyzis by HRXRD θ-2θ measurements of the Si(11$\bar{1}$) (sharp black peak) and CeO_2(11$\bar{1}$) (broad red peak with φ rotated by 180°) reflection of (a) CeO_2(111)/cub-Pr_2O_3(111)/Si(111) and (b) CeO_2(111)/hex-Pr_2O_3(0001)/Si(111). SR-GIXRD scan of CeO_2(111)/hex-Pr_2O_3(0001)/Si(111) along the (c) $[10L]^S$ rod and (d) $[01L]^S$ rod.[154]

L = 5/3 r.l.u. positions, because CeO_2 has a similar lattice constant as Si. However, potential type-A domains still cannot be detected, since their signal would overlap with the much more intense signal from the type-A oriented Si substrate. To finally estimate the type-A/B stacking ratio the $[01L]^S$ rod scan has to be analyzed, shown in Fig. 4.9d. Here, only one substrate related peak appears, namely the Si(131) at *L = 5/3* r.l.u. It is observed that the $(01\bar{1}n)$ Bragg peaks of the hex-Pr_2O_3 buffer layer also appear at the positions *L = 0.517n r.l.u.* (*n = 1, 2, 3…*) due to the six fold symmetry of these reflections. As expected, the peaks located at *L = 0.335* and *1.340* r.l.u. belong to the type-B oriented $CeO_2(1\bar{1}1)$ and $CeO_2(202)$ net planes, respectively. Since the Si(020) peak is kinematically forbidden, this gives the opportunity to detect the potential type-A oriented $CeO_2(020)$ reflection at around *L = 2/3* r.l.u. Referring to the I_{max} of the type-B $CeO_2(002)$ reflection and limited by the background intensity at *L = 2/3* r.l.u. it is estimated that less than 0.01% (see $I_{0.01\%}$ criterion in Fig. 4.9d) of type-A orientated domains are present within the type-B oriented $CeO_2(111)$ film. Concluding, no type-A oriented stacking twins concentration exist in the $CeO_2(111)$/hex-$Pr_2O_3(0001)$/$Si(111)$ heterostructure within the detection limit of this detailed laboratory and synchrotron based XRD study.

4.1.3 Microscopic origin of type-B oriented $CeO_2(111)$ growth on hex-$Pr_2O_3(0001)$/Si(111)

As the result of a twin free, exclusively type-B oriented growth from $CeO_2(111)$ on a hex-$Pr_2O_3(0001)$/$Si(111)$ support is quite surprising and not self-explanatory, the microscopic origin for this stacking characteristic was elucidated by *ab initio* calculations. In Fig. 4.10, two kind of stacking configuration models, namely type-B (Fig. 4.10a) and type-A (Fig. 4.10b), are presented. The interface between the $Si(111)$ substrate and the hex-$Pr_2O_3(0001)$ buffer layer was taken into consideration using the interface model measured and calculated by Jeutter.[113] This includes an additional oxygen layer on top of the Si atoms (red) and Pr^{3+} ions (light blue) above the T4 site (chapter 2.4). Thus, the bonding-type mismatch between Pr_2O_3 and Si is compensated by binding all electrons donated from Pr^{3+} to O^{2-} ions (yellow). A similar compensation appears at the CeO_2 and hex-Pr_2O_3 interface. By donating one more *f* electron, the interfacial Pr^{3+} ions become Pr^{4+} ions (dark blue) and form PrO_2. Thus, at the CeO_2/Pr_2O_3 interface the preferred valence state of Ce^{4+} is kept and a Pr^{3+}/Pr^{4+} valence state change occurs, conserving the REO_2 related cubic fluorite structure and semiconducting character.

The transition of the atomic planes for the type-B oriented $CeO_2(111)$/hex-$Pr_2O_3(0001)$ interface is presented in Fig. 4.10a. Referring to the notation of Eyring and Baenziger, the stacking sequence of the praseodymium sublattice is defined as ACACAC… and the oxygen sublattice as bacbac…[166] The type-B oriented CeO_2 film, exhibiting an oxygen sublattice with a likewise bacbac… stacking sequence, is a topological continuation of the hex-Pr_2O_3 arrangement. Here, just a slight shift of interfacial oxygen towards the formed Pr^{4+} occurs. Local thickness variation on a monatomic scale is energetically similar to the here presented A-terminated hex-$Pr_2O_3(0001)$ model. Thus, in case of a C-terminated interface the layer A with Pr^{4+} ions would be simply substituted by Ce^{4+} ions.

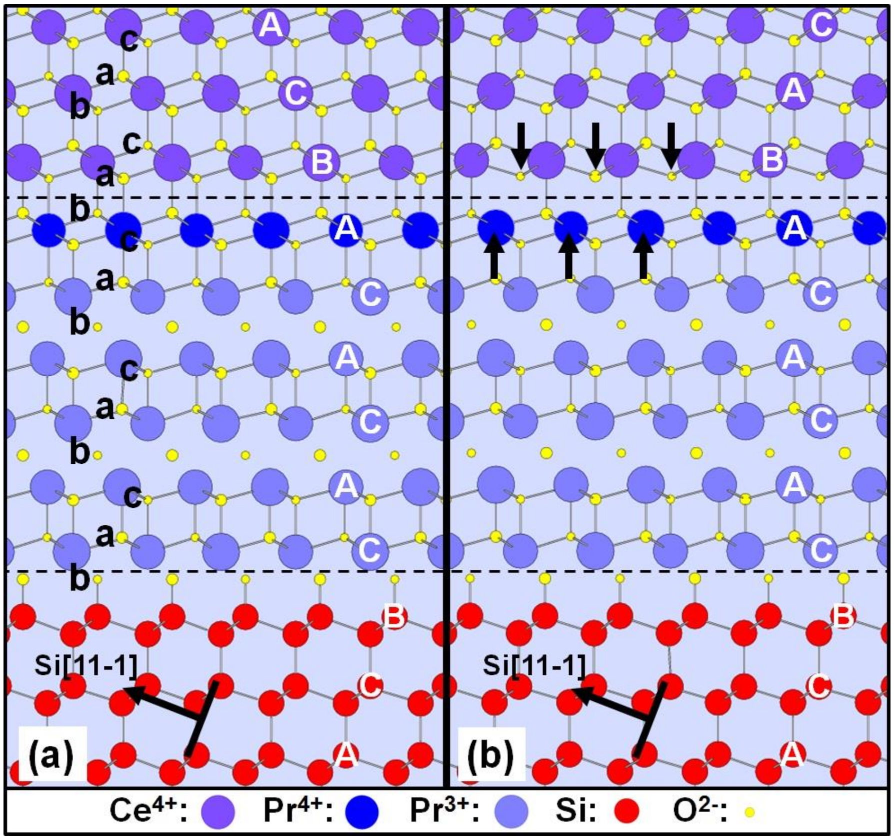

Figure 4.10: Stacking configuration models along the Si[$\bar{1}10$] of (a) type-B $CeO_2(111)$/hex-$Pr_2O_3(0001)$/Si(111) and (b) type-A $CeO_2(111)$/hex-$Pr_2O_3(0001)$/Si(111).[154]

In contrast, a type-A oriented $CeO_2(111)$ film, exhibiting an oxygen sublattice with an abcabc… stacking sequence, leads to a topological (111) stacking fault. As indicated by arrows in Fig. 4.10b, this causes under coordinated Pr^{4+} ions at the CeO_2/Pr_2O_3 interface. This results in an energetically favored type-B growth orientation by 2.2 eV per surface unit cell or rather 8 eV/nm^2. Concluding, the atomistic reason for the energetically strong preference of the exclusively, type-B oriented growth of $CeO_2(111)$ on a hex-$Pr_2O_3(0001)$/Si(111) support is based on crystallographic and electronic factors.

4.1.4 Conclusion

In the foregoing chapter, the growth of epitaxial $CeO_2(111)$ on Si(111) by MBE was discussed. The necessity of a buffer layer introduced in between CeO_2 and Si is based on interface reaction and thus formation of silicon oxide and silicate species. Even a lowering of the growth temperature and an increase of the deposition rate was not successful by means of polycrystalline CeO_2 growth. To solve this problem, it was investigated to use a cub-$Pr_2O_3(111)$

or hex-$Pr_2O_3(0001)$ buffer layer on the $Si(111)$ substrate. However, for the cub-$Pr_2O_3(111)$ formation an ex-situ annealing step is needed and the use of hex-$Pr_2O_3(0001)$ could lead to the formation of stacking twins.

The structure characterization starts with an XRR analysis, determining the thickness by modeling the thickness, the roughness and the electron density parameters of the layer stackings CeO_2(22.1nm)/cub-Pr_2O_3(7.7nm)/IF(0.9nm)/$Si(111)$ and CeO_2(37.9nm)/hex-Pr_2O_3(8.8nm)/IF(0.2nm)/$Si(111)$. During the growth process the crystallinity was investigated in-situ by RHEED giving first indications of the in-plane as well as off-plane growth orientation:

$CeO_2(111)$; $\langle 11\bar{2}\rangle$||cub-$Pr_2O_3(111)$; $\langle 11\bar{2}\rangle$||$Si(111)$; $\langle \overline{11}2\rangle$

$CeO_2(111)$; $\langle 11\bar{2}\rangle$||hex-$Pr_2O_3(0001)$; $\langle \bar{1}100\rangle$||$Si(111)$; $\langle \overline{11}2\rangle$

These crystallographic orientations were consecutively corroborated with high resolution and high sensitivity on a local and global scale by various investigation methods (TEM and XRD). Furthermore, induced strain in the $CeO_2(111)$ top layer was determined by the XRD $\cos^2\chi$ method. The strain amounts to +0.78% on the cub-$Pr_2O_3(111)$/$Si(111)$ and to +0.21% on the hex-$Pr_2O_3(0001)$/$Si(111)$ support. In detail, HRTEM confirmed the epitaxial relationships by atomic resolution. Globally, the off-plane and in-plane orientation were clarified by θ-2θ and φ scans, respectively. The stacking twin concentration of $CeO_2(111)$/cub-$Pr_2O_3(111)$/$Si(111)$ was estimated to be less than 10% just by laboratory HRXRD. However, it is expected that the type-A/B stacking ratio of the $CeO_2(111)$ film on cub-$Pr_2O_3(111)$ is not higher than on the hex-$Pr_2O_3(0001)$ buffer layer since no stacking sequence transition from ABABAB… to ABCABC… occurs. Only by synchrotron based investigations of the $[10L]^S$ and $[01L]^S$ rod, the type-A stacking twin concentration of $CeO_2(111)$/hex-$Pr_2O_3(0001)$/$Si(111)$ was determined to be less than 0.01%. Finally, this surprising result was verified by theoretical *ab initio* calculations. The twin-free, exclusively type-B oriented $CeO_2(111)$ growth on hex-$Pr_2O_3(0001)$/$Si(111)$ is energetically favoured by 8 eV/nm^2 caused by crystallographic (topological continuation of the oxygen sublattice avoiding an interface stacking fault) and electronic (conserving the semiconducting character by stabilizing a Pr^{4+} monolayer at the CeO_2/hex-Pr_2O_3 interface) factors. This results show that a thin hex-$Pr_2O_3(0001)$ buffer layer can be used for the growth of $CeO_2(111)$ on $Si(111)$ without an ex-situ annealing step.

4.2 Ternary $Ce_{1-x}Pr_xO_{2-\delta}$ (x = 0-1) mixed oxide systems on Si (111)

4.2.1 Stoichiometry and valence state determination in $Ce_{1-x}Pr_xO_{2-\delta}$ (x = 0-1) thin films

Applying the information of the previous chapter, the epitaxial growth of epitaxial $Ce_{1-x}Pr_xO_{2-\delta}$ (x = 0-1) mixed oxide thin films on Si(111) substrate should be also possible by co-evaporating MBE deposition on an ultra-thin hex-$Pr_2O_3(0001)$ buffer layer, avoiding the formation of an amorphous or polycrystalline mixed oxide. By tuning the deposition rates of ceria and praseodymia, different stoichiometries were achieved. These stoichiometries were in-situ determined by recording the Ce3*d* and Pr3*d* **XPS** spectra (Fig. 4.11) in the binding energy region from 980 eV to 850 eV from six different samples.

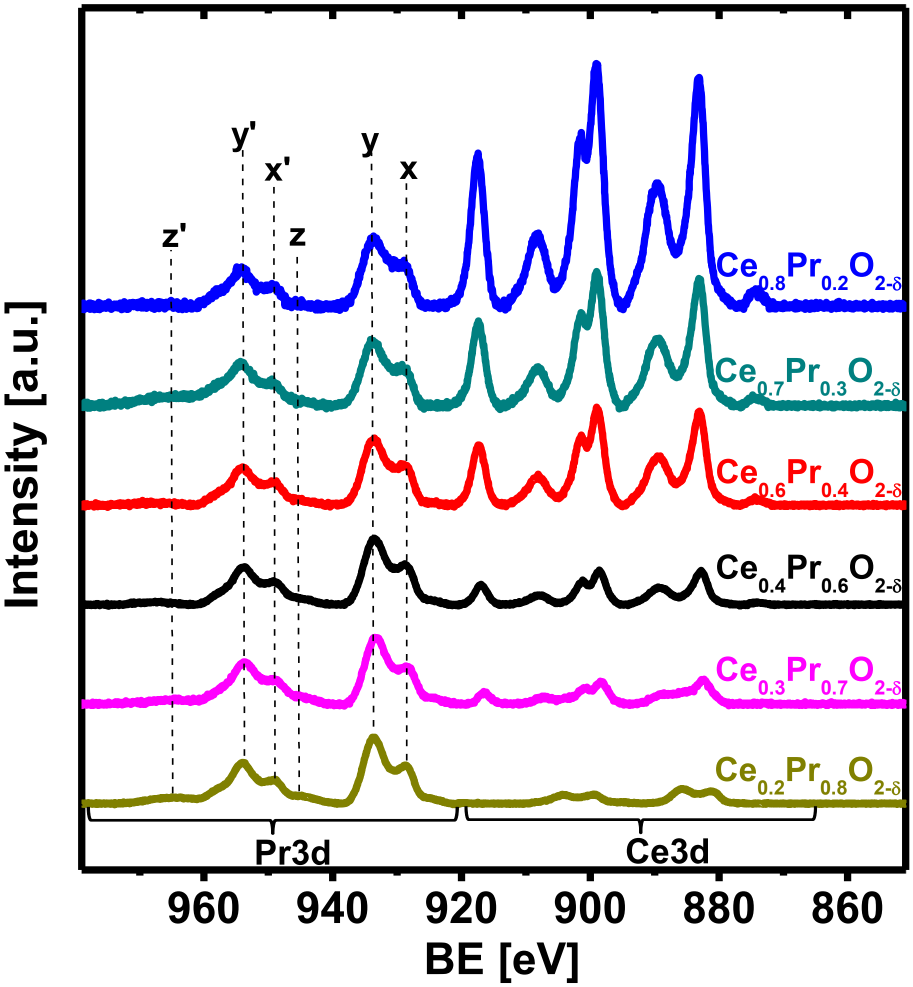

Figure 4.11: XPS 3*d* core level spectra of $Ce_{1-x}Pr_xO_{2-\delta}$ (x = 0-1) with six different stoichiometries.[173]

For the presentation in Fig. 4.11, the intensity of all spectra was normalized to the highest Pr signal (y) and a Shirley background was subtracted. Thus, the different stoichiometries already become evident from Ce 3*d* signal intensities. As described in chapter 3.2.1.3 the stoichiometries were calculated by the equation described by Briggs and Seah, considering the cross sections σ, the angular asymmetry function L, the transmission efficiency of the spectrometer (T_{Ekin}) and the inelastic mean free paths λ.[131] For the latter parameter λ an average value between CeO_2 and Pr_2O_3 was assumed being constant over the whole stoichiometry range. Furthermore, the difference in the asymmetry function L is negligible small. As indicated in Fig. 4.11 the resulting stoichiometries are: $Ce_{1-x}Pr_xO_{2-\delta}$ (x = 0.2, 0.3, 0.4, 0.6, 0.7, 0.8). Since these calculations exhibit some uncertainties, as pointed out before, the assumed error bar amounts up to $\Delta x = \pm 0.05$.

Considering the Pr3*d* region, one can observe a multiple splitting (z', y', x', z, y, x).[87] The signals are separated into two parts, due to spin-orbit coupling (BE(Pr3$d_{3/2}$) - BE(Pr3$d_{5/2}$) ~20 eV) indicated by the prime indices. Since the signal pair z'/z intensity is almost zero, one can deduce from the spectra a Pr^{3+} valence state for all mixtures.[87] The broad and low intensity signals at the z'/z position may come from Pr^{4+} related surface species or some unknown inelastic interactions.[106, 174] Furthermore, after the emission of a 3*d* photoelectron from the $3d^{10}4f^2$ initial state a core hole ($\underline{c}$) is created and charge transfers from the O2*p* valence band to empty *f* states occur.[83] Thus, in the final state a further valence band hole ($\underline{v}$) is created causing a splitting into the signals z, y and x. For the Pr^{3+} case y', x', y as well as x belong to the final states $3d_{3/2}f^2\underline{c}$, $3d_{3/2}f^3\underline{cv}$, $3d_{5/2}f^2\underline{c}$ and $3d_{5/2}f^3\underline{cv}$.

The Ce3*d* region splits in a similar way. However, the concentration from Ce^{3+} and Ce^{4+} ions varies over the stoichiometry range. Therefore, in Fig. 4.12 an enlarged BE region from 922 eV to 876 eV is presented for the stoichiometries $Ce_{0.7}Pr_{0.3}O_{2-\delta}$, $Ce_{0.3}Pr_{0.7}O_{2-\delta}$ and $Ce_{0.2}Pr_{0.8}O_{2-\delta}$. Here, the Ce3*d* spin-orbit splitting (BE(Ce3$d_{3/2}$) – BE(Ce3$d_{5/2}$)) amounts to ~18 eV. The initial state electron configuration of Ce^{3+} ions and Ce^{4+} ions is $3d^{10}f^1$ and $3d^{10}f^0$, respectively. After the photoelectron emission also an O2*p*-Pr4*f* hybridization occurs. Thus, Ce^{3+} exhibits two final states ($4f^1\underline{c}$ and $4f^2\underline{cv}$) and Ce^{4+} exhibits three final states ($4f^0\underline{c}$, $4f^1\underline{cv}$ and $4f^2\underline{cv^2}$). The multitude of 10 signal components with the respective designation was summarized in Tab. 4.2 according to literature.[175-177] Fittings by Voigt functions reveal in a qualitative way, that the Ce^{3+}

concentration is increasing with increasing Pr^{3+} doping concentration. While the $Ce_{0.7}Pr_{0.3}O_{2-\delta}$ shows predominantly Ce^{4+} concentration, the $Ce_{0.2}Pr_{0.8}O_{2-\delta}$ spectra shows a pure Ce^{3+} state. Additionally, the satellite features S_1 and S_2 with unclear origin are observed in the $Ce_{0.2}Pr_{0.8}O_{2-\delta}$ XPS spectra, which seem to be located at relative similar positions as the z/z' signal pair in the Pr3*d* region.[106, 174, 178] $Ce_{0.3}Pr_{0.7}O_{2-\delta}$ represents a mixed Ce^{4+}/Ce^{3+} valency. A quantitative Ce^{3+} determination lacks in precision due to overlapping charge transfer and multiplett splitting.[174]

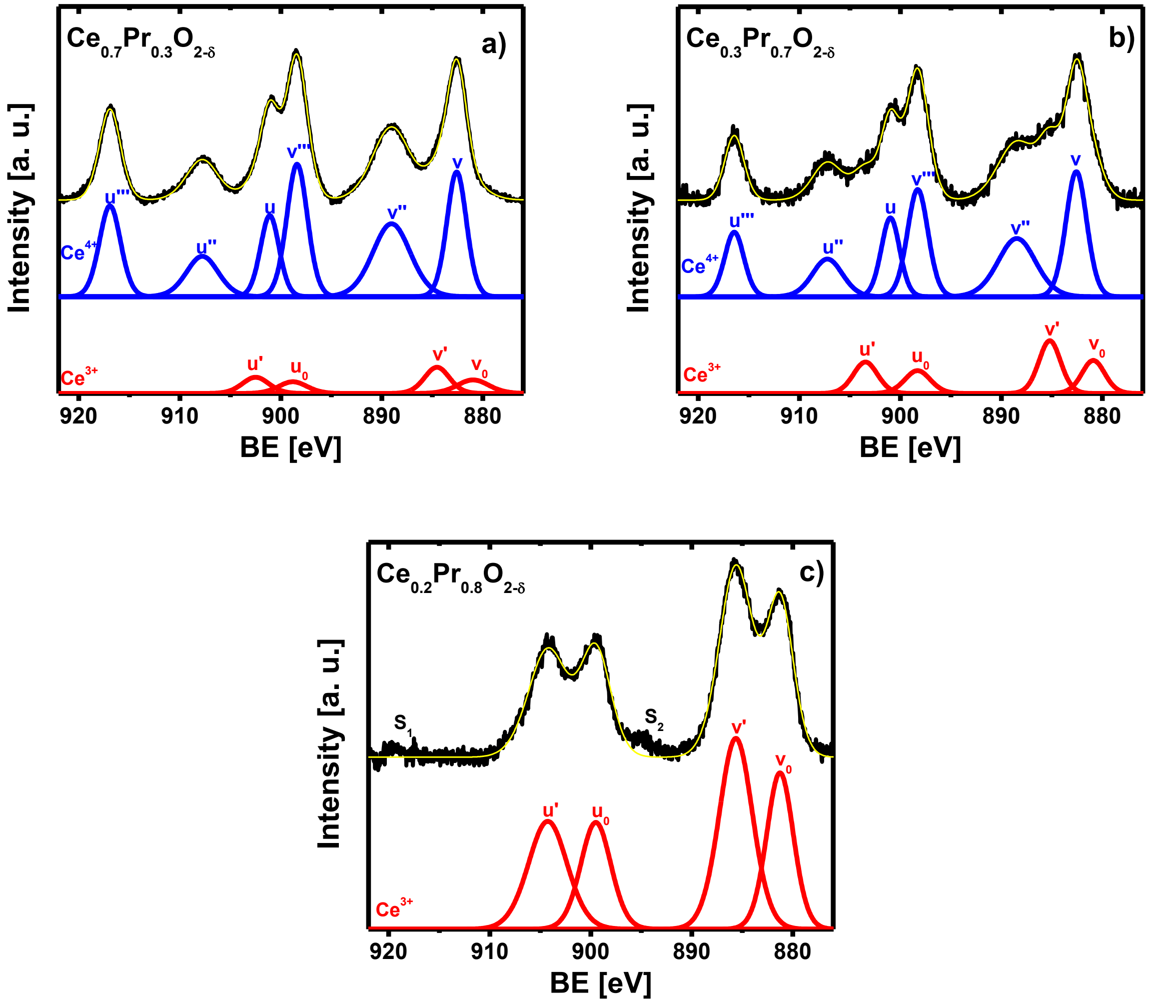

Figure 4.12: XPS Ce3*d* core level spectra of (a) $Ce_{0.7}Pr_{0.3}O_{2-\delta}$, (b) $Ce_{0.3}Pr_{0.7}O_{2-\delta}$ and (c) $Ce_{0.2}Pr_{0.8}O_{2-\delta}$.[173]

Ion	Designation ($Ce3d_{3/2}$ / $Ce3d_{5/2}$)	Initial state	Final state
Ce^{3+}	v_0 / u_0	$3d^{10}4f^{1}$	$3d^{9}4f^{2}\underline{cv}$
	v' / u'	$3d^{10}4f^{1}$	$3d^{9}4f^{1}\underline{c}$
Ce^{4+}	v / u	$3d^{10}4f^{0}$	$3d^{9}4f^{2}\underline{cv}^{2}$
	v'' / u''	$3d^{10}4f^{0}$	$3d^{9}4f^{1}\underline{cv}$
	v''' / u'''	$3d^{10}4f^{0}$	$3d^{9}4f^{0}\underline{c}$

Table 4.2: Nomenclature used for the deconvoluted Ce3*d* Voigt functions.[173, 175]

4.2.2 Structure characterization of epitaxial $Ce_{1-x}Pr_xO_{2-\delta}$ (x = 0-1)/Si(111) systems

At first, the thicknesses were determined by **XRR** in a similar way as for the bilayer structures, resulting in: $Ce_{0.8}Pr_{0.2}O_{2-\delta}$ (24 nm), $Ce_{0.7}Pr_{0.3}O_{2-\delta}$ (20 nm), $Ce_{0.6}Pr_{0.4}O_{2-\delta}$ (23 nm), $Ce_{0.4}Pr_{0.6}O_{2-\delta}$ (24 nm), $Ce_{0.3}Pr_{0.7}O_{2-\delta}$ (22 nm) and $Ce_{0.2}Pr_{0.8}O_{2-\delta}$ (8 nm). Following, to correlate the stoichiometry variation with the crystal structure, extensive **XRD** characterization was performed. The vertical epitaxial relationship was determined for the six different stoichiometries $Ce_{1-x}Pr_xO_{2-\delta}$ (x = 0-1) on a Si(111) substrate. In Fig. 4.13a-f the respective specular θ-2θ scans are presented from 55° to 65°. The net plane bulk values for cub-$Pr_2O_3(444)$ (2θ = 57.18°), $CeO_2(222)$ (2θ = 59.09°) and hex-$Pr_2O_3(0004)$ (2θ = 61.66°) are indicated. Also here, the sharp and most intense double peak at 2θ = 58.88° stems from the Si(222) net planes (Cu $K_{\alpha1}$ and Cu $K_{\alpha2}$). First of all, it is noteworthy that only one single peak can be observed for all mixtures, indicating that the Pr^{3+} and Ce^{4+} ions are incorporated in a common crystal structure. Furthermore, no signal is detected from the ultra-thin hex-$Pr_2O_3(0001)$ buffer, which either might became amorphous by interface reaction or its broad (0004) Bragg peak is hidden in the background due the very limited thickness. In Fig. 4.13a-e the 2θ values for the stoichiometries $Ce_{0.8}Pr_{0.2}O_{2-\delta}$ (2θ = 58.80°), $Ce_{0.7}Pr_{0.3}O_{2-\delta}$ (2θ = 58.68°), $Ce_{0.6}Pr_{0.4}O_{2-\delta}$ (2θ = 58.32°), $Ce_{0.4}Pr_{0.6}O_{2-\delta}$ (2θ = 58.00°) and $Ce_{0.3}Pr_{0.7}O_{2-\delta}$ (2θ = 58.00°) were determined. It is resulting that the peak position is shifting consecutively from $CeO_2(222)$ to cub-$Pr_2O_3(444)$ with increasing praseodymia concentration. Due to the XPS data, this can be clearly attributed to the doping of CeO_2 with the bigger Pr^{3+} ions ($d(Pr^{3+})$ = 1.266 Å) compared to the smaller Ce^{4+} ions ($d(Ce^{4+})$ = 1.110 Å), which are dominating these samples. Interestingly, $Ce_{0.4}Pr_{0.6}O_{2-\delta}$ and $Ce_{0.3}Pr_{0.7}O_{2-\delta}$ show the same 2θ value, which might be related to strain or stoichiometry variation within the error bar of the XPS method. Furthermore, all these samples do have a cub structure with (111) orientation. The sample with the stoichiometry $Ce_{0.2}Pr_{0.8}O_{2-\delta}$ (Fig. 4.13f) represents a special case. Here, the Bragg reflection is not situated in between the cub-$Pr_2O_3(444)$ and $CeO_2(222)$ bulk value, but in between $CeO_2(222)$ and hex-$Pr_2O_3(0004)$ at 2θ = 60.80°. Thus, this already gives a first indication for a hex crystal structure. Since Pr_2O_3 also prefers to grow in a hex structure on Si(111) initially and Ce^{3+} ions ($d(Ce^{3+})$ = 1.283 Å) exhibit a similar ionic radius as Pr^{3+} ions ($d(Pr^{3+})$ = 1.266 Å), this result is comprehensible regarding the Ce^{3+} concentration found by XPS.

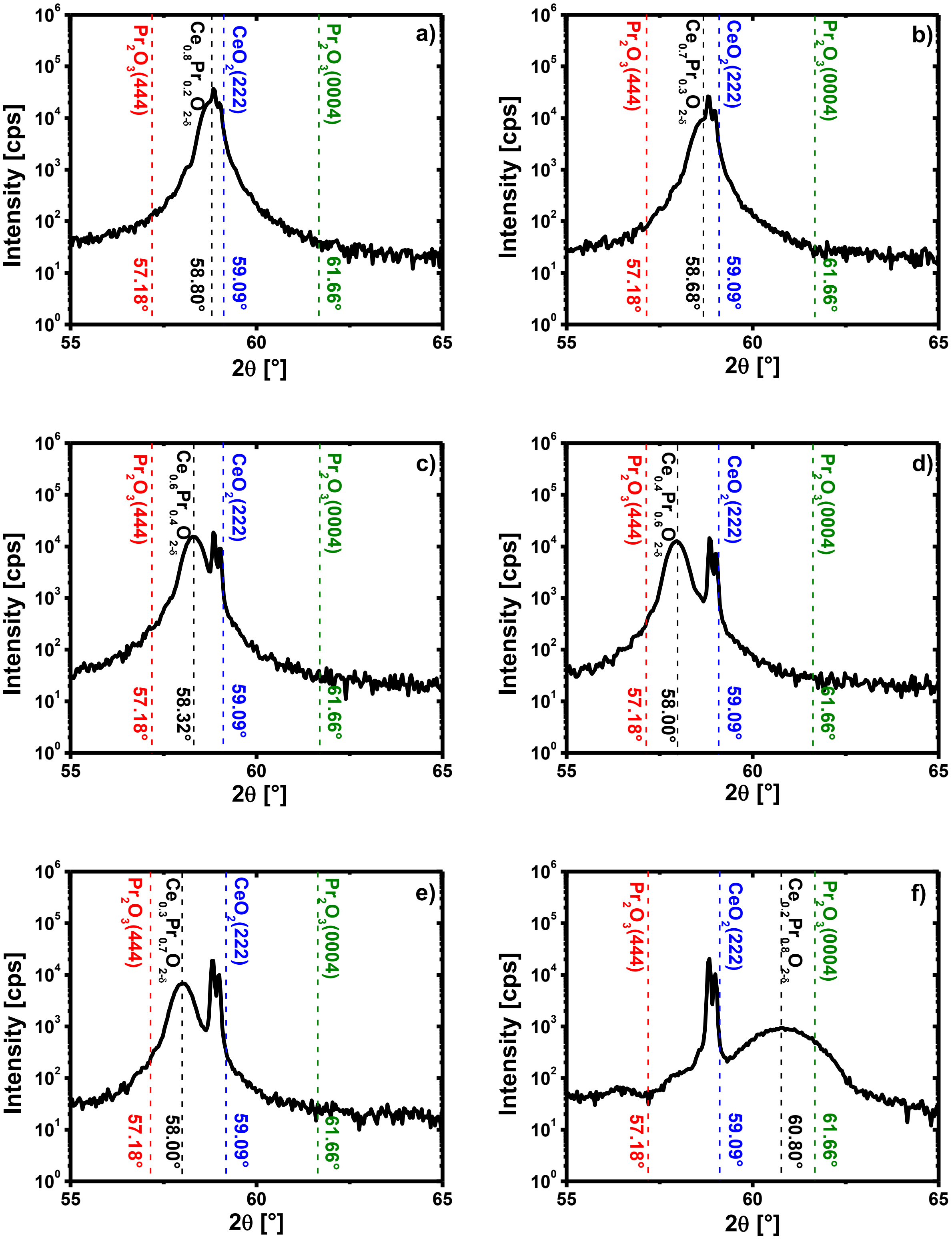

Figure 4.13: Specular θ-2θ measurements of (a) $Ce_{0.8}Pr_{0.2}O_{2-δ}$, (b) $Ce_{0.7}Pr_{0.3}O_{2-δ}$, (c) $Ce_{0.6}Pr_{0.4}O_{2-δ}$, (d) $Ce_{0.4}Pr_{0.6}O_{2-δ}$, (e) $Ce_{0.3}Pr_{0.7}O_{2-δ}$ and (f) $Ce_{0.8}Pr_{0.2}O_{2-δ}$ on a Si(111) substrate.[173, 179]

To determine the lateral epitaxial relationship, the samples with the stoichiometries $Ce_{0.7}Pr_{0.3}O_{2-\delta}$, $Ce_{0.3}Pr_{0.7}O_{2-\delta}$ and $Ce_{0.2}Pr_{0.8}O_{2-\delta}$ were investigated. These samples give a good overview over the stoichiometry range (see XPS analysis), since a sample with predominantly Ce^{4+} ($Ce_{0.7}Pr_{0.3}O_{2-\delta}$) and predominantly Ce^{3+} ($Ce_{0.2}Pr_{0.8}O_{2-\delta}$) is presented. Additionally, the transition case with mixed Ce^{3+}/Ce^{4+} valency ($Ce_{0.3}Pr_{0.7}O_{2-\delta}$) is shown. For both cub samples ($Ce_{0.7}Pr_{0.3}O_{2-\delta}$ and $Ce_{0.3}Pr_{0.7}O_{2-\delta}$) synchrotron radiation **GIXRD** studies were performed (Fig. 4.14a-d). By investigating the $[10L]^S$ and $[01L]^S$ rod, this will give additional information about the stacking twin concentration. Considering, the $[10L]^S$ rod, the sharp and intense signals can be attributed to the Si$(11\bar{1})$ at *L = 1/3 r.l.u.* and Si(220) at *L = 4/3 r.l.u.* (Fig. 4.14a and b). The reflections (002) and (113) from the mixed oxide (Ox) layer can be found at about *L = 2/3 r.l.u.* and *L = 0.5/3 r.l.u.* Thus, a type-B orientation could be identified (as for the bilayer stacking). To determine the type-A/B stacking twin ratio, the I_{max} criterion is indicated for the Ox(002) reflections. In the $[01L]^S$ rod, the type-B related Ox$(1\bar{1}1)$ and Ox(131) are located close to the positions *L = 1/3 r.l.u.* and *L = 4/3 r.l.u.*, where previously the respective Si signals were detected. Thus, the Si(113) is now detected at *L = 5/3 r.l.u.* Also here, the absence of the Si(020) enables to find potential type-A oriented domains. In contrast to the $CeO_2(111)$/hex-$Pr_2O_3(0001)$/Si(111) bilayer sample, in the mixed oxide samples weak signals from type-A stacking twins are detected at *L = 2/3 r.l.u*. The type-A domain concentration within the predominantly type-B oriented mixed oxide films amounts to about 0.1% in $Ce_{0.7}Pr_{0.3}O_{2-\delta}$ and 1.0% in $Ce_{0.3}Pr_{0.7}O_{2-\delta}$. For the hexagonal $Ce_{0.2}Pr_{0.8}O_{2-\delta}$ sample, the in-plane orientation with respect to the Si substrate was investigated by a **pole figure** measurement. Therefore, a $2\theta = 56.5°$ value was chosen, which is located in between the Si ($2\theta = 56.13°$) and hex-Pr_2O_3 ($2\theta = 57.12°$) signal. In the pole figure (Fig. 4.15) the following peaks can be detected: Si$\{113\}$ (open triangles: $\chi = 29.5°$), Si$\{1\bar{1}3\}$ (open squares: $\chi = 58.52°$), Si$\{\overline{11}3\}$ (open pentagones: $\chi = 79.98°$) and hex-$Pr_2O_3\{02\bar{2}1\}$ (open circles: $\chi = 75.00°$). The 6-fold symmetry corresponds thus to a hex-$Ce_{0.2}Pr_{0.8}O_{2-\delta}(0001)$ thin film. Summarizing, the epitaxial relationships are given by:

cub-$Ce_{0.7}Pr_{0.3}O_{2-\delta}(111);\ \langle 11\bar{2}\rangle||Si(111);\ \langle\overline{11}2\rangle$

cub-$Ce_{0.3}Pr_{0.7}O_{2-\delta}(111);\ \langle 11\bar{2}\rangle||Si(111);\ \langle\overline{11}2\rangle$

hex-$Ce_{0.2}Pr_{0.8}O_{2-\delta}(0001);\ \langle\bar{1}100\rangle||Si(111);\ \langle\overline{11}2\rangle$

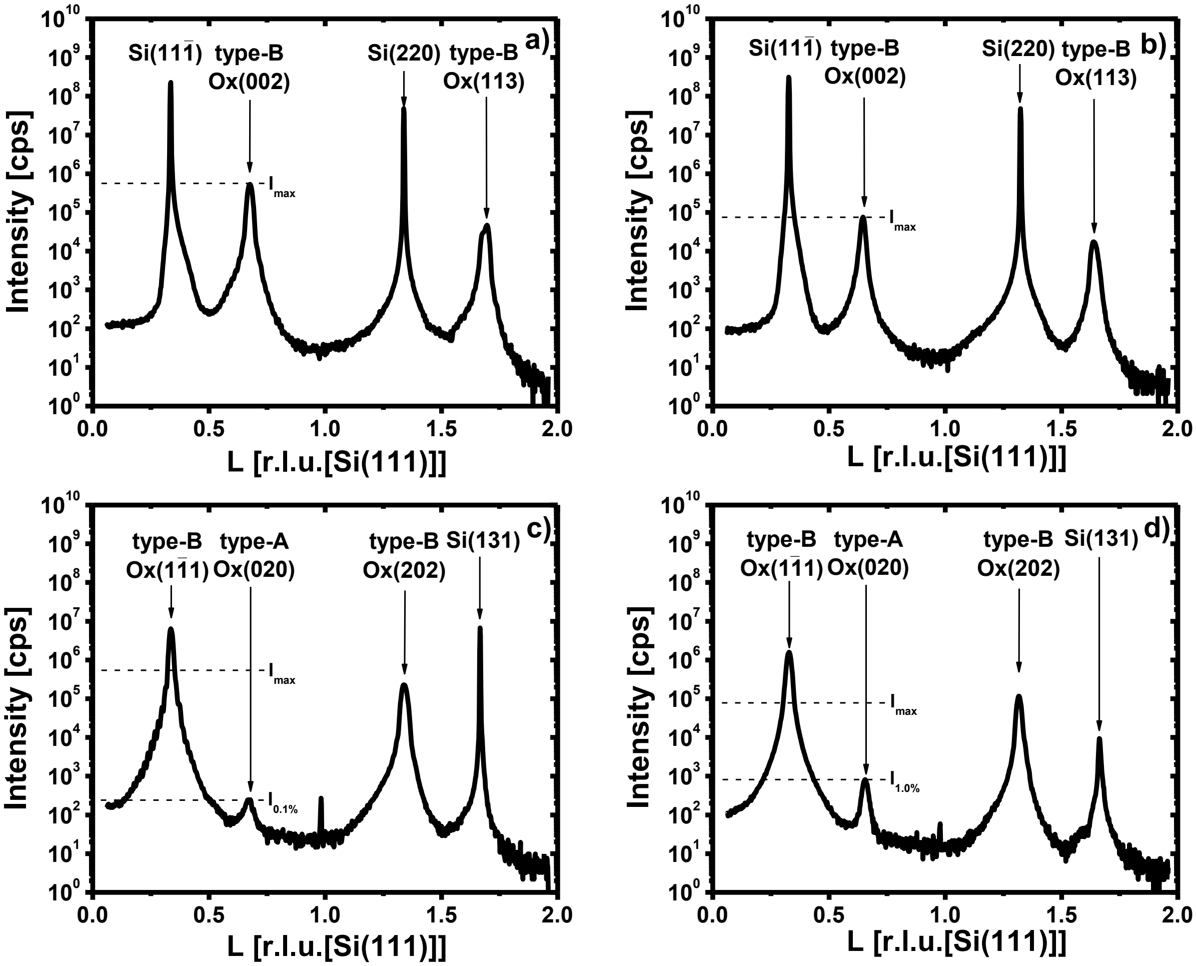

Figure 4.14: GIXRD scan along $[10L]^S$ rod of (a) $Ce_{0.7}Pr_{0.3}O_{2-\delta}$/Si(111) and (b) $Ce_{0.3}Pr_{0.7}O_{2-\delta}$/Si(111), and along $[01L]^S$ rod of (c) $Ce_{0.7}Pr_{0.3}O_{2-\delta}$/Si(111) and (d) $Ce_{0.3}Pr_{0.7}O_{2-\delta}$/Si(111).[173]

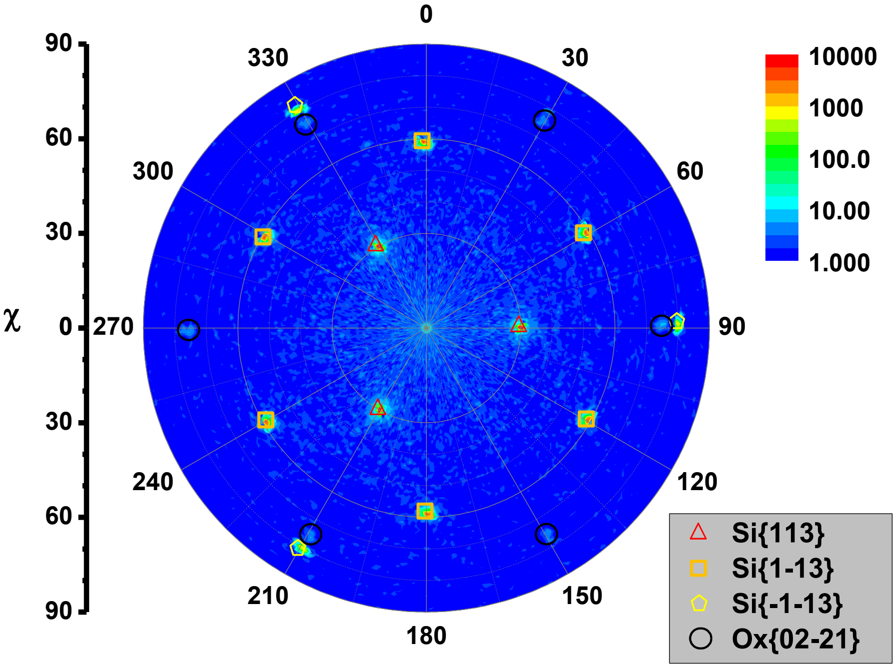

Figure 4.15: Pole figure of $Ce_{0.2}Pr_{0.8}O_{2-\delta}$/Si(111) measured at 2θ = 56.5°.[173]

The crystal phase is clarified for the hex case (hex-$Ce_{0.2}Pr_{0.8}O_{2-\delta}$), but for the cub crystal structure two possible cases exist, namely a REO_2 related fluorite (based on CeO_2 component) and a RE_2O_3 related bixbyite (based on cub-Pr_2O_3 component) phase. To identify the crystal structure an in-plane scan by synchrotron radiation **GIXRD** along the $[H00]^S$ direction was performed (Fig. 4.16). The fluorite (f) related signal f$(11\bar{2})$ is located at about *H = 1.5 r.l.u.* and f$(22\bar{4})$ at about *H = 3 r.l.u*. As the bixbyite (bb) lattice is twice as big as the fluorite lattice, the bb$(11\bar{2})$, bb$(22\bar{4})$, bb$(33\bar{6})$ and bb$(44\bar{8})$ reflections would appear at the positions *H = 0.75n (n = 1, 2, 3, 4)*, respectively. It has to be mentioned that the f$(11\bar{2})$ and bb$(22\bar{4})$ have a very small structure factor and thus cannot be detected. In Fig. 4.16a and b very sharp features are present at the positions *H = 1* and *H = 3*, which are related to the CTRs of the Si(111) substrate. Considering Fig. 4.16a, only one other broad peak at *H = 3* from the f$(22\bar{4})$ net planes is detected, clarifying the fluorite lattice structure of the cub-$Ce_{0.7}Pr_{0.3}O_{2-\delta}(111)$ thin film. In Fig. 4.16b (cub-$Ce_{0.3}Pr_{0.7}O_{2-\delta}(111)$), another broad peak at *H = 2.25* can be attributed to the bb$(33\bar{6})$ reflection. The other bixbyite related bb$(11\bar{2})$ reflection is not observed, since it is probably overshadowed by the increasing diffused X-ray scattering close to the direct beam. Nevertheless, a bixbyite structure is found. Resulting, the peak close to *H = 3* cannot anymore exclusively be designated as f$(22\bar{4})$, but also as the bb$(44\bar{8})$. In other words, it is not unambiguously clear whether only a bixbyite crystal structure or a bixbyite structure with fluorite inclusions is present in the cub-$Ce_{0.3}Pr_{0.7}O_{2-\delta}(111)$/Si$(111)$ sample. Post festum, it has to be mentioned that the mixed oxide peaks are not exactly positioned at *H = 0.75n (n = 1, 2, 3, 4)*, indicating a non-pseudomorphic growth.

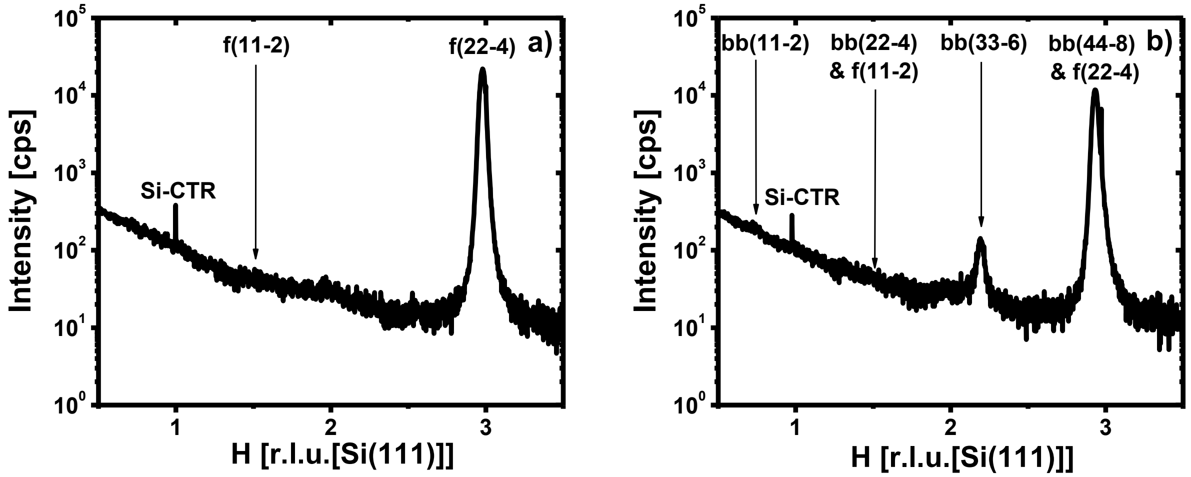

Figure 4.16: GIXRD scan along the $[H00]^S$ direction of (a) $Ce_{0.7}Pr_{0.3}O_{2-\delta}$/Si(111) and (b) $Ce_{0.3}Pr_{0.7}O_{2-\delta}$/Si(111).[173]

The strain status of the mixed oxides with a cub crystal structure ($Ce_{0.8}Pr_{0.2}O_{2-\delta}$, $Ce_{0.7}Pr_{0.3}O_{2-\delta}$, $Ce_{0.6}Pr_{0.4}O_{2-\delta}$, $Ce_{0.4}Pr_{0.6}O_{2-\delta}$ and $Ce_{0.3}Pr_{0.7}O_{2-\delta}$) was determined by the **$\cos^2\chi$ method**, which are presented in Fig. 4.17a-e. For this purpose, the respective asymmetric Bragg reflections were analyzed by θ-2θ scans under the following inclination angles χ: $\chi_{(11\bar{1})}$ = 70.5°,$\chi_{(400)}$= 54.7°, $\chi_{(3\bar{1}3)}$= 48.5°, $\chi_{(511)}$= 38.9°, $\chi_{(220)}$= 35.3°, $\chi_{(311)}$= 29.5°, $\chi_{(422)}$= 19.5° and $\chi_{(222)}$= 0°. From the in-plane a_0 and off-plane a_1 lattice constant the in-plane strain $\varepsilon_{||} = (a_0 - a_{bulk})/a_{bulk}$ was calculated and summarized in Tab. 4.3. It is resulting, that all samples (apart from $Ce_{0.7}Pr_{0.3}O_{2-\delta}$) exhibit a negative in-plane strain $\varepsilon_{||}$. Furthermore, the strain value is very small, even less than for pure $CeO_2(111)$ on a hex-$Pr_2O_3(0001)$/Si(111) support. This is quite surprising, since pure CeO_2 is closer to the lattice match with the buffer layer. Reminding that CeO_2 grows highly strained on a cub-Pr_2O_3 buffer layer, the difference in the relaxation mechanism may be based on the crystal structure transition from the hex-Pr_2O_3 to the cub-$Ce_{1-x}Pr_xO_{2-\delta}$. Thus, one possible explanation is that a high defect concentration is built in during the growth.

stoichiometry	a_0 [nm]	a_1 [nm]	$\varepsilon_{\|\|}$ [%]	a_{bulk} [nm]
$Ce_{0.8}Pr_{0.2}O_{2-\delta}$	0.5452	0.5457	-0.05	0.5455
$Ce_{0.7}Pr_{0.3}O_{2-\delta}$	0.5452	0.5445	0.07	0.5448
$Ce_{0.6}Pr_{0.4}O_{2-\delta}$	0.5477	0.5485	-0.08	0.5481
$Ce_{0.4}Pr_{0.6}O_{2-\delta}$	0.5496	0.5515	-0.18	0.5506
$Ce_{0.3}Pr_{0.7}O_{2-\delta}$	0.5505	0.5517	-0.11	0.5511

Table 4.3: In-plane (a_0), off-plane (a_1), bulk (a_{bulk}) lattice constant and in-plane strain ($\varepsilon_{||}$) in dependence of the stoichiometry determined by the $\cos^2\chi$ method.

Knowing a_0 and a_1 enables to calculate the bulk lattice constant a_{bulk} by the Poisson ratio ν:

$$\frac{(a_1 - a_{bulk})}{a_{bulk}} = \frac{(a_0 - a_{bulk})}{a_{bulk}} * \frac{-2\upsilon}{1-\upsilon} \quad or \quad a_{bulk} = \frac{a_1 + a_0 P}{1 + P} \quad with \quad P = \frac{2\upsilon}{1-\upsilon} \qquad \mathbf{(4.1)}$$

For the poisson ratio a value of ν = 0.33 was assumed. This value derives from the average between a pure cub-$Pr_2O_3(111)$/Si(111) (ν = 0.32)[172] thin film and a pure CeO_2(111)/cub-Pr_2O_3(111)/Si(111) (ν = 0.34) thin film investigated in the previous chapter. By determining a_{bulk} and assuming Vegard´s law, the stoichiometry of the $Ce_{1-x}Pr_xO_{2-\delta}$ (x = 0-1) mixed oxide thin films can be evaluated. In Fig. 4.17f the calculated a_{bulk} values (red squares) are plotted versus the Pr concentration c(Pr) with the assumed error bar (Δx = ±0.05) from the XPS stoichiometry determination. The black circles give the respective pure bulk values of CeO_2, cub-Pr_2O_3, Pr_6O_{11} and PrO_2. Vegard's law is indicated by the black dotted lines. Furthermore, literature values

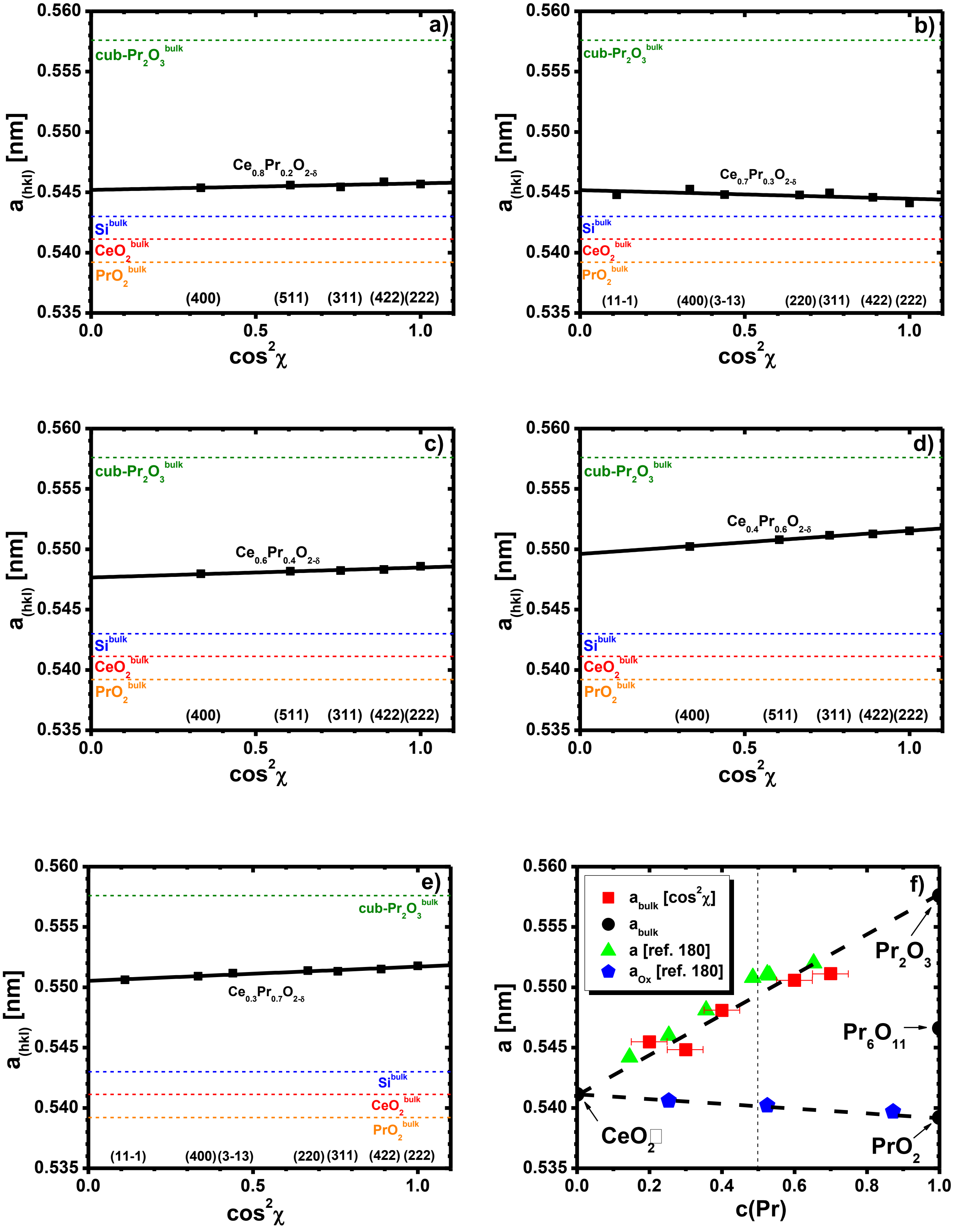

Figure 4.17: Strain analyzis using the cos$^2\chi$ method of (a) $Ce_{0.8}Pr_{0.2}O_{2-\delta}$, (b) $Ce_{0.7}Pr_{0.3}O_{2-\delta}$, (c) $Ce_{0.6}Pr_{0.4}O_{2-\delta}$, (d) $Ce_{0.4}Pr_{0.6}O_{2-\delta}$ and (e) $Ce_{0.3}Pr_{0.7}O_{2-\delta}$. (f) Dependency of a_{bulk} from c(Pr).[173]

from $Ce_{1-x}Pr_xO_{2-\delta}$ (x = 0-1) mixed oxide powder studies are indicated (green triangles as-prepared; blue pentagons heated in oxygen towards fluorite structure).[180] The experimentally derived stoichiometries do not completely fit to the Vegard's law within the assumed error bar. However, it is noteworthy that the literature study implies a linear behavior with a higher slope than predicted by the Vegard's law.[180] Furthermore, it is noted that above a stoichiometry of x = 0.5 a phase separation occurs. A lattice constant below the theoretical values might be explained by an oxidation process in atmosphere, resulting in Pr^{4+} formation causing a shrinking lattice constant.

Supplementary, it can be stated that the increasing lattice constant is intrinsically caused by Pr^{3+} incorporation and not extrinsically by strain. Thus, a $REO_{2-\delta}$ fluorite matrix with oxygen deficiency δ is given for the Pr poor samples and a RE_2O_3 related bixbyite matrix with potential fluorite inclusions is given for the cub Pr rich samples. In any case, this should lead to oxygen vacancies (charge neutrality) and defects (fluorite lattice distortion) within the crystal structure, which can be investigated by **Raman spectroscopy**. Since the He-Cd UV-laser (λ = 325nm) penetrates the whole $Ce_{1-x}Pr_xO_{2-\delta}$ (x = 0-1) thin film, bulk information and even the transverse optical mode from the Si substrate is detected.[181] This enables to reference and normalize all signals to the Si peak, appearing at 520 cm^{-1}. The mixed oxide layer response to the laser excitation is characterized by three signals (γ, α, β)[182] within the investigated range from 400 cm^{-1} to 700 cm^{-1}. Deriving from theoretical calculations on doped CeO_2 from Nakajima *et al.*[183] the signals (shown in Fig. 4.18) can be described as following:

1) γ is located at 460 cm^{-1} and corresponds to the oxygen breathing mode F_{2g} around the 4+ valent cation M^{4+} with O_h symmetry ($M^{4+}O_8$ type complex). This signal is typical for the fluorite crystal structure of CeO_2.
2) α is located at 570 cm^{-1} and corresponds to an oxygen vacancy $V_O^{\bullet\bullet}$, predominantly described by an $V_O^{\bullet\bullet}O_6$ defect type with O_h symmetry, which might be distorted in dependence on the cation coordination sphere.
3) β is located at 600 cm^{-1} and corresponds to another oxygen breathing mode including a cation with bigger ionic radii. This is the case for the trivalent cations (Ce^{3+}, Pr^{3+}), thus forming a $M^{3+}O_8$ defect configuration.

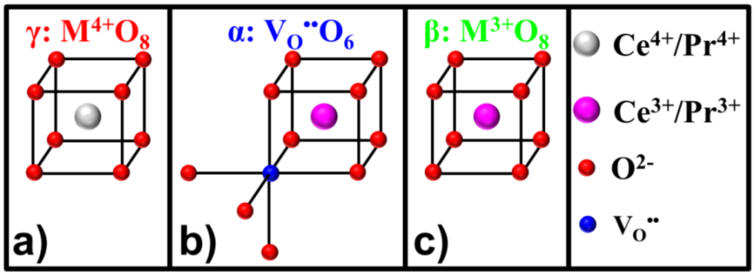

Figure 4.18: . Different complex types a) γ: $M^{4+}O_8$; b) α: $V_O^{\bullet\bullet}O_6$; and c) β: $M^{3+}O_8$ giving a Raman signal.[184]

In Fig. 4.19a the Raman spectra for $Ce_{1-x}Pr_xO_{2-\delta}(111)/Si(111)$ (x = 0, 0.2, 0.4, 0.6, 1) are presented. Apart from the α signal, in the pure $CeO_2(111)$ thin film only a very weak defect related signal can be detected, which probably results from the Ce^{4+}-Pr^{3+} exchange at the interface to the ultra-thin Pr_2O_3 buffer layer. In contrast, the pure cub-$Pr_2O_3(111)$ thin film shows no signal at all. The mixtures show a successive decrease of the overall intensities for all oxide signals with increasing Pr^{3+} doping concentration, which is related to two facts. On the one hand, cub-Pr_2O_3 exhibits a bixbyite crystal structure gradually breaking the O_h symmetry. On the other hand, the signal intensity is reducing due to the fluorescence effect from pure Pr_2O_3. Furthermore, a shift and a broadening of the γ signal can be observed, shown in Fig. 4.19b. Factors as phonon confinement, strain, defects etc. influence the peak position and shape.[185] In this case, the main responsible factor is the lattice expansion by the Pr^{3+} ion doping as discussed by XRD results. The broadening is likewise based on the Pr^{3+} doping and the related fluorite lattice distortion, which is also responsible for the decreasing signal intensity. Such a stoichiometry dependent behavior of the Raman spectra was investigated for several doped CeO_2 materials by McBride *et al.* (e.g. La^{3+}, Gd^{3+}, $Pr^{3+/4+}$).[182, 183, 185, 186] Furthermore, the defect type complexes $V_O^{\bullet\bullet}O_6$ (α) and $M^{3+}O_8$ (β) vary also in their relative intensity. For this purpose, the relative signals $V_\alpha = A_\alpha/(A_\alpha + A_\beta + A_\gamma)$ (blue line) and $V_\beta = A_\beta/(A_\alpha + A_\beta + A_\gamma)$ (red line) are plotted in Fig. 4.19c. While a relatively high signal V_α (related to the $V_O^{\bullet\bullet}$) is observed for the Pr poor and medium sample ($Ce_{0.8}Pr_{0.2}O_{2-\delta}(111)/Si(111)$ and $Ce_{0.6}Pr_{0.4}O_{2-\delta}(111)/Si(111)$), the Pr rich sample ($Ce_{0.4}Pr_{0.6}O_{2-\delta}(111)/Si(111)$) shows a drastical intensity loss. The relative signal V_β ($M^{3+}O_8$ type complex) behaves inverse, and shows an increasing intensity. Thus, it is shown that doping of CeO_2 by Pr^{3+} introduces $V_O^{\bullet\bullet}$ and forms $M^{3+}O_8$ defect complexes. However, a further doping leads to a lattice distortion in favor of the bixbyite structure as discussed by XRD. Thus, the relative signal V_α is expected to decrease.

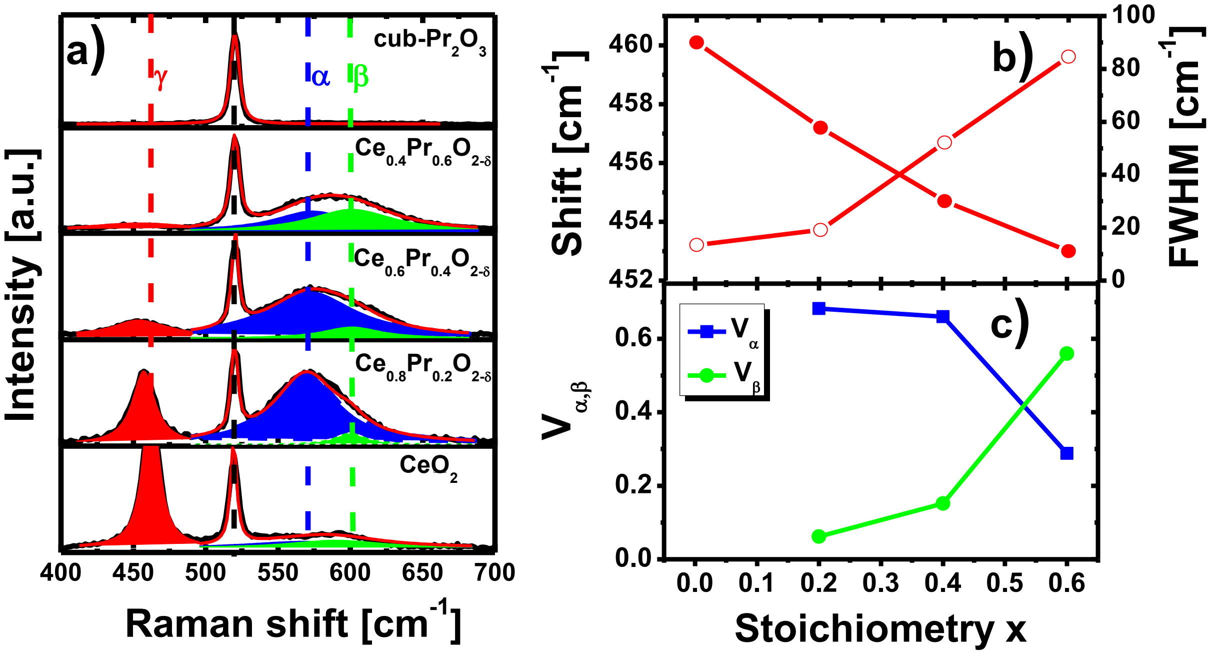

Figure 4.19: (a) Raman spectra of CeO_2(111)/Si(111), $Ce_{0.8}Pr_{0.2}O_{2-\delta}$(111)/Si(111), $Ce_{0.6}Pr_{0.4}O_{2-\delta}$(111)/Si(111), $Ce_{0.4}Pr_{0.6}O_{2-\delta}$(111)/Si(111) and cub-$Pr_2O_3$(111)/Si(111). (b) α peak shift (red full circles) and broadening (red open circles) in dependence on the stoichiometry. (c) Stoichiometry dependent evolution of the defect related relative signal intensities V_α (blue line) and V_β (green line).[179]

4.2.3 Conclusion

By an ultra-thin hex-Pr_2O_3(0001) buffer layer it became possible to grow epitaxial $Ce_{1-x}Pr_xO_{2-\delta}$ (x = 0-1) mixed oxide thin films on a Si(111) substrate. The thickness was determined by XRR and the stoichiometry by XPS from the following six samples: $Ce_{0.8}Pr_{0.2}O_{2-\delta}$ (24 nm), $Ce_{0.7}Pr_{0.3}O_{2-\delta}$ (20 nm), $Ce_{0.6}Pr_{0.4}O_{2-\delta}$ (23 nm), $Ce_{0.4}Pr_{0.6}O_{2-\delta}$ (24 nm), $Ce_{0.3}Pr_{0.7}O_{2-\delta}$ (22 nm) and $Ce_{0.2}Pr_{0.8}O_{2-\delta}$ (8 nm). Additionally, it was found that by doping with Pr^{3+} the Ce^{3+} valence state becomes more stable and the Ce^{3+} valence state was even completely stabilized in a hex-P_2O_3 matrix. In contrast, a stabilization of the Pr^{4+} state by Ce^{4+} was not observed and thus plasma-oxidation is still needed. The epitaxial relationships were measured by laboratory and synchrotron based XRD techniques (θ-2θ, pole figure, GIXRD). Although, the in-plane orientation was only determined for certain samples one can in general distinguish between hex and cub samples. In detail, only the sample with the highest Pr concentration (x = 0.2) has a hex phase and all other have a cub phase. Thus the epitaxial relationships are given by:

cub-$Ce_{1-x}Pr_xO_{2-\delta}(111)$; $\langle 11\bar{2}\rangle||Si(111)$; $\langle\overline{11}2\rangle$ $\quad for \quad x = 0.8, 0.7, 0.6, 0.4, 0.3$

hex-$Ce_{1-x}Pr_xO_{2-\delta}(0001)$; $\langle\bar{1}100\rangle||Si(111)$; $\langle\overline{11}2\rangle$ $\quad for \quad x = 0.2$

However, the cub structures can exhibit either a fluorite or bixbyite lattice. Samples with dominating 4+ valent cations prefer an oxygen deficient fluorite matrix. In contrast, the more 3+ valent cations are existing the more the lattice becomes distorted and finally a bixbyite structure with potential fluorite inclusions is resulting. This thesis is supported by findings of McCullough *et al.*[180] on powder samples, who presents a linear behavior of the lattice constant with increasing Pr doping concentration (Vegard's law) but reports on a phase separation above x = 0.5. Furthermore, this conclusion is in line with the Raman spectroscopy data, which show a high oxygen vacancy concentration for slightly and medium doped samples, but a more defective structure for higher doping concentrations. Accordingly, it is also shown that at least below x = 0.5 the Pr^{3+} cation are really incorporated in the lattice structure forming a solid solution instead of clustering in a separated phase. This behavior was previously observed for a similar REO film system by extended X-ray absorption fine structure (EXAFS), namely $Pr_{2-x}Y_xO_3(111)$.[20]

4.3 Reduction of oxidized $Ce_{1-x}Pr_xO_{2-\delta}$ (x = 0-1) mixed oxide thin films

4.3.1 Oxygen release

Since the growth of epitaxial $Ce_{1-x}Pr_xO_{2-\delta}$ (x = 0-1) mixed oxide thin films became possible, the structure is clarified and a first indication on the tunable valence state exchange M^{4+}/M^{3+} (M = Pr, Ce) was observed, the reduction behavior was investigated in more detail as next step. Therefore, a cub-$Pr_2O_3(111)$/Si(111) and three cub-$Ce_{1-x}Pr_xO_{2-\delta}(111)$/Si$(111)$ samples were in-situ investigated by **TPD** after plasma-oxidation and cleaning. Thus, the samples should exhibit a "clean" surface and no oxygen deficiency. In Fig. 4.20a, the O_2 spectra of 11nm $PrO_2(111)$ (black curve), 24 nm $Ce_{0.4}Pr_{0.6}O_2(111)$ (green curve), 23 nm $Ce_{0.6}Pr_{0.4}O_2(111)$ (red curve) and 24 nm $Ce_{0.8}Pr_{0.2}O_2(111)$ (blue curve) are presented. The pure PrO_2 spectrum shows a complex shape with several maxima related to certain phase transitions, which are discussed by Wilkens *et al.*[187] Here, just the global maximum is considered as starting point for the oxygen release of the fluorite lattice. The higher the Pr concentration, the less symmetric is the shape of the TPD

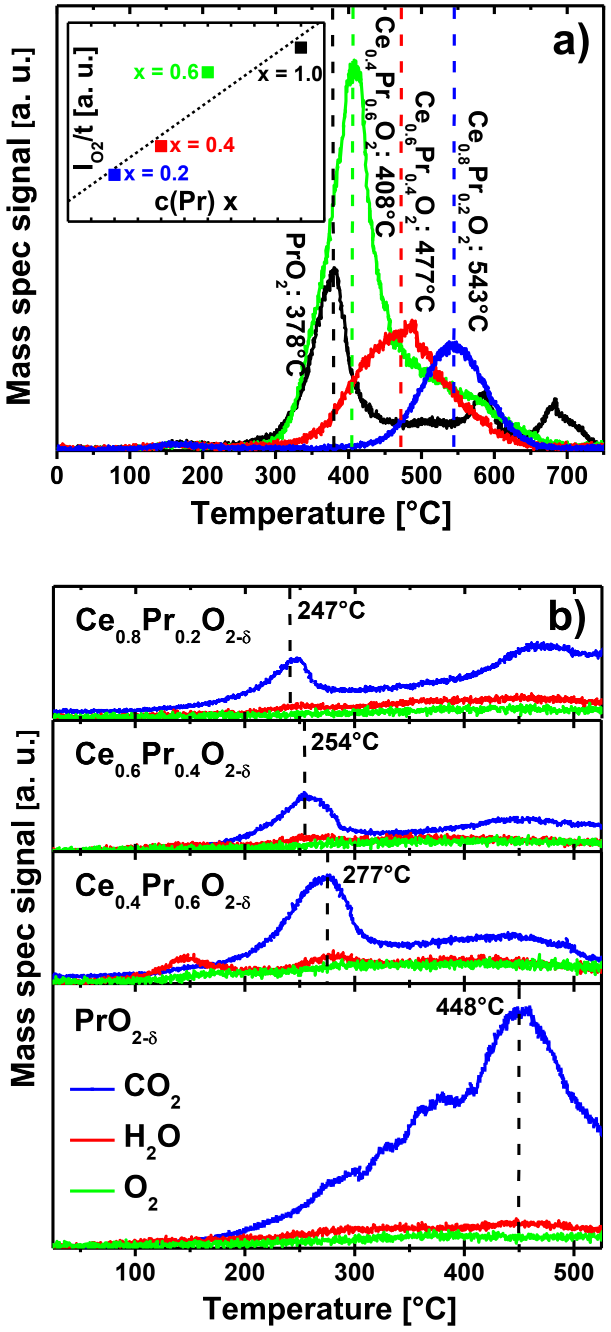

Figure 4.20: TPD spectra of $Ce_{1-x}Pr_xO_{2-\delta}$(111)/Si(111) samples treated a) in-situ with oxygen plasma b) ex-situ with molecular oxygen.[180]

spectra and the lower the oxygen desorption maximum becomes ($T_{O2}^{x=0.2} = 543^\circ C$; $T_{O2}^{x=0.4} = 477^\circ C$; $T_{O2}^{x=0.6} = 408^\circ C$; $T_{O2}^{x=1.0} = 378^\circ C$). This result agrees with calculations by Tang *et al.*[188], who predicts a lowering of the activation energy for oxygen vacancies in Pr doped CeO_2. Additionally, it turned out that the integral intensity I_{O2} with respect to the layer thickness t ($I_{O2}^{x=0.2}/t = 23$; $I_{O2}^{x=0.4}/t = 38$; $I_{O2}^{x=0.6}/t = 75$; $I_{O2}^{x=1.0}/t = 87$) is linearly increasing with the Pr concentration as indicated by the inset of Fig. 4.20a. On the one hand, this enables to engineer the OSC by Pr doping and on the other hand this demonstrates the inferior participation of the Ce^{4+} reduction to the oxygen release. This is corroborated by previous studies, which show that the Pr^{4+} reduction in such $Ce_{1-x}Pr_xO_{2-\delta}$ mixed oxides proceeds at much lower temperatures than the Ce^{4+} reduction.[174, 189]

However, further temperature dependent investigations on the lattice structure, the valence state change and the defect characterization were performed ex-situ. For a coherent study, in Fig. 4.20b the O_2, CO_2 and H_2O spectra of all atmosphere exposed samples are presented. It has to be noted that the carbonaceous contaminations on the samples are undefined, but assumed to be similar on all samples considering the same storage history. Thus, no signal from molecular oxygen O_2 was detected, but from the combustion products CO_2 ($T_{CO2}^{x=0.2} = 247^\circ C$; $T_{CO2}^{x=0.4} = 254^\circ C$; $T_{CO2}^{x=0.6} = 277^\circ C$; $T_{CO2}^{x=1.0} = 448^\circ C$) and a little H_2O. In general, the maximum desorption temperature T_{CO2} is lower than T_{O2} for the respective mixture ($T_{CO2}^{x=0.2} < T_{O2}^{x=0.2}$; $T_{CO2}^{x=0.4} < T_{O2}^{x=0.4}$; $T_{CO2}^{x=0.6} < T_{O2}^{x=0.6}$). This behaviour might be based on the kinetically favoured oxidation of hydrocarbons in comparison to the recombination and desorption of molecular oxygen. Furthermore, in contrast to the signal T_{O2} from the plasma-oxidized samples, the atmosphere exposed samples show a vice versa tendency of the CO_2 desorption temperature maximum T_{CO2} with increasing Pr concentration, namely higher desorption temperatures. Considering the higher catalytic activity for hydrocarbon oxidation of ceria (the highest among all other REOs e.g. for propylene and n-butane)[1] in $Ce_{1-x}Pr_xO_{2-\delta}(111)$ the reason for this inversed temperature tendency originates from the inferior catalytic activity from praseodymia. In addition, Sato et al.[190] found by TPDs that CO_2 desorbs already at ~100°C from CeO_2 and at ~300°C from Pr_6O_{11} and thus that CeO_2 exhibits a lower basicity compared to Pr_6O_{11}. Possibly, the reaction mechanism on Pr rich samples might be kinetically hindered by the more stable carbonate species. This might also explain the asymmetric shape of the CO_2 desorption with a tail towards lower temperatures.

4.3.2 Crystal lattice rearrangement

As it is pointed out during the structure characterization of the mixed oxide samples, the reduction/oxidation process will have an inherent influence on the crystal lattice. This was investigated by **specular θ-2θ scans** (Fig. 4.21a-c) from 55° to 62° for the three mixed oxide samples ($Ce_{0.8}Pr_{0.2}O_{2-\delta}(111)$, $Ce_{0.6}Pr_{0.4}O_{2-\delta}(111)$ and $Ce_{0.4}Pr_{0.6}O_{2-\delta}(111)$) previously characterized by TPD. As known, the sharp and most intense double peak was designated to Si(222). The remaining peak can be attributed to the cub-$Ce_{1-x}Pr_xO_{2-\delta}(222)$ or cub-$Ce_{1-x}Pr_xO_{2-\delta}(444)$ reflection, in dependence of the crystal structure (fluorite or bixbyite). At this point it should be mentioned, that the sample with highest Pr concentration ($Ce_{0.4}Pr_{0.6}O_{2-\delta}(111)$) exhibits for some reduction steps a shoulder at the lower angle side. This is related to a phase separation as pointed out in chapter 4.2.2 and might be described by a two column model (as done for pure $PrO_2(111)$ thin film reduction on Si(111)).[119] Here, the signal from the phase with the highest intensity was used for further consideration. It can be observed that the main reflection peak is consecutively shifting after each annealing step (A = 50°C, B = 200°C, C = 250°C, D = 300°C, E = 500°C) to lower angles. Thus, the reduction process induces an expanding

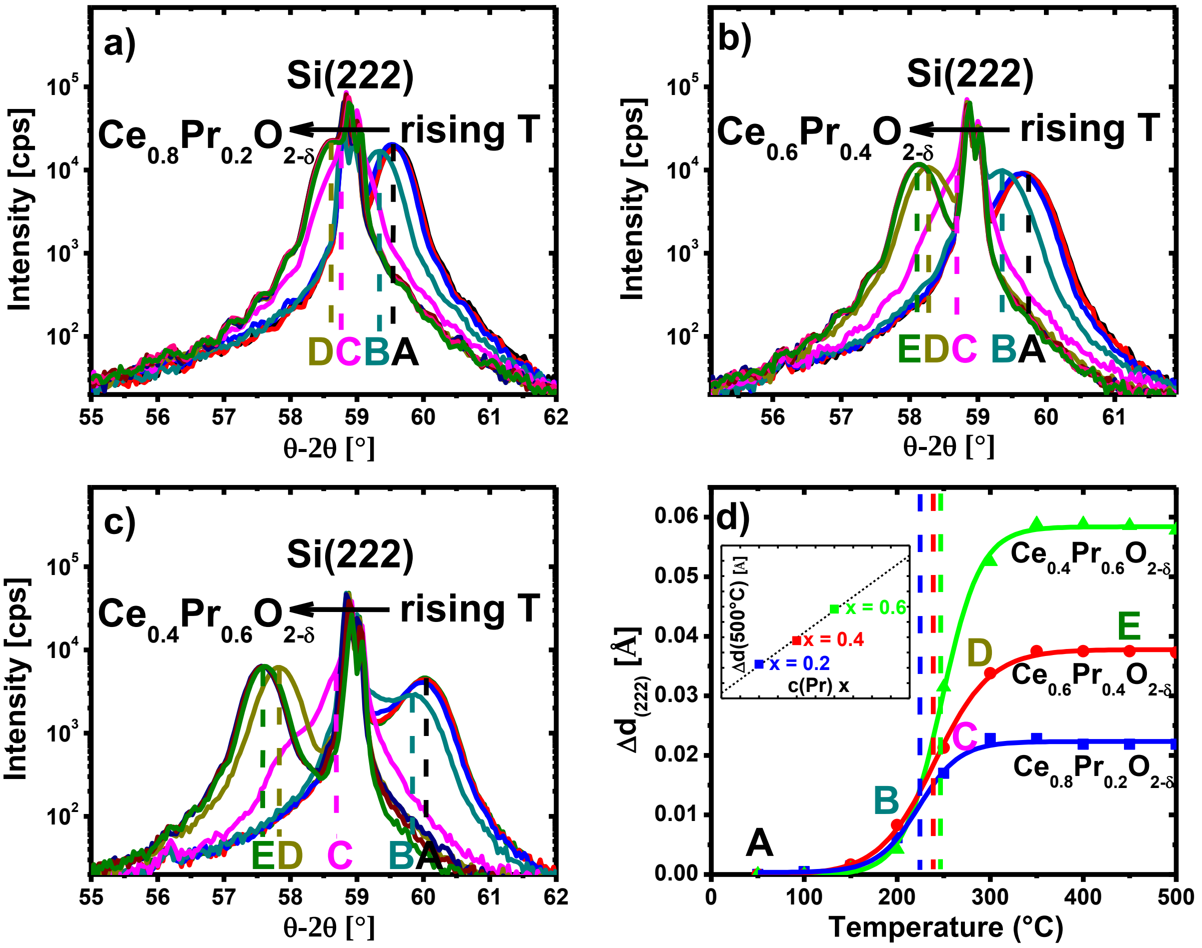

Figure 4.21: Specular θ-2θ scans from 55° to 62° of (a) $Ce_{0.8}Pr_{0.2}O_{2-\delta}(111)$ (b) $Ce_{0.6}Pr_{0.4}O_{2-\delta}(111)$ and (c) $Ce_{0.4}Pr_{0.6}O_{2-\delta}(111)$. (d) $\Delta d_{(222)}$ plotted versus annealing temperature with inset showing $\Delta d_{(222)}$(500°C) in dependency on c(Pr).[184]

out-of-plane lattice spacing $d_{(222)}$ by Pr^{3+} and/or Ce^{3+} formation. Furthermore, the higher the Pr concentration the higher the shift, which is demonstrated in Fig. 4.21d. Here, the lattice spacing variation $\Delta d_{(222)}$ is plotted versus the annealing temperature and fitted to estimate the lattice reconstruction temperature T_r (dashed lines). T_r is found to increase ($T_r^{x=0.2} < T_r^{x=0.4} < T_r^{x=0.6}$) with increasing Pr concentration and is thus in line with the TPD result for the atmosphere exposed samples (T_{CO2}). As already indicated, the final lattice spacing expansion $\Delta d_{(222)}$ after the 500°C annealing step is also linearly increasing with the Pr doping concentration as shown in the inset of Fig. 4.21d ($\Delta d_{(222)}^{x=0.2} = 0.022Å$; $\Delta d_{(222)}^{x=0.4} = 0.038Å$; $\Delta d_{(222)}^{x=0.6} = 0.058Å$). This indicates a dependency from the Pr^{4+} to Pr^{3+} reduction process. To which extent Ce^{4+} contributes to the oxygen release and the lattice reconstruction is not yet clear.

4.3.3 Valence state variation

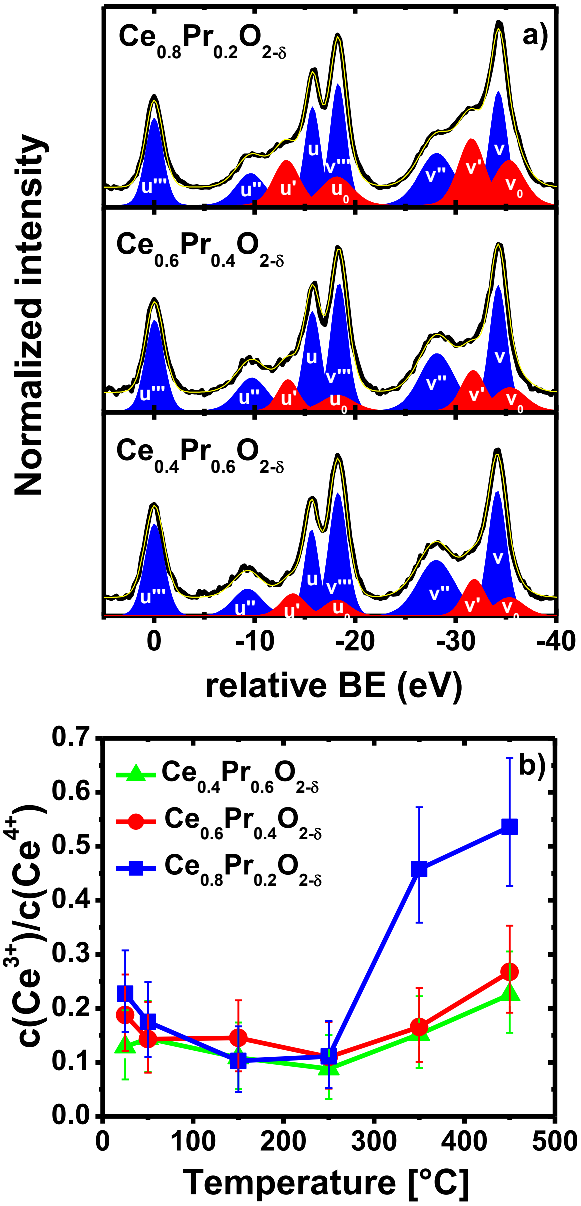

Figure 4.22: (a) XPS Ce3*d* core level spectra of $Ce_{1-x}Pr_xO_{2-\delta}(111)/Si(111)$ samples (x = 0.2, 0.4, 0.6) at 450°C. (b) Temperature dependent $c(Ce^{3+})/c(Ce^{4+})$ ratio variation.[180]

As previously discussed, the oxygen release is related to a lattice expansion, which is attributed to the reduction of the rare earth cations Pr^{4+}/Pr^{3+} and/or Ce^{4+}/Ce^{3+}. Since it is found by Allahgholi that the complete reduction to Pr^{3+} in such $Ce_{1-x}Pr_xO_2$ mixed oxides proceeds at much lower temperatures than for Ce^{3+} ($T_{Pr3+}^{x=0.7} = 390°C$; $T_{Ce3+}^{x=0.7} = 880°C$)[174] and a clear linear dependency on the Pr concentration of the oxygen release and lattice rearrangement is demonstrated in the previous chapter, it is evident that the OSC is mainly driven by the Pr^{4+}/Pr^{3+} redox system. However, as indicated by the TPD results, the reaction is supported by the catalytic activity of the Ce^{4+}/Ce^{3+} redox system. Thus, XPS investigations of the Ce3*d* region after the final annealing step of 450°C are presented in Fig. 4.22a to evaluate the influence of Ce^{3+} formation to the reaction process. As known, the multitude of 10 peaks is denoted and fitted according to Tab. 4.2,[175] with u''', u'', u, v''', v'', v (blue curves) for the Ce^{4+} cations and with u', u_0, v', v_0 (red curves) for the Ce^{3+} cations. A Shirley background was subtracted before. Furthermore, the signals are normalized and referred to the u''' peak intensity and position, respectively. Thus, the Ce^{3+} concentration can be approximately calculated by:

$$c(Ce^{3+}) = \frac{u' + u_0 + v' + v_0}{\sum_i (u^i + v^i)} \qquad and \qquad c(Ce^{4+}) = \frac{u + u'' + u''' + v + v'' + v'''}{\sum_i (u^i + v^i)} \qquad \mathbf{(4.2)}$$

However, due to the overlapping multiplett and charge transfer satellites, this method exhibits a quite large error. It is noted that the determination of the valence state concentration is more precise by factor analysis.[178, 191, 192] Thus, in the following the temperature dependent behavior (Fig. 4.22b) of the c(Ce^{3+})/c(Ce^{4+}) ratio is described qualitatively. At first, all samples show a similar ratio and likewise a similar drop of the ratio up to 250°C. This can be attributed to carbonaceous surface species with a Ce^{3+} valence state. Following, a reduction to Ce^{3+} occurs starting at 350°C. Thus, it seems that the Ce^{4+} starts to reduce not until the oxygen release and the lattice reconstruction proceeded (200°C – 300°C). Even up to 450°C the Ce^{4+} concentration stays dominant since the ratio is far below 1, demonstrating the inferior role of the Ce^{4+}/Ce^{3+} redox system.

Interestingly, the Ce^{3+} concentration at 450°C is higher for the Pr poor samples, which seems to be surprising since a promoting effect by the Pr doping is expected. However, the PrO_2 component may act as oxygen buffer and excess electrons from the reduction process prefer to be located at the Pr^{4+} ion forming Pr^{3+}.[188] Thus, Pr poor mixtures run faster into an oxygen insufficiency leading to a more pronounced reduction of Ce^{4+}.

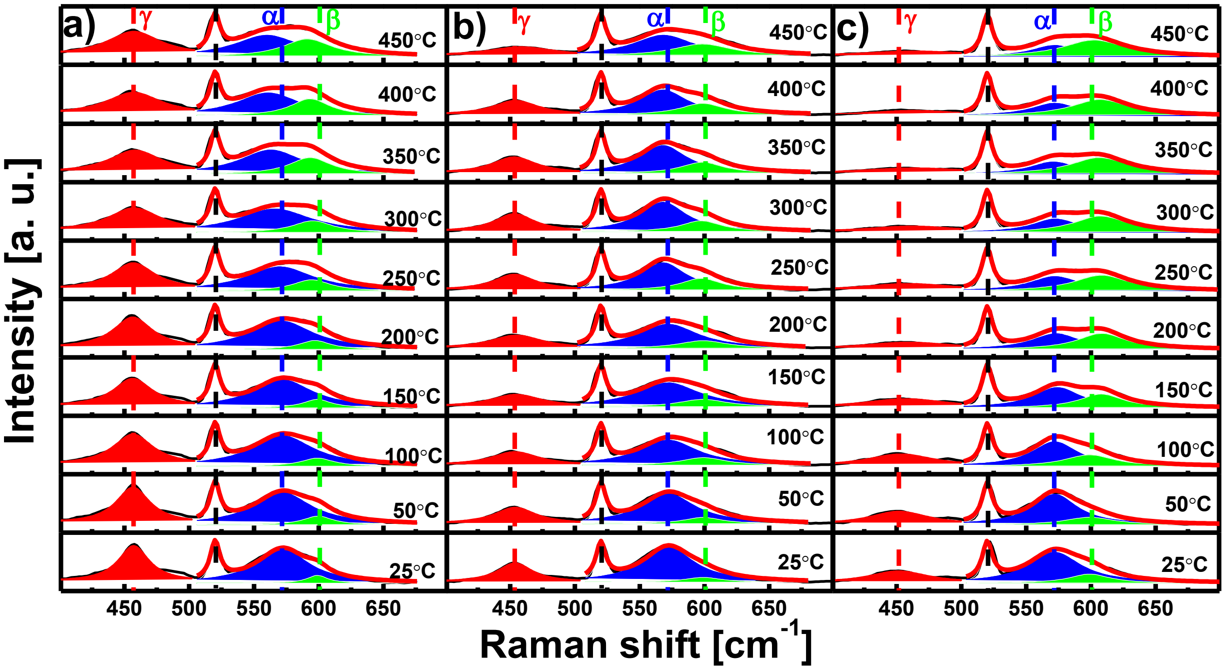

Figure 4.23: Raman spectra of (a) $Ce_{0.8}Pr_{0.2}O_{2-\delta}$(111)/Si(111) (b) $Ce_{0.6}Pr_{0.4}O_{2-\delta}$(111)/Si(111) and (c) $Ce_{0.4}Pr_{0.6}O_{2-\delta}$(111)/Si(111) after stepwise annealing.[184]

4.3.4 Microscopic defect formation

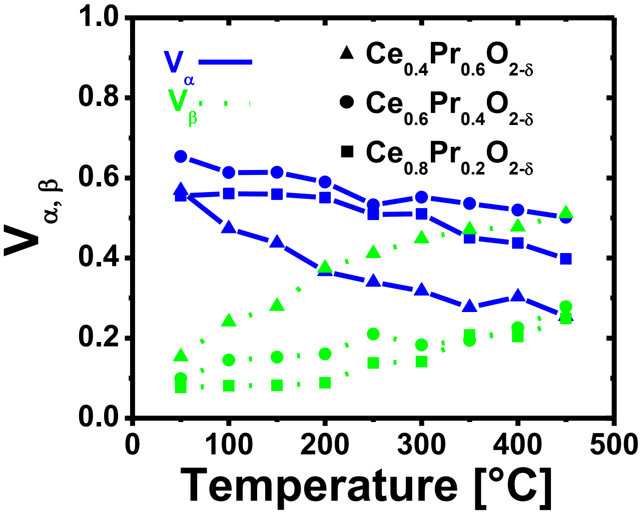

Figure 4.24: Temperature dependent evolution of the defect related relative signal intensities V_α (full blue lines) and V_β (dotted green lines) for $Ce_{0.8}Pr_{0.2}O_{2-\delta}$ (full squares), $Ce_{0.6}Pr_{0.4}O_{2-\delta}$ (full circles) and $Ce_{0.4}Pr_{0.6}O_{2-\delta}$(111) (full triangles).[180]

Since the release of oxygen leads to a reconstruction of the lattice by the valence state change this will certainly also cause a structural change on a microscopic scale. This was investigated by Raman spectroscopy as done in chapter 4.2.2 for a stoichiometry dependent study. In Fig. 4.23 the temperature dependent (RT to 450°C) Raman spectra of $Ce_{0.8}Pr_{0.2}O_{2-\delta}(111)$ (Fig. 4.23a), $Ce_{0.6}Pr_{0.4}O_{2-\delta}(111)$ (Fig. 4.23b) and $Ce_{0.4}Pr_{0.6}O_{2-\delta}(111)$ (Fig. 4.23c) are referred to the Si peak position and normalized to the Si peak intensity. Additionally, the peaks γ ($M^{4+}O_8$) at 460 cm^{-1}, α ($V_O^{\bullet\bullet}O_6$) at 570 cm^{-1} and β ($M^{3+}O_8$) at 600 cm^{-1} are denoted. The temperature dependent evolution of the relative signals V_α and V_β show a similar tendency (Fig. 4.24), as observed for the doping by Pr^{3+} (Fig 4.19c). Namely, V_α is decreasing while V_β is increasing. This is not surprising since the doping as well as the reduction process leads to an increase of the M^{3+} concentration. Thus, the M^{3+} cations like to cluster in MO_8 type complexes up to 450°C, as it was also observed for Gd-doped CeO_2 in this temperature range.[193] Furthermore, Tang *et al.*[188] calculated for $Ce_{1-x}Pr_xO_{2-\delta}$ solid solutions, that for the $V_O^{\bullet\bullet}$ the second nearest-neighboring oxygen coordination sphere is energetically favored and thus creates a $M^{3+}O_8$ complex configuration, resulting in an increase of V_β.

4.3.5 Conclusion

The presented temperature dependent study on the reduction behavior of single crystalline, mixed ternary $Ce_{1-x}Pr_xO_{2-\delta}$ thin films as a function of stoichiometry x (x = 0.2, 0.4, 0.6) indicate that it became possible to engineer the catalytic properties (OSC and oxidative activity) of such heterostructures. It is suggested that the oxygen storage effect is attributed to the Pr^{4+}/Pr^{3+} redox system and the hydrocarbon oxidative ability to the Ce^{4+}/Ce^{3+} redox system. This redox mechanism can be illustrated by the sketch shown in Fig. 4.25 and is corroborated by the results from TPD, XRD, XPS and Raman spectroscopy. The oxygen release from in-situ plasma-oxidized ("clean surfaces") and ex-situ atmosphere exposed ("hydrocarbon covered surfaces") samples was investigated by TPD.

1) With increasing Pr concentration the plasma-oxidized samples release O_2 earlier ($T_{O2}^{x=0.2} > T_{O2}^{x=0.4} > T_{O2}^{x=0.6} > T_{O2}^{x=1.0}$), which is attributed to the higher oxygen exchange activity by Pr^{4+}/Pr^{3+}(thick arrow from blue to purple in Fig. 4.25).[38]
2) The atmosphere exposed samples release CO_2 later ($T_{CO2}^{x=0.2} < T_{CO2}^{x=0.4} < T_{CO2}^{x=0.6} < T_{CO2}^{x=1.0}$), which is probably related to the kinetically favoured reaction path (hydrocarbon oxidation and CO_2 desorption) and the superior oxidative ability of ceria (thick arrow of the oxidation process in Fig. 4.25).[1]

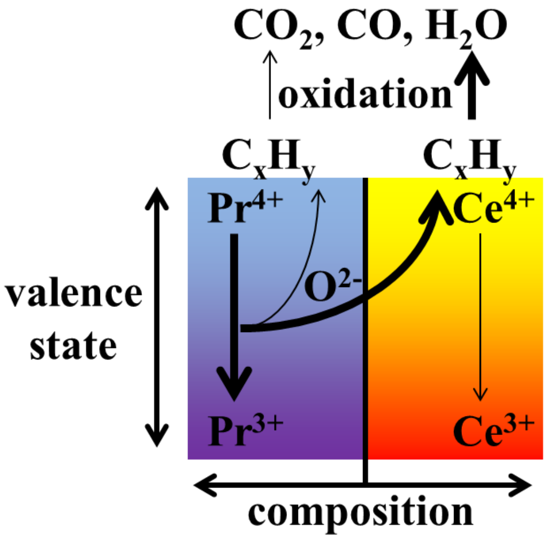

Figure 4.25: Model of the redox process of $Ce_{1-x}Pr_xO_{2-\delta}(111)/Si(111)$ samples.[180]

Considering the linear increasing behaviour of the integral O_2 signal (TPD) and of the total lattice spacing difference (XRD) in dependence on the Pr concentration, the OSC is mainly supported by the Pr doping. Indeed, the superior role of the Pr^{3+}/Pr^{4+} redox system is corroborated by XPS measurements, which do not show any significant Ce^{3+}/Ce^{4+} valence state change (thin arrow of valence state change in Fig. 4.25) in the temperature range from 200°C-300°C. Since the oxidation process is driven by Ce^{4+}/Ce^{3+} variation and the Pr^{3+}/Pr^{4+} is responsible for the oxygen supply, an oxygen transport within the film is suggested (thick arrow of O^{2-} transport in Fig. 4.25). In consequence, it is found by Raman spectroscopy that microscopic $M^{3+}O_8$ defect formation occurs. However, the oxygen deficiency seems not to be reflected by the Raman signal of $V_O^{\bullet\bullet}O_6$ defect types. A lattice distortion in favor of the bixbyite structure might be the reason for this observation as discussed in chapter 4.2.2.

Chapter 5

Summary & Outlook

5.1 Summary

Recalling the main objective of this PhD thesis, the idea was to bring together microelectronics and catalysis on a fundamental physical and chemical level. To achieve that goal, binary and ternary $Ce_{1-x}Pr_xO_{2-\delta}$ thin films were grown on a Si(111) substrate in order to allocate high quality samples to study the structural and electronic properties. Fig. 5.1 demonstrates this basic context in a schematic way. From the foregoing result chapters related to single crystalline and epitaxial, binary and ternary $Ce_{1-x}Pr_xO_{2-\delta}$ (x = 0-1) heterostructures, three main results are given:

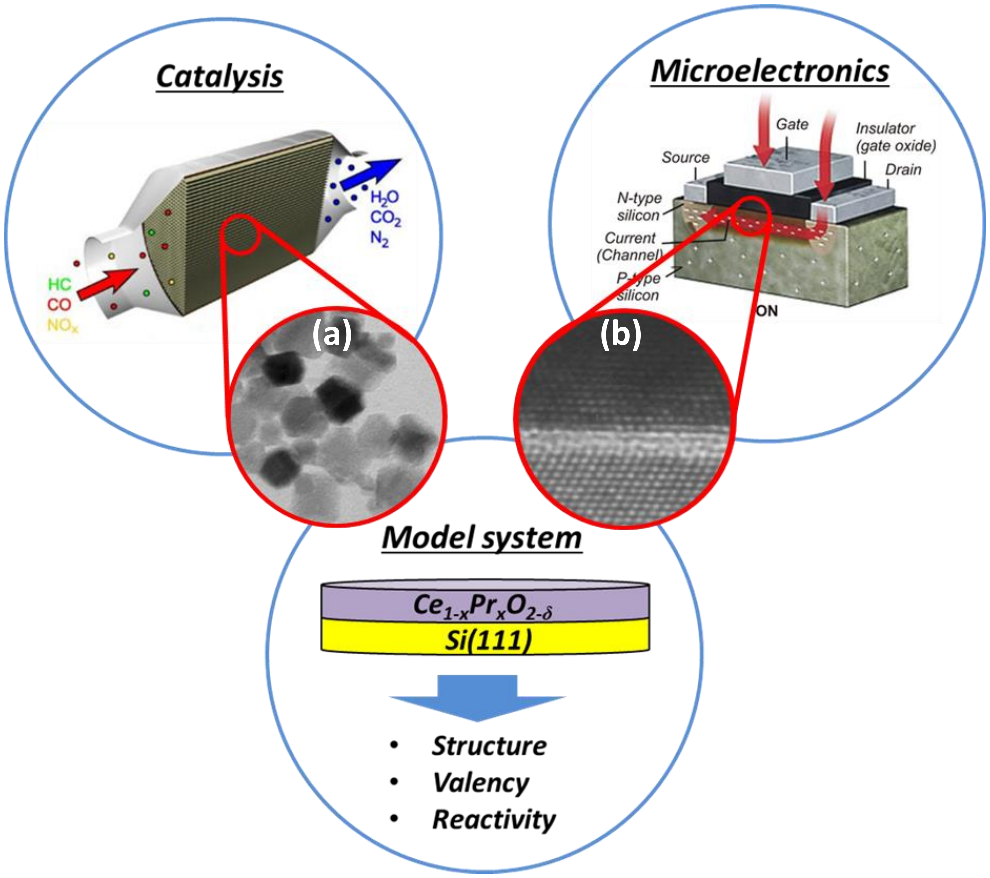

Figure 5.1: Schematic presentation that “Microelectronics meets Catalysis” on a basic materials science research level (TEM images of (a) CeO_2 nanopowder and (b) $CeO_2(111)$/Si(111) interface are presented). Model systems can help to give insights on structure, valency and reactivity to understand and tailor these complex functional materials.[105, 194]

I. ***Implications on structure:*** It became possible to in-situ grow epitaxial, twin-free, exclusively type-B oriented CeO$_2(111)$ on Si(111) in the IHP MBE oxide chamber by using an ultra-thin hex-Pr$_2$O$_3(0001)$ buffer layer, finally verified by SR-GIXRD (Fig. 5.2a). This is attributed to the crystallographic (continuation of the oxygen sub-lattice) and electronic (conservation of the semiconducting behavior) interplay at the interface. Especially, a stabilization of Pr^{4+} cations at the interface is predicted by a theoretical model (Fig. 5.2b and c), but not yet proven by experiment. Such an epitaxy stabilized Pr^{4+} interface layer might exhibit interesting electronic properties.

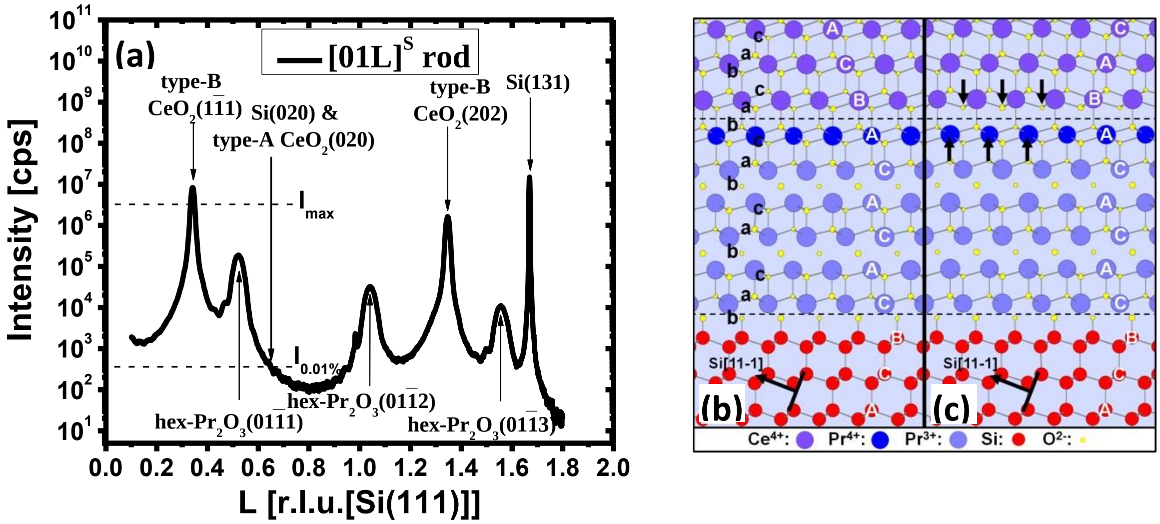

Figure 5.2: (a) Stacking twin analyzis by SR-GIXRD scan of CeO$_2$(111)/hex-Pr$_2$O$_3$(0001)/Si(111) showing the epitaxial, twin-free, exclusive type-B orientation.[154] (b) Stacking configuration models with a Pr^{4+} monolayer of type-B CeO$_2$(111)/hex-Pr$_2$O$_3$(0001)/Si(111) indicating the oxygen sub-lattice continuation and (c) type-A CeO$_2$(111)/hex-Pr$_2$O$_3$(0001)/Si(111) indicating an oxygen sub-lattice stacking fault at the interface.[154]

II. ***Implications on valency:*** Furthermore, the growth of epitaxial ternary Ce$_{1-x}$Pr$_x$O$_{2-\delta}$ mixed oxides became possible on such a hex-Pr$_2$O$_3(0001)$ buffer layer on Si(111). In dependence on the Pr content, it turned out that truly mixed alloys with Pr^{3+} incorporation into the CeO$_2$ fluorite crystal matrix and Ce^{3+} incorporation into the hex-Pr$_2$O$_3$ matrix were achieved (Fig. 5.3a-c). However, Pr^{4+} stabilization within such mixed oxides was not yet achieved in this UHV study but is certainly possible by plasma-oxidation.

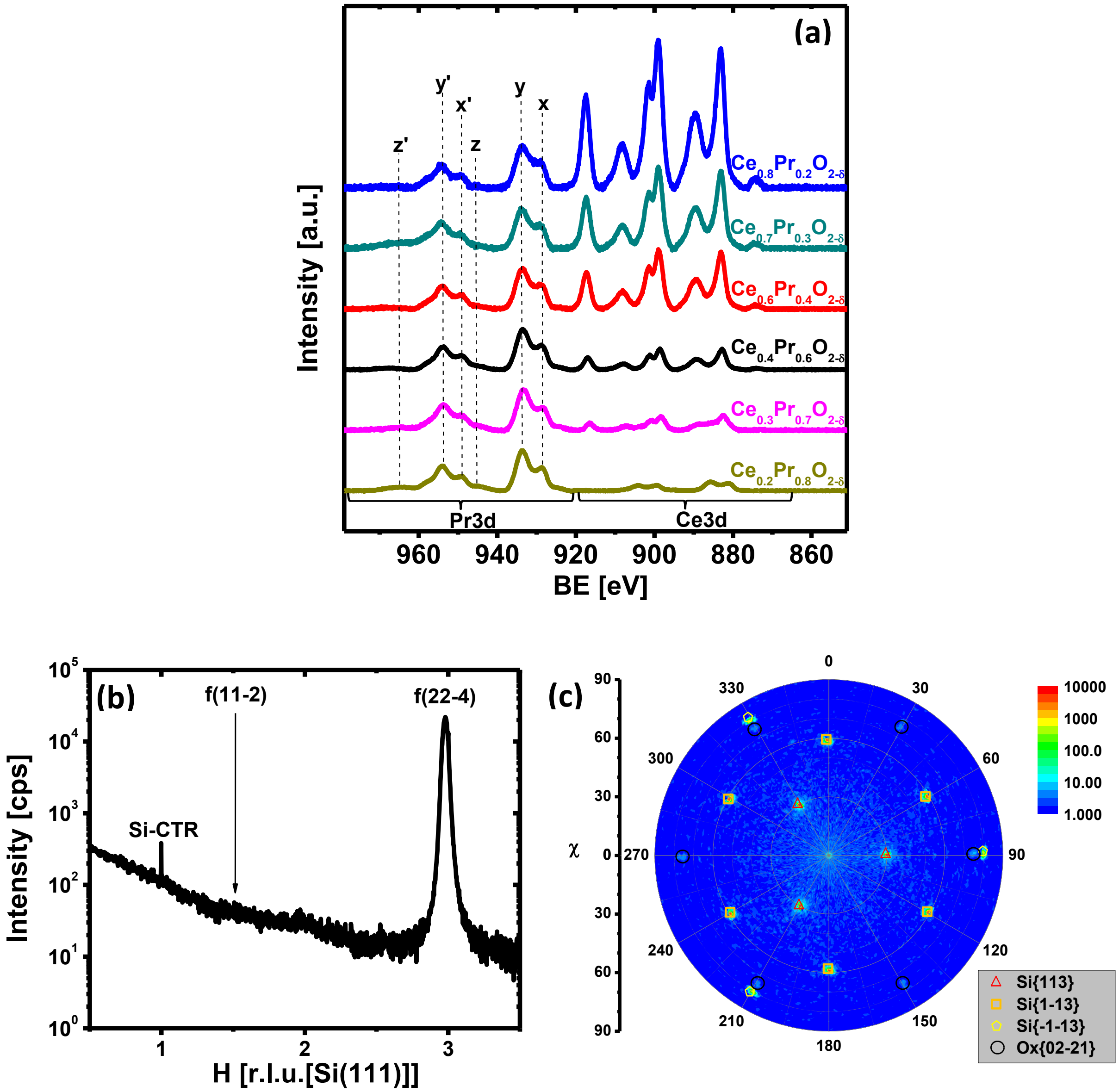

Figure 5.3: (a) XPS Pr and Ce3*d* core level spectra of $Ce_{1-x}Pr_xO_{2-\delta}$ showing Pr^{3+} valence state for all stoichiometries and Ce^{3+} content for Pr rich samples. (b) SR-GIXRD scan indicating the exclusively cubic related fluorite crystal structure of $Ce_{0.7}Pr_{0.3}O_{2-\delta}$ and (c) Pole figure of $Ce_{0.2}Pr_{0.8}O_{2-\delta}$/Si(111) indicating a hexagonal crystal structure.[173]

III. ***<u>Implications on reactivity:</u>*** The reduction behavior of $Ce_{1-x}Pr_xO_{2-\delta}$ mixed oxides was investigated, revealing that the OSC can be tailored by Pr doping due to the Pr^{4+}/Pr^{3+} redox system (inset Fig. 5.4a,b). It was found that the hydrocarbon oxidation process is however mainly triggered by the Ce^{4+}/Ce^{3+} redox system (Fig. 5.4c). In other words, Pr-doped CeO_2 allows tuning catalytic properties in order to increase the oxidation properties and to lower the temperature of future catalytic oxidation reactions.

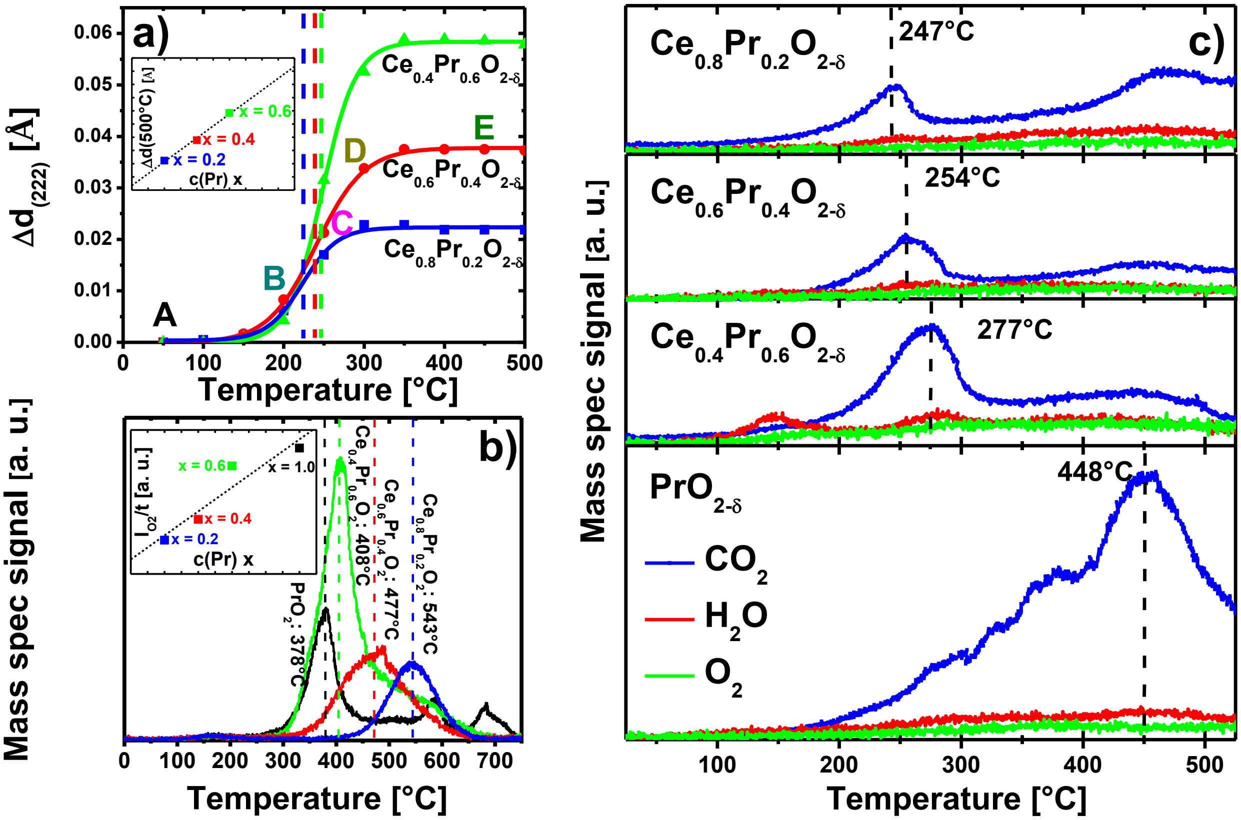

Figure 5.4: (a) Temperature dependent variation of the lattice spacing $d_{(222)}$ for $Ce_{1-x}Pr_xO_{2-\delta}(111)$ (x = 0.2, 0.4, 0.6) and (b) O_2 TPD spectra of in-situ oxygen plasma treated samples. Insets of (a) and (b) represent the increased oxygen storage capacity with higher Pr content. (c) CO_2 TPD spectra of samples treated ex-situ with molecular oxygen indicating lower oxidation temperatures with increasing Ce content.

As introduced in the beginning of the thesis, these observations of the physical and chemical properties are based on the following microscopic origin: Ceria and praseodymia appear in similar crystal structures (fluorite, bixbyite, hexagonal phase) and valence states (M^{4+}/M^{3+}) but their preference is different within these options. While Ceria favors the cubic fluorite structure, praseodymia favors the hexagonal structure when grown under UHV conditions on Si(111). Furthermore, they exhibit an opposite behaving redox systems of Pr^{4+}/Pr^{3+} and Ce^{4+}/Ce^{3+}, with Pr (Ce) preferring the 3+ (4+) valence state under normal reaction conditions.

5.2 Outlook

The three implications on structure, valency and reactivity pointed out in this PhD thesis give rise to more detailed fundamental and application related investigations. Fig. 5.5 demonstrates that microelectronics and catalysis may profit from such structural and electronic studies of this binary and ternary $Ce_{1-x}Pr_xO_{2-\delta}$/Si(111) thin films in terms of future applications, e.g. in model catalysis and spintronics.

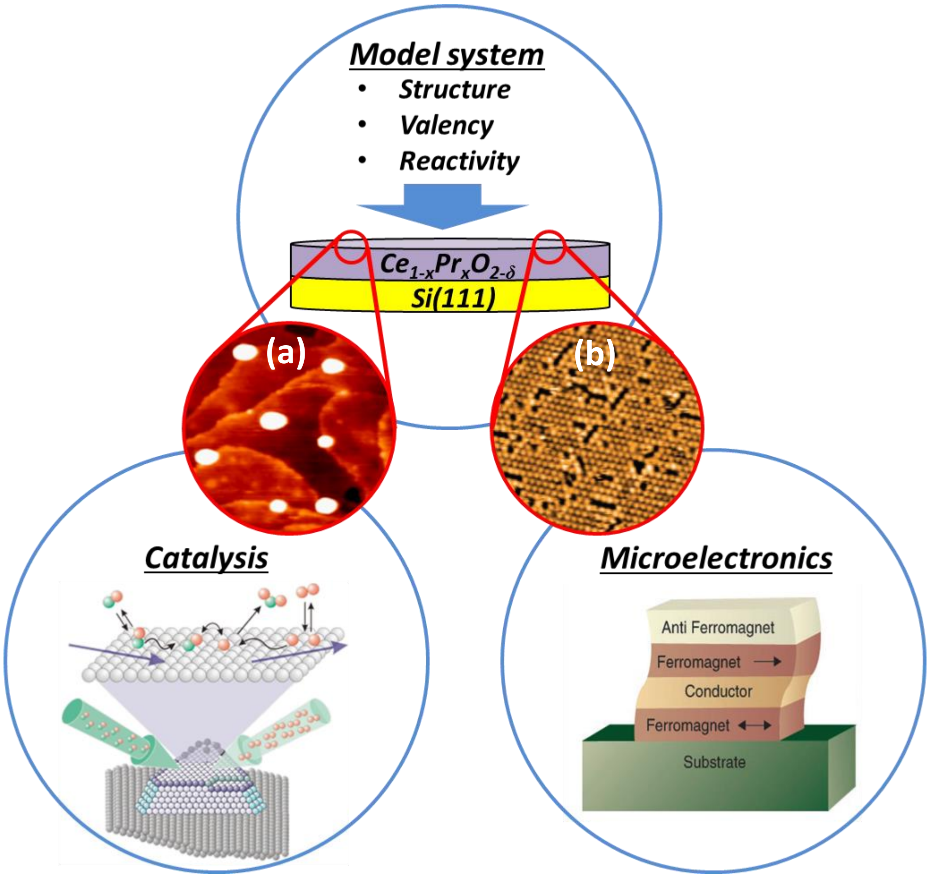

Figure 5.5: Schematic presentation how $Ce_{1-x}Pr_xO_{2-\delta}(111)$/Si(111) systems may be investigated for future applications in microelectronics and catalysis (STM images of (a) $CeO_2(111)$ surface decorated with Pd nanoparticles (b) $CeO_2(111)$ surface with oxygen vancies).[195-197]

I. ***Reactivity properties for catalysis:*** Related to catalytic experiments, the buried praseodymia film in CeO_2/Pr_2O_3 bilayer structures might be loaded with oxygen through the CeO_2 top layer in order to function as oxygen buffer reservoir (increased OSC) for oxidative reactions similar to the function of Pr in the $Ce_{1-x}Pr_xO_{2-\delta}$ mixed oxide films. Since up to know only undefined carbonaceous contaminations were oxidized on $Ce_{1-x}Pr_xO_{2-\delta}$ films, it is also necessary to evaluate the oxidative reactivity in dependence of the stoichiometry under more defined conditions, e.g. plasma oxidized samples, certain ambient atmosphere (simple gases as CO, H_2O, O_2), exposure time etc. According to chapter 2.3.2, further investigations should be devoted to a step wise increase of the complexity of this model catalytic system in order to bridge the materials and pressure gap, as done for Pd clusters on a Fe_3O_4/Pt(111) thin film support (see Fig. 5.6).[198] To gain a deeper understanding of the reaction mechanisms and thus evaluate the potential of this approach with respect to existing solutions in catalysis, e.g. metal-support interaction, poisoning effects, size and structure dependency might be investigated by the model catalysis approach.

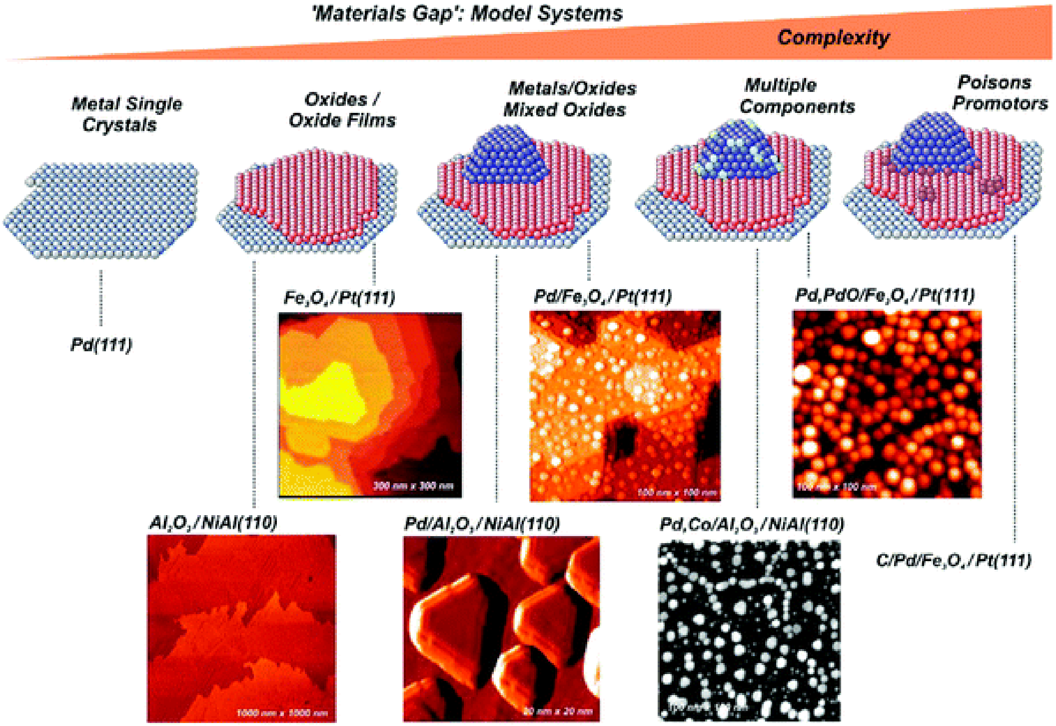

Figure 5.6: Planar supported model catalysts of increasing complexity (e.g. Pd on Fe_3O_4/Pt(111)).[198]

II. ***<u>Electronic properties for microelectronics:</u>*** Investigations of the electronic characteristics at the CeO_2/Pr_2O_3 heterostructures interface by electron energy loss spectroscopy (EELS) would be of interest to evaluate potential Pr^{4+} formation. Related to this phenomenon, electrical measurements of such heterostructures could be performed in order to characterize deviations of the insulating behavior, which is related to the oxygen excess ($M_2O_{3+\delta}$) and deficiency ($MO_{2-\delta}$) accompanied by a semiconducting behavior. Potentially, oxidic pn-junctions may result from these investigations. Another interesting property of $Ce_{1-x}Pr_xO_{2-\delta}$ mixed oxides, recently highlighted in several publications, is room temperature ferromagnetism (RTFM) in diluted magnetic oxides (DMO).[199, 200] For the widely accepted F-center exchange (FCE) mechanism, the oxygen vacancies seem to play a major role as mediating agent (F-center) between the paramagnetic Ce^{3+}, Pr^{3+} and Pr^{4+} cations within the diamagnetic CeO_2 matrix (Fig. 5.7a). Three different centers can be categorized depending on how many electrons are trapped in the hydrogenic orbit (r_H) of the $V_O^{\bullet\bullet}$ (Fig. 5.7b-c): (i) F^{2+}-center with no trapped electron. Both free electrons are localized at the cations forming Ce^{3+}/Pr^{3+}. (ii) F^{+}-center with one trapped electron mediating the FM interaction. (iii) F^{0}-center with 2 trapped electrons mediating weak antiferromagnetism.[199] It was shown that the saturation magnetization is two orders of magnitude higher (1.8 emu/g) than usually measured in undoped/doped CeO_2 nanopowders and that the effect correlates with the microscopic defect structure, namely the oxygen vacancies within the epitaxial $Ce_{1-x}Pr_xO_{2-\delta}$ thin films.[179]

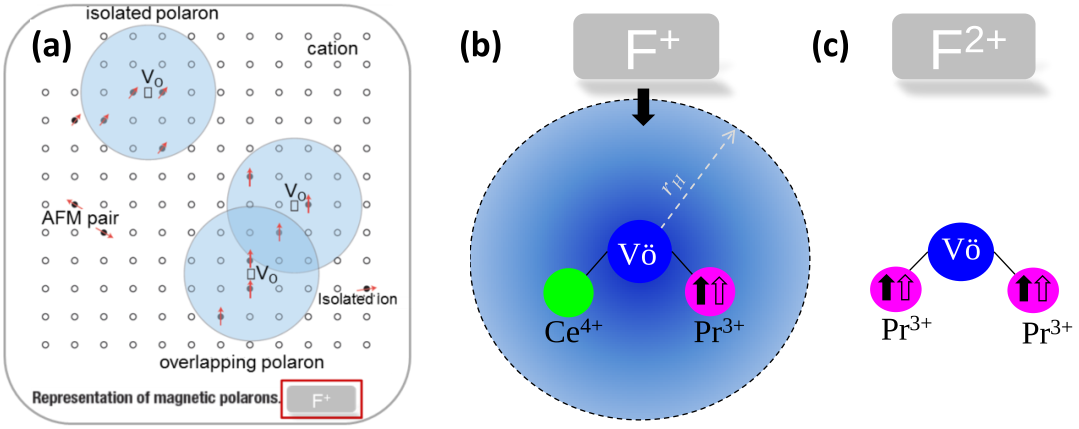

Figure 5.7: (a) Representation of a magnetic polaron coupling paramagnetic cations by a F^{+}-center.[200] Two defect complexes creating (b) a F^{+}-center and (c) a F^{2+}center.[179]

Chapter 6

Scientific Visibility

6.1 Publications in peer-reviewed Journals

1. M. H. Zoellner, J. Dabrowski, P. Zaumseil, A. Giussani, M. A. Schubert, G. Lupina, H. Wilkens, J. Wollschläger, M. Reichling, M. Bäumer and T. Schroeder, *Stacking behavior of twin-free type-B oriented* CeO_2*(111) films on hexagonal*Pr_2O_3*(0001)/Si(111) systems,* Phys. Rev. B **85**, 035302 (2012).

2. M. H. Zoellner, P. Zaumseil, H. Wilkens, S. Gevers, J. Wollschläger, M. Bäumer, Y.-H. Xie, G. Niu, and T. Schroeder *Stoichiometry-structure correlation of epitaxial* $Ce_{1-x}Pr_xO_{2-\delta}$ *(x = 0-1) thin films on Si(111),* J. Cryst. Growth **355**, 159 (2012).

3. M. H. Zoellner, G. Niu, J.-H. Jhang, A. Schaefer, P. Zaumseil, M. Bäumer and T. Schroeder, *Temperature dependent reduction of epitaxial* $Ce_{1-x}Pr_xO_{2-\delta}$ *(x = 0-1) thin films on Si(111): A combined TPD, XRD, XPS and Raman study*, J. Phys. Chem. C **117**, 24851 (2013).

4. H. H. Pieper, C. Derks, M. H. Zoellner, R. Olbrich, L. Tröger, T. Schroeder, M. Neumann, and M. Reichling, *Morphology and nanostructure of* CeO_2*(111) surfaces of single crystals and Si(111) supported ceria films,* Phys. Chem. Chem. Phys. **14**, 15361 (2012).

5. G. Niu, P. Zaumseil, M. A. Schubert, M. H. Zoellner, J. Dabrowski, and T. Schroeder, *Lattice-matched epitaxial* $Pr_xY_{2-x}O_3$ *films on SrO-passivated Si(001): Interface engineering and crystallography tailoring*, Appl. Phys. Lett. **102**, 011906 (2013).

6. G. Niu, M. H. Zoellner, P. Zaumseil, A. Pouliopoulos, F. d'Acapito, T. Schroeder, and F. Boscherini, *X-ray diffraction and extended X-ray absorption fine structure study of epitaxial mixed ternary bixbyite* $Pr_xY_{2-x}O_3$ *(x = 0-2) films on Si(111)*, J. Appl. Phys. **113**, 043504 (2013).

7. H. Wilkens, O. Schuckmann, R. Oelke, S. Gevers, A. Schaefer, M. Bäumer, M. H. Zoellner, T. Schroeder, and J. Wollschlaeger, *Stabilization of the ceria ι–phase (Ce_7O_{12}) surface on Si(111)*, Appl. Phys. Lett. **102**, 111602 (2013).

8. H. Wilkens, J. Rodewald, S. Gevers, M. H. Zoellner, T. Schroeder, and J. Wollschläger, *Surface morphology of ultrathin hex-Pr_2O_3 films on Si(111)*, J. Phys. D: **46**, 285306 (2013).

9. H. Wilkens, O. Schuckmann, R. Oelke, S. Gevers, M. Reichling, A. Schaefer, M. Bäumer, M. H. Zoellner, N. Gang, T. Schroeder and J. Wollschläger, *Structural transitions of epitaxial ceria films on Si(111)*, Phys. Chem. Chem. Phys. **15**, 18589 (2013).

10. H. Wilkens, S. Gevers, S. Röhe, A. Schaefer, M. Bäumer, M. H. Zoellner, T. Schroeder, and J. Wollschläger, *Structural changes of ultra thin cub-PrO_2(111)/Si(111) films due to thermally induced oxygen desorption,* submitted to J. Phys. Chem. C. 2013.

11. R. Olbrich, H.H. Pieper, R. Oelke, H. Wilkens, J. Wollschläger, M. H. Zoellner, T. Schroeder and M. Reichling, *Transforming kinetically determined nanostructures on ceria into a thermodynamic equilibrium configuration*, submitted to Appl. Phys. Lett. 2013.

12. G. Niu, E. Hildebrandt, M. A. Schubert, F. Boscherini, M. H. Zoellner, L. Alff, D. Walczyk, P. Zaumseil, I. Costina, and T. Schroeder, *Oxygen vacancy induced room temperature ferromagnetism in Pr-doped CeO_2 thin films on silicon*, to be submitted to Adv. Mater. 2013.

6.2 Patent

1. G. Lippert, O. Seifarth, G. Lupina, H. Thieme, M. H. Zoellner, *Integration von hochbeweglichem Graphen,* AZ: 10 167 703.7 EP-Patentanmeldung (Erstanmeldung 2010), US-Patentanmeldung (2011) AZ: 13/135,313.

6.3 Presentation at conferences

1. M. H. Zoellner, G. Lippert, O. Seifarth, G. Lupina, and T. Schroeder, *Graphene Growth on Catalytic Insulator*, Graphene Electronics - Material, Physics and Devices, August 2010, Germany.

2. M. H. Zoellner, J. Dabrowski, P. Zaumseil, A. Giussani, M. A. Schubert, J. Wollschläger, M. Reichling, M. Bäumer, and T. Schroeder, *Structures Investigation of Heteroepitaxial Type-B Oriented $CeO_2(111)$ on cubic- and hexagonal-$Pr_2O_3/Si(111)$ Supports*, DPG spring meeting, March 2011, Germany.

3. M. H. Zoellner, H. Wilkens, P. Zaumseil, M. Bäumer, M. Reichling, J. Wollschläger and T. Schroeder, Studying the Structure - *Stoichiometry Relationship of Mixed $Ce_{1-x}Pr_xO_{2-\delta}$ (x = 0-1) Oxide Catalysts on Si (111) investigated by XRD*, 8th Autumn School on X-Ray Scattering from Surfaces and Thin Layers, October 2011, Slovakia.

4. M. H. Zoellner, H. Wilkens, P. Zaumseil, M. Bäumer, M. Reichling, J. Wollschläger and T. Schroeder, *Structure - Stoichiometry Relationship of Mixed $Ce_{1-x}Pr_xO_{2-\delta}$ (x = 0-1) Oxides on Si(111)*, DPG spring meeting, March 2012, Germany.

5. M. H. Zoellner, G. Lupina, G. Lippert, J. Dabrowski and T. Schroeder, *Graphene Growth on Insulators*, Workshop des Leibniz-Verbundes Nanotechnologie, January 2012, Germany.

6. M. H. Zoellner, G. Chahine, M.-I. Richard, P. Zaumseil, P. Storck, T. U. Schülli, and T. Schroeder, *Influence of Chemo-Mechanical Planarization on the Spatial Lattice tilt Distribution in SiGe Buffer Layers Investigated by Micro-focused X-ray Diffraction Mapping*, JSPS Core-to-Core Program Workshop "Atomically Controlled Processing for Ultralarge Scale Integration", October 2013, Germany.

Chapter 7

Bibliography

1 M. P. Rosynek and N. Imanaka, Catal. Rev.-Sci. Eng. **16**, 111 (1977).
2 M. Fanciulli and G. Scarel, *Rare Earth Oxide Thin Films: Growth, Characterization and Applications* (Springer-Verlag, Berlin, 2007).
3 T. Schroeder, A. Giussani, J. Dabrowski, P. Zaumseil, H.-J. Müssig, O. Seifarth, and P. Storck, Phys. Status Solidi C **6**, 653 (2009).
4 G. Adachi and N. Imanaka, Chem. Rev. **98**, 1479 (1998).
5 A. Trovarelli, *Catalysis by Ceria and Related Materials* (Imperial College Press, London, 2002).
6 D. Kahng and M. Atalla, in *U.S. patents **3102230***, 1960).
7 J. T. Clemens, Bell Labs Technical Journal, 76 (1997).
8 A. Schaefer, PhD thesis, Universität Bremen, 2010.
9 M. Schulz, Nature **399**, 729 (1999).
10 G. D. Wilk, R. M. Wallace, and J. M. Anthony, J. Appl. Phys. **89**, 5243 (2001).
11 J. Robertson, J. Vac. Sci. Technol. B **18**, 1785 (2000).
12 G. Niu, PhD thesis, Ecole Centrale de Lyon, 2010.
13 M. Fanciulli and G. Scarel, *Rare Earth Oxide Thin Films: Growth, Characterization and Applications* (Springer-Verlag, Berlin, 2007).
14 D. P. Norton, Mat. Sci. Eng. R **43**, 139 (2004).
15 K. J. Hubbard and D. G. Schlom, J. Mater. Res. **11**, 2757 (1996).
16 J. Robertson and C. W. Chen, Appl. Phys. Lett. **74**, 1168 (1999).
17 D. G. Schlom and J. H. Haeni, MRS Bulletin **27**, 198 (2002).
18 R. Chau, S. Datta, M. Doczy, B. Doyle, J. Kavalieros, and M. Metz, IEEE **25**, 408 (2004).
19 J. M. J. Lopes, et al., Microelectron. Eng. **86**, 1646 (2009).
20 O. Seifarth, M. A. Schubert, A. Giussani, D. O. Klenov, D. Schmeißer, and T. Schroeder, J. Appl. Phys. **108**, 103709 (2010).
21 S. Shen, Y. Liu, R. G. Gordon, and L. J. Brillson, Appl. Phys. Lett. **98**, 172902 (2011).
22 A. Giussani, Osnabrück, 2010.
23 A. Giussani, P. Zaumseil, O. Seifarth, P. Storck, and T. Schroeder, New J. Phys. **12**, 093005 (2010).
24 E. J. Tarsa, J. S. Speck, and M. Robinson, Appl. Phys. Lett. **63**, 539 (1993).
25 T. Schroeder, P. Zaumseil, O. Seifarth, A. Giussani, H.-J. Müssig, P. Storck, D. Geiger, H. Lichte, and J. Dabrowski, New J. Phys. **10**, 113004 (2008).
26 T. Schroeder, P. Zaumseil, G. Weidner, G. Lupina, C. Wenger, P. Storck, and H.-J. Müssig, J. Appl. Phys. **98**, 123513 (2005).
27 A. Giussani, et al., J. Appl. Phys. **105**, 033512 (2009).
28 L. Tarnawska, P. Zaumseil, M. A. Schubert, S. Okur, U. Ozgur, H. Morkoc, R. Paszkiewicz, P. Storck, and T. Schroeder, J. Appl. Phys. **111**, 073509 (2012).

29 F. Sanchez, R. Bachelet, P. d. Coux, B. Warot-Fonrose, V. Skumryev, L. Tarnawska, P. Zaumseil, T. Schroeder, and J. Fontcuberta, Appl. Phys. Lett. **99**, 2011 (2011).

30 M. Baerns, A. Behr, A. Brehm, J. Gmehling, H. Hofmann, U. Onken, and A. Renken, *Technische Chemie* (Wiley-VCH Verlag, 2006).

31 J. G. Calvert, J. B. Heywood, R. F. Sawyer, and J. H. Seinfeld, Science **261**, 37 (1993).

32 J. M. Thomas and W. J. Thomas, *Principles and Practice of Heterogeneous Catalysis* (VCH, Weinheim, 1997).

33 O. V. Buyevskaya, D. Wolf, and M. Baerns, Catal. Today **62**, 91 (2000).

34 K. Asami, K. Kusakabe, N. Ashi, and Y. Ohtsuka, Appl. Catal. A: General **156**, 43 (1997).

35 F. L. Normand, J. Barrault, R. Breault, L. Hilaire, and A. Kiennemann, J. Phys. Chem. **95**, 257 (1991).

36 J. Kaspar, P. Fornasiero, and M. Graziani, Catal. Today **50**, 285 (1999).

37 T. Bunluesin, R. J. Gorte, and G. W. Graham, Appl. Catal. B: Environmental **15**, 107 (1998).

38 G. V. Antoshin, K. M. Minachev, and R. V. Dmitriev, Russ. Chem. Bull. **16**, 1793 (1967).

39 J. M. DeBoy and R. F. Hicks, Ind. Eng. Chem. Res. **27**, 1577 (1988).

40 K. Otsuka, T. Ushiyama, and I. Yamanaka, Chem. Lett. **22**, 1517 (1993).

41 K. Otsuka, K. Jinno, and H. Morikawa, Chem. Lett. **14**, 499 (1985).

42 A. M. Maitra, I. Campbell, and R. J. Tyler, Appl. Catal. A: General **85**, 27 (1992).

43 D. J. Discroll, W. Martir, J.-X. Wang, and J. H. Lunsford, J. Am. Chem. Soc. **107**, 58 (1985).

44 K. D. Campbell, H. Zhang, and J. H. Lunsford, J. Phys. Chem. **92**, 751 (1988).

45 Y. Feng, J. Niiranen, and D. Gutman, J. Phys. Chem. **95**, 6558 (1991).

46 Y. Feng, J. Niiranen, and D. Gutman, J. Phys. Chem. **95**, 6564 (1991).

47 Y. Schuurman and C. Mirodatos, Appl. Catal. A: General **151**, 305 (1997).

48 V. R. Choudhary and V. H. Rane, J. Catal. **130**, 411 (1991).

49 V. R. Choudhary and V. H. Rane, J. Catal. **135**, 310 (1992).

50 G. A. Martin and C. Mirodatos, Fuel Process. Technol. **42**, 179 (1995).

51 J. Ito, J.-X. Wang, C.-H. Lin, and J. H. Lunsford, J. Am. Chem. Soc. **107**, 5062 (1985).

52 C. Doornkamp and V. Ponec, J. Mol. Catal. A: Chemical **162**, 19 (2000).

53 P. Mars and D. W. Krevelen, Chem. Eng. Sci. Spec. Suppl. **3**, 41 (1954).

54 H. Over, Y. D. Kim, A. P. Seitsonen, S. Wendt, E. Lundgren, M. Schmid, P. Varga, A. Morgante, and G. Ertl, Science **287**, 1474 (2000).

55 S.-B. Li, Chinese J. Chem. **19**, 16 (2001).

56 S.-B. Li, J. Nat. Gas. Chem. **12**, 1 (2003).

57 M.-F. Luo, Z.-L. Yan, and L.-Y. Jin, J. Mol. Catal. A: Chemical **260**, 157 (2006).

58 S. Rossignol, F. Gérard, D. Mesnard, C. Kappenstein, and D. Duprez, J. Mat. Chem. **13**, 3017 (2003).

59 Z. Song, W. Liu, H. Nishiguchi, A. Takami, K. Nagaoka, and Y. Takita, Appl. Catal. A: General **329**, 86 (2007).

60 P. Shuk and M. Greenblatt, Solid State Ionics **116**, 217 (1999).

61 I. Langmuir, Trans. Faraday Soc. **17**, 607 (1922).

62 I. Langmuir, J. Am. Chem. Soc. **38**, 2221 (1916).

63 G. Ertl and P. Rau, Surf. Sci. **15**, 443 (1969).

64 G. Ertl, J. Vac. Technol. A **1**, 1247 (1983).

65 J. R. Jennings, *Catalytic Ammonia Synthesis* (Plenum, New York, 1991).

[66] A. Schaefer, T. Schroeder, G. Lupina, Y. Borchert, J. Dabrowski, C. Wenger, and M. Bäumer, Surf. Sci. **601**, 1473 (2006).

[67] H.-J. Freund, H. Kuhlenbeck, J. Libuda, G. Pupprechter, M. Bäumer, and H. Hamann, Top. Catal. **15**, 201 (2001).

[68] G. A. Somorjai, R. L. York, D. Butcher, and J. Y. Park, PCCP **9**, 3500 (2007).

[69] C. R. Henry, Surf. Sci. Rep. **31**, 231 (1998).

[70] J. H. Larsen and I. Chorkendorf, Surf. Sci. Rep. **35**, 163 (1999).

[71] P. S. Cremer, C. Stanners, J. W. Niemantsverdriet, Y. R. Shen, and G. Somorjai, Surf. Sci. **328**, 111 (1995).

[72] J. Libuda and H. J. Freund, J. Phys. Chem. **106**, 4901 (2002).

[73] J. Libuda, S. Schauermann, M. Laurin, T. Schalow, and H. J. Freund, Monatsh. Chem. **136**, 59 (2005).

[74] M. L. Yu and L. A. DeLouise, Surf. Sci. Rep. **19**, 285 (1994).

[75] J. A. Barker and D. J. Auerbach, Surf. Sci. Rep. **4**, 1 (1985).

[76] S. J. Tauster, S. C. Fung, R. T. K. Baker, and J. A. Horsley, Science **211**, 1121 (1981).

[77] M. Bäumer and H.-J. Freund, Prog. Surf. Sci. **61**, 127 (1999).

[78] C. T. Campbell, Surf. Sci. Rep. **27**, 111 (1997).

[79] S. Tanaka, H. Ogasawara, K. Okada, and A. Kotani, J. Phys. Soc. Jpn. **64**, 2225 (1995).

[80] A. Moewes, D. L. Ederer, M. M. Grush, and T. A. Callcott, Phys. Rev. B **59**, 5452 (1999).

[81] A. Kotani and H. Ogasawara, J. Elect. Spec. Rel. Phenom. **60**, 257 (1992).

[82] A. Bianconi, A. Kotani, K. Okada, R. Giorgi, A. Gargano, A. Marcelli, and T. Miyahara, Phys. Rev. B **38**, 3433 (1988).

[83] L. Petit, A. Svane, Z. Szotek, and W. M. Temmerman, Phys. Rev. B **72**, 205118 (2005).

[84] D. D. Koelling, A. M. Boring, and J. H. Wood, Solid State Commun. **47**, 227 (1983).

[85] N. V. Skorodumova, S. I. Simak, B. I. Lundqvist, I. A. Abrikosov, and B. Johansson, Phys. Rev. Lett. **89**, 166601 (2002).

[86] H.-W. Chiang, R. N. Blumenthal, and R. A. Fournelle, Solid State Ionics **66**, 85 (1993).

[87] A. Schaefer, S. Gevers, V. Zielasek, T. Schroeder, J. Falta, J. Wollschläger, and M. Bäumer, J. Chem. Phys. **134**, 054701 (2011).

[88] E. S. Putna, J. M. Vohs, and R. J. Gorte, J. Phys. Chem. **100**, 17862 (1996).

[89] T. Inoue, Y. Yamamoto, and A. Satoh, Mat. Res. Soc. Symp. Proc. **441**, 535 (1997).

[90] A. Fissel, H. J. Osten, and E. Bugiel, J. Vac. Sci. Technol. B **21**, 1765 (2003).

[91] H. Nagata, T. Tsukahara, S. Gonda, M. Yoshimoto, and H. Koinuma, Jpn. J. Appl. Phys. **30**, 1136 (1991).

[92] T. Inoue, T. Ohsuna, L. Luo, D. Wu, C. J. Maggiore, Y. Yamamoto, Y. Sakurai, and J. H. Chang, Appl. Phys. Lett. **59**, 3604 (1991).

[93] G. Niu, P. Zaumseil, M. A. Schubert, M. H. Zoellner, J. Dabrowski, and T. Schroeder, Appl. Phys. Lett. **102**, 011906 (2013).

[94] T. Ami, Y. Ishida, N. Nagasawa, A. Machida, and M. Suzuki, Appl. Phys. Lett. **78**, 1361 (2001).

[95] V. Trtik, F. Sanchez, R. Aguiar, Y. Maniette, C. Ferrater, and M. Varela, Appl. Phys. A **67**, 455 (1998).

[96] C.-H. Chen, A. Saiki, N. Wakiya, K. Shinozaki, and N. Mizutani, J. Cryst. Growth **219**, 253 (2000).

[97] F. Sanchez, M. Varela, C. Ferrater, M. V. Garcia-Cuenca, R. Aguiar, and J. L. Morenza, Appl. Surf. Sci. **70/71**, 94 (1993).

[98] T. Inoue, Y. Yamamoto, S. Koyama, S. Suzuki, and Y. Ueda, Appl. Phys. Lett. **56**, 1332 (1990).

[99] H. Koinuma, H. Nagata, T. Tsukahara, S. Gonda, and M. Yoshimoto, Appl. Phys. Lett. **58**, 2027 (1991).

[100] T. Inoue, M. Osonoe, H. Tohda, M. Hiramatsu, Y. Yamamoto, A. Yamanaka, and T. Nakayama, J. Appl. Phys. **69**, 8313 (1991).

[101] D. B. Fenner, A. M. Viano, D. K. Fork, G. A. N. Connel, J. B. Boyce, F. A. Ponce, and J. C. Tramontana, J. Appl. Phys. **69**, 2176 (1990).

[102] T. Chykyow, S. M. Bedair, L. Tye, and N. A. El-Masry, Appl. Phys. Lett. **65**, 1030 (1994).

[103] B. Hirschauer, M. Göthelied, E. Janin, H. Lu, and U. O. Karlsson, Appl. Surf. Sci. **148**, 164 (1999).

[104] Y. Nishikawa, D. Matsushita, N. Satou, M. Yoshiki, T. Schimizu, T. Yamaguchi, H. Satake, and N. Noburu, J. Electrochem. Soc. **151**, 202 (2004).

[105] Y. Nishikawa, N. Fukushima, N. Yasuda, K. Nakayama, and S. Ikegawa, Jpn. J. Appl. Phys. **41**, 2480 (2002).

[106] J. I. Flege, et al., Phys. Rev. B **84**, 235418 (2011).

[107] H. Nagata, M. Yoshimoto, and H. Koinuma, J. Cryst. Growth **123**, 1 (1992).

[108] H. J. Osten, J. P. Liu, E. Bugiel, H.-J. Müssig, and P. Zaumseil, Mat. Sci. Eng. B **87**, 297 (2001).

[109] T. Schroeder, et al., J. Appl. Phys. **97**, 074906 (2005).

[110] A. Schaefer, et al., Phys. Rev. B **80**, 045414 (2009).

[111] L. Libralesso, T. Schroeder, T.-L. Lee, and J. Zegenhagen, Surf. Sci. **598**, 347 (2005).

[112] N. M. Jeutter, W. Moritz, A. Sidorenko, and A. Stierle, Appl. Phys. Lett. **90**, 062906 (2007).

[113] N. M. Jeutter, 2005.

[114] T. Schroeder, P. Zaumseil, G. Weidner, C. Wenger, J. Dabrowski, P. Storck, and H.-J. Müssig, J. Appl. Phys. **99**, 014101 (2006).

[115] J. P. Liu, P. Zaumseil, E. Bugiel, and H. J. Osten, Appl. Phys. Lett. **79**, 671 (2001).

[116] D. K. Fork, D. B. Fenner, and T. H. Geballe, J. Appl. Phys. **68**, 4316 (1990).

[117] T. Weisemoeller, et al., J. Appl. Phys. **105**, 124108 (2009).

[118] S. Gevers, T. Weisemoeller, A. Schaefer, V. Zielasek, M. Bäumer, and J. Wollschläger, Phys. Rev. B **83**, 193408 (2011).

[119] S. Gevers, T. Weisemoeller, B. Zimmermann, F. Bertram, C. Deiter, and J. Wollschläger, J. Phys.: Condens. Matter **21**, 175408 (2009).

[120] S. Gevers, T. Weisemoeller, D. Bruns, A. Giussani, T. Schroeder, and J. Wollschläger, J. Phys.: Condens. Matter **23**, 115904 (2011).

[121] W. Kern and K. A. Reinhardt, *Handbook of Semiconductor Wafer Cleaning Technology* (William Andrew, Norwich NY, 1993).

[122] G. B. D. Rousseau, V. Dhanak, and M. Kadodwala, Surf. Sci. **494**, 251 (2001).

[123] K. Takayanagi, Y. Tanishiro, S. Takahashi, and M. Takahashi, Surf. Sci. **164**, 367 (1985).

[124] I. V. Markov, *Crystal Growth for beginners* (World Scientific, Singapore, 2003).

[125] M. A. Herman and H. Sitter, *Molecular Beam Epitaxy* (Springer-Verlag, Berlin, 1989).

[126] A. Y. Cho, J. Vac. Sci. Technol. **8**, S31 (1971).

127 A. Y. Cho and J. R. Arthur, Prog. Solid State Chem. **10**, 157 (1975).

128 A. Giussani, PhD thesis, Universität Osnabrück, 2010.

129 H. Hertz, Ann. Phys. **31**, 983 (1887).

130 A. Einstein, Ann. Phys. **17**, 132 (1905).

131 D. Briggs and M. P. Seah, *Practical Surface Analysis* (Wiley, Chichester, 1983).

132 S. Hüfner, *Photoelectron Spectroscopy: Principles and Applications* (Springer, Berlin, 1995).

133 C. S. Fadley, Prog. Surf. Sci. **16**, 275 (1984).

134 J. H. Scofield, J. Electron. Spectrosc. Relat. Phenom. **8**, 129 (1976).

135 R. F. Reilman, A. Msezane, and S. T. Manson, j. Elect. Spec. Rel. Phenom. **8**, 389 (1976).

136 J. B. Hudson, *Surface Science* (Butterworth-Heinemann, Stoneham, 1992).

137 S. Tanuma, c. J. Powell, and D. R. Penn, Surf. Interface Anal. **21**, 159 (2009).

138 S. Tanuma, C. J. Powell, and D. R. Penn, Surf. Interface Anal. **20**, 77 (1993).

139 S. Tanuma, C. J. Powell, and D. R. Penn, Surf. Interface Anal. **35**, 268 (2003).

140 B. E. Warren, *X-ray Diffraction* (Dover Publications, Inc., New York, 1990).

141 M. Birkholz, *Thin Film Analysis by X-ray Scattering* (Wiley VCH Verlag GmbH, Weinheim, 2006).

142 G. Kozlowski, PhD thesis, Brandenburgische Technische Universität Cottbus, 2012.

143 P. Zaumseil, J. Phys. D: Appl. Phys. **41**, 135308 (2008).

144 L. Tarnawska, PhD thesis, Brandenburgische Technische Universität Cottbus, 2013.

145 P. Zaumseil, in *Rocking and Reclectivity Simulation Software* (IHP, Frankfurt(Oder).

146 D. L. Rousseau, R. P. Baumann, and S. P. S. Porto, J. Raman Spectrosc. **10**, 253 (1981).

147 A. Ubaldini and M. M. Carnasciali, J. Alloy. Compd. **454**, 374 (2008).

148 A. Smekal, Naturwiss. **11**, 873 (1923).

149 C. V. Raman and K. S. Krishnan, Nature **121**, 501 (1928).

150 W. H. Weber and R. Merlin, *Raman scattering in material science* (Springer, 2000).

151 M. Cardona and G. Güntherodt, *Light scattering in solids II: basic concepts and instrumentation* (Springer, 1982).

152 I. R. Lewis and H. G. M. Edwards, *Handbook of Raman Spectroscopy* (CRC Press, Basel, 2001).

153 W. H. Weber, K. C. Hass, and J. R. McBride, Phys. Rev. B **48**, 178 (1993).

154 M. H. Zoellner, et al., Phys. Rev. B **85**, 035302 (2012).

155 P. Giannozzi, et al., J. Phys.: Condens. Matter **21**, 395502 (2009).

156 J. P. Perdew and A. Zunger, Phys. Rev. B **23**, 5048 (1981).

157 N. V. Skorodumova, M. Baudin, and K. Hermansson, Phys. Rev. B **69**, 075401 (2004).

158 J. L. F. D. Silva, M. V. Ganduglia-Pirovano, J. Sauer, V. Bayer, and G. Kresse, Phys. Rev. B **75**, 045121 (2007).

159 J. Manhan, K. Geib, G. Robinson, and R. Long, J. Vac. Sci. Technol. **8**, 3692 (1990).

160 M. Dabrowska-Szata, Mat. Chem. and Phys. **81**, 257 (2003).

161 A. Ichimiya and P. Cohen, *High Energy Electron Diffraction* (Cambridge University Press, 2004).

162 W. Braun, *Applied RHEED: Reflection High Energy Electron Diffraction During Crystal Growth* (Springer, 1999).

163 J. Klein, PhD thesis, Universität zu Köln, 2001.

164 D. B. Williams and B. C. Carter, *Transmission Electron Microscopy: A Textbook for Materials Science* (Plenum Press, 1996).

165 E. d. Hoffmann and V. Stroobant, *Mass Spectrometry: Principles and Applications* (John Wiley and Sons, Toronto, 2007).

166 L. Eyring and N. C. Baenziger, J. Appl. Phys. **33**, 428 (1962).

167 Z. X. Mei, Y. Wang, X. L. Du, Z. Q. Zeng, M. J. Ying, H. Zheng, J. F. Jia, Q. K. Xue, and Z. Zhang, J. Cryst. Growth **289**, 686 (2006).

168 N. Yu, P. C. McIntyre, M. Nastasi, and K. E. Sickafus, Phys. Rev. B **52**, 17518 (1995).

169 L. Tarnawska, A. Giussani, P. Zaumseil, M. A. Schubert, R. Paszkiewicz, O. Brandt, P. Storck, and T. Schroeder, J. Appl. Phys. **108**, 063502 (2010).

170 T. Schroeder, I. Costina, P. Storck, A. Wilke, O. Seifarth, A. Giussani, H.-J. Müssig, and P. Zaumseil, J. Appl. Phys. **103**, 084102 (2008).

171 R. M. Wallace and G. D. Wilk, Crit. Rev. Solid State Mater. Sci. **28**, 231 (2003).

172 P. Zaumseil and T. Schroeder, J. Phys. D: Appl. Phys. **44**, 055403 (2011).

173 M. H. Zoellner, P. Zaumseil, H. Wilkens, S. Gevers, J. Wollschläger, M. Bäumer, Y.-H. Xie, G. Niu, and T. Schroeder, J. Cryst. Growth **355**, 159 (2012).

174 A. Allahgholi, PhD tesis, Universität Bremen, 2013.

175 A. Pfau and K. D. Schierbaum, Surf. Sci. **321**, 71 (1994).

176 P. Burroughs, A. Hamnett, A. F. Orchard, and G. Thornton, J. Chem. Soc. Dalton Trans. **17**, 1686 (1976).

177 M. Romeo, K. Bak, J. E. Fallah, F. l. Normand, and L. Hilaire, Surf. Interface Anal. **20**, 508 (1993).

178 J. P. Holgado, R. Alvarez, and G. Munuera, Appl. Surf. Sci. **161**, 301 (2000).

179 G. Niu, et al., to be submitted to Adv. Mater. (2013).

180 J. D. McCullough, J. Am. Chem. Soc. **72**, 1386 (1950).

181 I. D. Wolf, Semicond. Sci. Technol. **11**, 139 (1996).

182 L. Li, F. Chen, J.-Q. Lu, and M.-F. Luo, J. Phys. Chem. **115**, 7972 (2011).

183 A. Nakajima, A. Yoshihara, and M. Ishigama, Phys. Rev. B **50**, 13297 (1994).

184 M. H. Zoellner, G. Niu, J.-H. Jhang, A. Schaefer, P. Zaumseil, M. Bäumer, and T. Schroeder, accepted by J. Phys. Chem. C (2013).

185 J. E. Spanier, R. D. Robinson, F. Zhang, S.-W. Chan, and I. P. Herman, Phys. Rev. B **64**, 245407 (2001).

186 J. R. McBride, K. C. Hass, B. D. Pointdexter, and W. H. Weber, J. Appl. Phys. **76**, 2435 (1994).

187 H. Wilkens, S. Gevers, S. Röhe, A. Schaefer, M. Bäumer, M. H. Zoellner, T. Schroeder, and J. Wollschläger, submitted to J. Phys. Chem. C (2013).

188 Y. Tang, H. Zhang, L. Cui, C. Ouyang, S. Shi, W. Tang, H. Li, J.-S. Lee, and L. Chen, Phys. Rev. B **82**, 125104 (2010).

189 G. Zhou and R. J. Gorte, J. Phys. Chem. B **112**, 9869 (2008).

190 S. Sato, R. Takahashi, M. Kobune, and H. Gotoh, Appl. Catal. A: General **356**, 57 (2009).

191 M. L. Turdeau, A. Tschope, and J. Y. Yang, Surf. Interface Anal. **23**, 219 (1995).

192 H. Wilkens, O. Schuckmann, R. Oelke, S. Gevers, A. Schaefer, M. Bäumer, M. H. Zoellner, T. Schroeder, and J. Wollschläger, Appl. Phys. Lett. **102**, 111602 (2013).

193 T. Taniguchi, T. Watanabe, N. Sugiyama, A. K. Subramani, H. Wagata, N. Matsushita, and M. Yoshimura, J. Phys. Chem. C **113**, 19789 (2009).

[194] N. Mladenov, *Modellierung von Autoabgaskatalysatoren* (KTI Scientific Publishing, Karlsruhe, 2009).

[195] S. D. Senanayake, J. Zhou, A. P. Baddorf, and D. R. Mullins, Surf. Sci. **601**, 3215 (2007).

[196] F. Esch, S. Fabris, L. Zhou, T. Montini, C. Africh, P. Fornasiero, G. Comelli, and R. Rose, Science **309**, 752 (2005).

[197] S. A. Wolf, D. D. Awschalom, R. A. Buhrman, J. M. Daughton, S. v. Molnar, M. L. Roukes, Y. Chtchelkanova, and D. M. Treger, Science, 1488 (2001).

[198] M. Bäumer, J. Libuda, K. M. Neyman, N. Rösch, G. Rupprechter, and H.-J. Freund, PCCP **9**, 3541 (2007).

[199] N. Paunovic, Z. Dohcevic-Mitrovic, R. Scurtu, S. Askrabic, M. Prekajski, B. Matovic, and Z. V. Popovic, Nanoscale **4**, 5469 (2012).

[200] J. M. D. Coey, M. Venkatesan, and C. B. Fitzgerald, Nature **4**, 173 (2005).